UNIVERSIDAD DE CHILE
FACULTAD DE CIENCIAS FÍSICAS Y MATEMÁTICAS
DEPARTAMENTO DE ASTRONOMÍA

THE PHYSICAL AND KINEMATICAL STRUCTURE OF MASSIVE AND DENSE COLD CORES

TESIS PARA OPTAR AL GRADO DE
DOCTORA EN CIENCIAS, MENCIÓN ASTRONOMÍA

ELISE MARIE GERMAINE SERVAJEAN BERGOEING

PROFESOR GUÍA:
GUIDO GARAY BRIGNARDELLO

MIEMBROS DE LA COMISIÓN:
ANDRÉS ESCALA ASTORQUIZA
DIEGO MARDONES PÉREZ
LARS-AKE NYMAN

Este trabajo ha sido parcialmente financiado por CONICYT-PCHA/Doctorado Nacional/21110496, CONICY-PFB-06 y CONICYT-AFB-170002.

SANTIAGO DE CHILE
2019

RESUMEN DE LA MEMORIA PARA OPTAR
AL TÍTULO DE DOCTORA EN CIENCIAS, MENCIÓN ASTRONOMÍA
POR: ELISE MARIE GERMAINE SERVAJEAN BERGOEING
FECHA: 2019
PROF. GUÍA: GUIDO GARAY BRIGNARDELLO

THE PHYSICAL AND KINEMATICAL STRUCTURE OF MASSIVE AND DENSE COLD CORES

A pesar de los esfuerzos enfocados en el estudio de la formación de estrellas de alta masa, no tenemos un claro entendimiento de cuales son los procesos involucrados. Para entender mejor estos fenómenos necesitamos caracterizar objetos en estados muy tempranos de formación y así poder inferir cuales son las condiciones iniciales de estos procesos. En esta tesis estudiamos estos objetos desde dos frentes diferentes. Primero caracterizamos cuatro nubes masivas frías y densas en estados previos a la formación de estrellas (G305.136+0.068, G333.125-0.562, G18.606-0.076 and G34.458+0.121) y analizamos cuales son sus señales de colapso. Realizamos esto con datos del Atacama Pathfinder Experiment (APEX) con una resolución angular de ∼20". Por otro lado estudiamos la distribución de masa dentro del objeto más inactivo (G305.136+0.068), con datos del Atacama Large Millimeter/submillimeter Array (ALMA) con alta resolución angular (∼2"), pudiendo detectar los pequeños fragmentos que serán semillas de estrellas.

Los cuatro objetos observados con APEX muestran diversas características cinemáticas señalando diferentes estados de evolución. En todos los objetos las dispersiones de velocidades de las líneas moleculares son mucho mayores que los anchos termales implicando otro tipo de procesos como turbulencia y/o colapso. El análisis virial de los objetos indica que se encuentran cercanos a estar ligados. En dos de los objetos estudiados (G305.136+0.068 y G333.125-0.562) encontramos en los perfiles de las líneas moleculares claras señales de colapso.

En el caso del objeto observado con ALMA, G305.136+0.069, los datos de continuo de polvo muestran doce estructuras compactas con masas de 3.3 a 50.6 $M_\odot$ y radios de 1800 to 5300 UA. Las líneas moleculares muestran que estos pequeños fragmentos también están dominados por movimientos no termales. El análisis virial de los fragmentos indica que los más masivos están más cerca de colapsar. La distribución de masas de los fragmentos detectados tiene una forma mucho más plana que la que muestra la función de masa inicial estelar, debido a una sobrepoblación de objetos de alta masa.

Pour Papa qui est maintenant parmi les étoiles.

Agradecimientos

Hace bastante tiempo, conversando sobre la tesis con mi padre, me preguntó si ya había empezado a escribir los agradecimientos. En ese momento me pareció una exageración pensarlo con tanto tiempo de anticipación, pero ahora que ha llegado el momento me doy cuenta de por qué lo decía. Agradecer a todas las personas es imposible, pero quiero darle el espacio a esas personas que estuvieron ahí en los momentos más importantes y marcaron la diferencia.

Primero quiero agradecer a mis padres por todo el amor que he recibido en estos años. Por el apoyo y el empuje que han ayudado a que llegue al final de esta aventura. Agradecerle a mi padre porque me contagió el amor por el conocimiento y que, a pesar de no seguir a nuestro lado, cada día me dice las palabras que necesito para seguir soñando y mirar más lejos. A mi madre, que es mi amiga del alma. La persona que siempre tiene la palabra acertada y que me ha enseñado que en la vida todo tiene solución menos la muerte y que hay que seguir adelante pase lo que pase con la mejor de las disposiciones.

Quiero agradecerle a Francisco, el amor de mi vida, que estos últimos ocho años me ha acompañado en este camino y ha hecho que cada uno de mis días sea mejor que el anterior. Me ha mostrado que soy más de lo que a veces creo y que puedo con todo aunque muchas veces no quiera darme cuenta. Gracias por tu paciencia, tu apoyo y tus consejos, porque sin ti esta tesis no habría sido posible. A Erika y Tete, que aunque no han estado nunca en Calán me han escuchado, apoyado y motivado en este camino. Por todos esos momentos que compartimos en Beauchef, que hacen de nosotras un trío de lo más especial.

Este camino ha sido largo y han habido varias personas que me han acompañado en diferentes etapas. A Srini y a Paula quiero agradecerles por esos primeros años, los que compartimos juntos en la oficina mientras hacíamos tareas. Esos años donde creíamos que el camino sería más fácil, y más corto, pero que nos unieron tanto que a pesar de la distancia seguimos juntos de alguna manera. A la buena oficina, a Jose, Matías, Pola, Coni y Mari, porque me hicieron sentir una más de su grupo, me acogieron cuando me hizo falta y estuvieron ahí en los momentos difíciles. A Yanett y Laura, que siempre tuvieron la disposición de ayudarme cuando me hizo falta y me acompañaron en mis aventuras por Australia.

A mi mentor, Guido, que después de todos estos años trabajando juntos aún me tiene paciencia. He aprendido muchísimo y a pesar de no seguir el camino tradicional de la investigación, espero seguir aprendiendo y compartiendo experiencias con él. A Jill, que aunque no está compartiendo este momento conmigo, me permitió vivir maravillosos momentos en Australia. Gracias por tu optimismo y tu motivación.

Contents

List of Tables

List of Figures

Chapter 1

Introduction

The main goal of this thesis is to investigate the physical and kinematical properties of massive and dense cold clumps through observations. Knowing their properties, the levels of fragmentation and which are the processes that lead to the formation of stars will help us to understand how high-mass stars are born.

Star formation is one of the fundamental topics in astrophysics because stars and star clusters are the building blocks of galaxies. Moreover, massive stars ($M_* > 8\ M_\odot$) are fundamental in the evolution of galaxies since they dominate their energy input, produce the heavy elements that enrich the interstellar medium (ISM) and affect the star formation process. Therefore, understanding how stars are formed is key to understanding other processes in Galaxies and in our universe.

In spite of the fact that most stars, and in particular high-mass stars, form in clusters (Lada and Lada 2003) our understanding of the star formation process is mainly limited to isolated low-mass protostars. Thus, understanding cluster formation is necessary to understand the formation of high-mass stars. However the problem is difficult observationally because massive star formation occurs in distant, highly obscured regions, and it is difficult theoretically because of the many processes that must be included. The study of the earliest stages of high-mass star formation and their environmental conditions is key to understanding how high-mass stars are formed.

1.1 Molecular clouds

Visual telescopic observations by William and Caroline Herschel (Herschel 1785) in the late eighteenth century led to the discovery of the first dark patches in the sky, which we now know correspond to Molecular Clouds. Later, during the 1920s, photographic observations of Barnard and Wolf established them as discrete, optically opaque interstellar clouds. These observations demonstrated that the material in these clouds contained dust grains which completely absorbed the optical emission from background stars. At the time of the detection in the 1950s of the atomic hydrogen in the ISM using the 21-cm line, it was unclear if the

composition of the ISM gas could be more complex. The first ISM molecules, simple as OH and more complex as NH_3 and H_2O, were detected in the 1960s. During the 1970s, through observations of CO (e.g. Wilson et al. 1970) , the data quickly lead to the realization that dark clouds were molecular clouds, consisting almost entirely of molecular hydrogen mixed with small amounts of interstellar dust and trace amounts of more complex molecular species.

The modern study of the ISM started with long-wavelength observations (Far-IR, sub-millimetre and millimetre wavelengths) where the extinction of the interstellar dust is lower allowing us to peer deep within them and study the physical processes in the colder regions. These observations have shown that stars and planets are formed within dark clouds also called molecular clouds.

1.1.1 Formation

Molecular clouds are not isolated, but are dense condensations within more widely distributed, mostly atomic gas, extended envelopes that typically have comparable mass (Blitz et al. 1988). They are highly irregular structures and have complex shapes (many of them filamentary) that do not at all resemble equilibrium configurations.

Molecular clouds are transient structures and do not survive without major changes for more than a few times 10^7 years (Blitz and Shu 1980; Larson 1981). The short lifetimes of molecular clouds are directly indicated by the fact that the range in age of the young stars associated with them is only about 10 to 20 Myr, comparable to the internal dynamical time scales of large molecular clouds (Larson 1981).

Two possible formation mechanisms for molecular clouds that have been considered are cloud growth by random collisions and coalescence, i.e. building of large clouds from smaller ones by random collisions and coalescence, and gravitational instability, i.e. large-scale gravitational instability and amplification effects in the Galactic gas layer. Evidence that gravitational instability effects are indeed primarily responsible for both molecular cloud formation and star formation in galaxies is provided by the fact that star formation is observed to occur only where the surface density of gas in galactic disks exceeds a threshold which is close to the critical value predicted for the onset of gravitational instability (Kennicutt 1990). While collisions almost certainly play a role in the building up of large molecular clouds, it nevertheless seems clear that purely random collisions cannot build them fast enough and that more ordered large-scale motions are therefore required.

1.1.2 Classification and Composition

Figure 1.1 and Table 1.1 illustrate and summarize the properties of the ISM cloud classification proposed by Snow and McCall (2006). Diffuse atomic clouds represent the regime in the ISM that is fully exposed to the interstellar radiation field, and consequently nearly all molecules are quickly destroyed by photo dissociation. Hydrogen is mainly in neutral atomic form and very little chemistry occurs in this gas. Diffuse molecular clouds represent

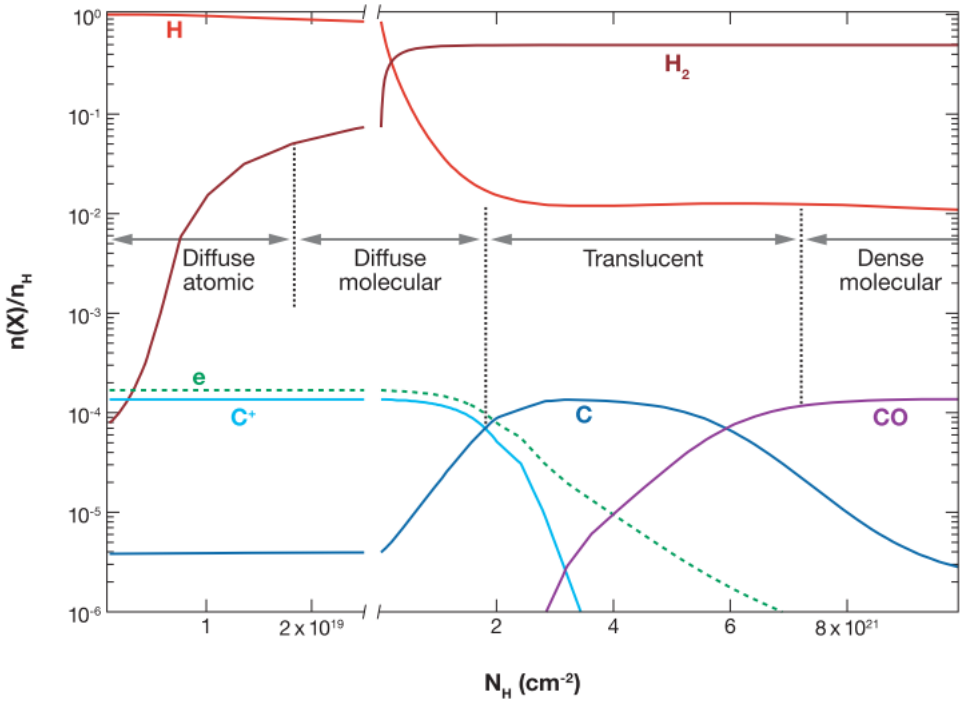

Figure 1.1: Relation between density and molecular and atomic abundance in molecular clouds. The proposed classification of Interstellar Cloud Types from Snow and McCall (2006) is illustrated.

Table 1.1: Classification of Interstellar Cloud Types from Snow and McCall (2006)

	Diffuse Atomic	Diffuse Molecular	Translucent	Dense Molecular
Defining Characteristic	$f^n_{H_2}$ <0.1	$f^n_{H_2}$ >0.1 $f^n_{C^+}$ >0.5	$f^n_{C^+}$ <0.5 f^n_{CO} <0.9	f^n_{CO} >0.9
A_v (min.)	0	∼0.2	∼1-2	∼5-10
n_H (cm^{-3})	10-100	100-500	500-5000	$>10^4$
T (K)	30-100	30-100	15-50	10-50

(f^n is the local fraction, in terms of number densities, thus, $f^n_{H_2}$= 2n(H_2)/n_H, f^n_{CO} = n(CO)/n_C, etc.)

the regime where the interstellar radiation field is sufficiently attenuated so that the local fraction of hydrogen in molecular form becomes substantial. However, enough interstellar radiation is still present such that carbon is predominantly still in the form of C^+. The translucent cloud regime is the least well understood of all the cloud types. They must, in steady state, be surrounded by diffuse molecular cloud material. Finally, Dense Molecular clouds are typically self-gravitating, and are most often observed by IR absorption and mm-wave emission methods. More than 130 molecules have been detected in molecular clouds.

1.1.3 Structure

Molecular clouds are irregular structures with regions with wide range of sizes and densities from 10^2 to 10^8 cm^{-3}. The largest structures (sizes ∼ 10 pc), known as Giant molecular

Table 1.2: Average properties of the different types of molecular clouds: Giant Molecular Clouds (GMC), typical clouds, clumps and low-mass and high-mass cores (Blitz 1993; Garay and Lizano 1999; Bergin and Tafalla 2007; Beuther et al. 2007).

	GMC	Clouds	Clumps	Low-mass Cores	High-mass Cores
Mass ($M_\odot$)	1-2×10^5	10^3-10^4	50-500	0.5-5	$\sim10^2$
Size (pc)	40	2-15	0.3-3	0.03-0.2	<0.1
Density (cm^{-3})	∼50	50-500	10^3-10^4	10^4-10^5	10^5-10^8
T (K)	∼10	∼10	10-20	8-12	10-50

clouds, have masses $\gtrsim10^4$ $M_\odot$, are generally gravitationally bound, and may contain several sites of star formation. However, there also exist small molecular clouds with masses $\lesssim10^2$ $M_\odot$, such as the unbound high latitude clouds discovered by Blitz et al. (1984), and the small, gravitationally bound molecular clouds in the Galactic plane catalogued by Clemens and Barvainis (1988). A small number of low-mass stars are observed to form in some of these clouds but the contribution to their total star formation rate in the Galaxy is negligible (Magnani and Onello 1995).

Clumps are high density (10^3 - 10^4 cm^{-3}) coherent regions out of which stellar clusters form. Although most clusters are unbound, the gas out of which they form is bound (Williams et al. 1995). Cores are regions out of which single stars (or multiple systems such as binaries) form and are necessarily gravitationally bound. They have sizes up to 0.1 pc and densities from 10^4 to 10^8 cm^{-3}. Not all material that goes into forming a star must come from the core; some may be accreted from the surrounding clump or cloud as the protostar moves through it (Bonnell 1997).

1.2 Star formation

Molecular clouds are the birth places of stars across the whole range of masses. The most massive stars reach the main sequence while still accreting whereas low-mass stars must contract for tens to hundreds of millions of years before becoming hot enough for sustained hydrogen fusion. Hence, two categories are usually considered: low-mass star formation and high-mass star formation. The dividing line between them is 8 $M_\odot$. Our understanding of the star formation process is mainly limited to isolated low-mass protostars due to the fact that hig- mass stars evolve quickly making very difficult to observe their formation process. The differences between them are explained in the following sections.

1.2.1 Low-mass star formation

The formation of low-mass stars can be studied in greatest detail because it occurs in relatively nearby clouds and sometimes in isolation from other forming stars. The formation of low-mass protostars can be summarized in four stages (Shu et al. 1987) that are illustrated

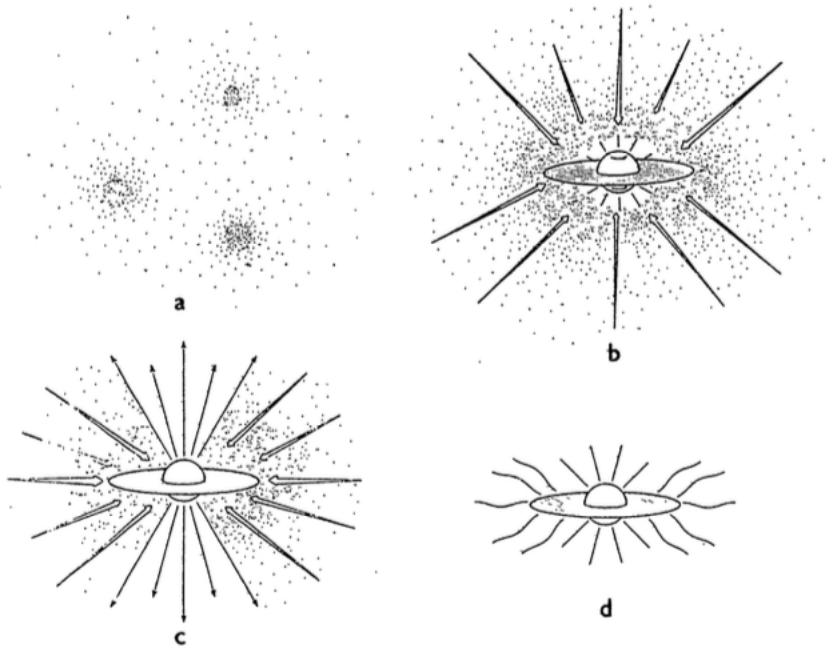

Figure 1.2: The four stages of star formation from Shu et al. (1987). (a) Cores form within molecular clouds as magnetic and turbulent support is lost, (b) A protostar with a surrounding disk forms at the center of the core collapsing from inside-out. (c) Stellar wind breaks out along the rotational axis of the disk. (d)The infall finishes revealing a newly formed star with a circumstellar disk.

in Figure 1.2. The process begins with the fragmentation of a molecular cloud into rotating cores approaching a centrally concentrated state with a density profile of the type $\rho \sim r^{-2}$. Once the cores loose support they collapse from "inside-out". A deeply embedded protostar and disk will appear from which it will accrete material. Both the protostar and the disk will be surrounded by an envelope of dust and gas.

As a protostar accretes matter, deuterium will eventually ignite in the central regions and drive the star nearly completely convective if its mass is less than $\sim$2 $M_{\odot}$. As time proceeds, the material will fall preferentially onto the disk. A stellar wind appears, which escapes through the rotational poles, that are the ones with the weakest resistance, leading to collimated jets and bipolar outflows. With time the opening angle of the wind will be wider sweeping out the material of the envelope, obtaining finally a young star.

1.2.2 High-mass star formation

Unlike the low-mass scenario, the processes involved in the formation of high-mass stars are still not well understood. High-mass stars form in clusters (Lada and Lada 2003) therefore to understand their formation it is necessary to understand cluster formation. The hosts of young high-mass stars and clusters are known to be massive and dense clumps with masses of a few $10^3 M_{\odot}$, sizes of $\sim$0.4 pc and temperatures of $\sim$30 K (e.g., Plume et al. 1997, Faúndez et al. 2004). Much colder clumps (T $<$ 14K) with similar masses, sizes and densities have

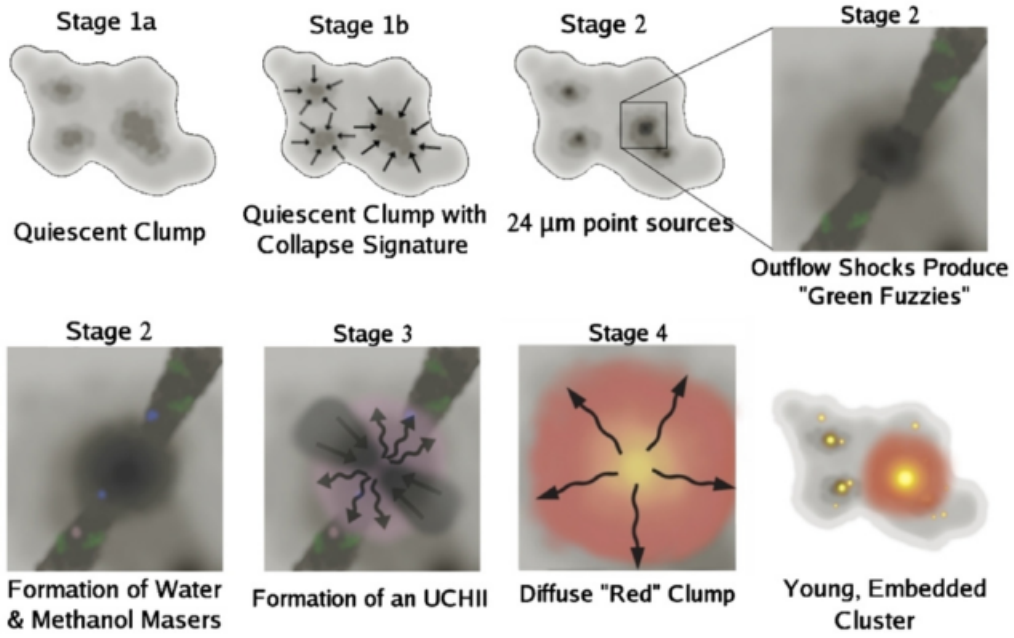

Figure 1.3: Schematic illustration of the discussed evolutionary sequence for high-mass star formation from Battersby et al. (2010).

also been identified (Garay et al. 2004; Pillai et al. 2006), which would correspond to the initial conditions for the process of formation of high-mass stars and clusters (Garay et al. 2004). These clumps are expected to fragment into a group of protostellar cores which will collapse to produce a cluster of stars. However, the way in which these massive and dense cold clumps (MDCCs) evolve to form massive stars is still poorly known. Clumps which are on the verge of forming protostars, but have not formed any yet, must still reflect the initial conditions of the formation of protoclusters. Searching and studying such objects is crucial for our understanding of star formation.

There are two main models that have been proposed to explain the formation of high-mass stars: Competitive Accretion (Bonnell et al. 2001, Wang et al. 2010) and Core Accretion (McLaughlin and Pudritz 1996, McKee and Tan 2003). Their principal difference is related to how and when the mass that will form a star is gathered. In both cases an initial fragmentation is necessary but with different characteristics. In the competitive accretion model the cloud fragments in Jeans-mass fragments ($\sim$0.1 $M_\odot$, for T=10K and n_{H_2}=$10^6 cm^{-3}$) that will accrete mass. The fragments located in regions where more material can be accreted will likely form a high-mass star which results in the segregation of high-mass stars to be formed at the center of a cluster. On the other hand, in the core accretion model, a scaled-up version of low-mass star formation, the high-mass stars are formed from the gravitational collapse of individual cores. This implies that we should be able to find many high-mass pre-stellar cores. Today there is no convincing observational evidence that can rule out any of the two proposed models. However, recent studies based on high angular resolution observations (e.g., Liu et al. 2013, Rathborne et al. 2015) are starting to provide better constraints on particular objects.

Observationally a sequence for the stages of the high-mass star formation has been proposed (Chambers et al. 2009). Figure 1.3 shows a schematic version of the sequence (Battersby et al. 2010). The first stage, Stage 1, is a cold quiescent clump with no signs of active star formation. Within the clump high-mass starless cores will be present. These cores are cold ($\sim$10 K), with masses ranging from 100 $M_\odot$ to few 1000 $M_\odot$, sizes of 0.25-0.5 pc and densities of 10^5 cm^{-3} (Beuther et al. 2007). Observationally, they are characterized by strong cold dust emission, molecular lines at sub-millimetre to millimetre wavelength (e.g CO, CS, N_2H^+) and non detection in the mid-infrared. This first stage can be split into two: a quiescent clump which has not yet begun to collapse (Stage 1a) and a quiescent clump that shows collapse signatures (Stage 1b).

Stage 2 is a hotter, denser clump that shows signs of active star formation. The cores are refered as Hot cores and are internally heated (50-250 K), have masses of 100 to 300 $M_\odot$, sizes < 0.1 pc and densities of 10^5 to 10^8 cm^{-3}. In this stage the cores show at least one sign of active star formation: a 24 μm point source, a "green fuzzy", collimated jets/outflows, or an H_2O or CH_3OH maser. Because the central objects heat their surrounding allowing more molecules to be excited, they also exhibit a rich chemistry, showing emission from complex molecules such as large organic carbon chains (e. g. CH_3CN, HC_3CN, $HC^{13}CCN$ and HNCO) (Blake et al. 1987; Schilke et al. 2001) and shock tracers, such as SiO.

The third stage, Stage 3, is the ignition of an ultra-compact HII region (UCHII). The source will have a strong ($\gtrsim$1 Jy) 24 μm point source and possibly maser emission and outflows. Theory (e.g., McKee and Ostriker 2007) suggests that massive stars reach the main sequence while still accreting, because the accretion timescale is greater than the Kelvin-Helmholtz timescale, meaning that a main-sequence B star may continue to accrete on the main sequence, eventually becoming an O star. Stage 4 is the expansion of the HII region, producing a diffuse "red" clump. However, in the densest cores, the HII region may be quenched by the remaining envelope for some time and a "diffuse red clump" will not form. For UCHII regions not trapped by their surrounding envelope, the UCHII region will expand as the radiation field increases. Finally we see OB associations at the center of a much larger HII region.

1.3 Identification and characterization of High-mass clumps

1.3.1 Basic parameters of radiation

Intensity

The intensity of the radiation is defined such as the energy, which is a measurable quantity, carried by the rays passing through an area dA in a time dt, in a frequency range dν, and within a solid angle dΩ is given by:

$$\mathrm{d}E \triangleq I_\nu \mathrm{d}A\mathrm{d}t\mathrm{d}\Omega\mathrm{d}\nu.$$

The monochromatic intensity I_ν remains constant along a ray path, irrespective of the distance from the emitting source, as long as no absorption or emission occurs along the path. The change in I_ν is described by the equation of radiative transfer:

$$\frac{\mathrm{d}I_\nu}{\mathrm{d}s} = -\kappa_\nu I_\nu + \varepsilon_\nu,$$

where the term κ_ν is the absorption coefficient or opacity, and ε_ν is the emission coefficient or emissivity. Introducing the optical depth τ_ν as variable, defined as $\mathrm{d}\tau_\nu = \kappa_\nu \mathrm{d}s$, the radiative transfer equation takes a simpler form:

$$\frac{\mathrm{d}I_\nu}{\mathrm{d}\tau_\nu} = -I_\nu + S_\nu.$$

where the source function S_ν is defined as:

$$S_\nu = \frac{\varepsilon_\nu}{\kappa_\nu}.$$

Integrating this equation we have the formal solution of the transfer equation:

$$I_\nu(\tau_\nu) = I_\nu(0)\mathrm{e}^{-\tau_\nu} + S_\nu(1 - \mathrm{e}^{-\tau_\nu}).$$

This expression indicates that for large optical depths, i.e. when $\tau_\nu \to \infty$, $I_\nu \to S_\nu(T)$.

Flux Density

In terms of the monochromatic intensity I_ν the power $\mathrm{d}W$ of radiation coming from a direction s within a solid angle $\mathrm{d}\Omega$, through a cross-section of area $\mathrm{d}\sigma$ with a normal inclined by an angle θ from the direction s, within a frequency bandwidth $\mathrm{d}\nu$ centered at ν, is given by:

$$\mathrm{d}W = I_\nu(s)\cos\theta \mathrm{d}\Omega \mathrm{d}\sigma \mathrm{d}\nu.$$

The flux density S_ν is the quantity of radiation energy incoming through a cross section of unit area, per unit frequency bandwidth, and per unit time. The flux density is related to the intensity I_ν by an integral over a solid angle Ω:

$$S_\nu = \int I_\nu \cos\theta \mathrm{d}\Omega.$$

For discrete sources the flux density can be approximated as:

$$S_\nu = \int I_\nu \mathrm{d}\Omega.$$

Brightness temperature

The brightness temperature T_B is defined as the temperature of the blackbody that would give the same intensity as the observed one, $I_\nu = B_\nu(T_B)$. In the Rayleigh-Jeans regime (where $h\nu \ll kT_b$) $B_\nu(T) = \frac{2\nu^2}{c^2}kT$. Then the intensity I_ν adopts the Rayleigh-Jeans approximation for $B_\nu(T)$:

$$I_\nu^{RJ}(T) = \frac{2\nu^2}{c^2}kT_B.$$

In the Rayleigh-Jeans regime the transfer equation takes a simple form:

$$\frac{\mathrm{d}T_B}{\mathrm{d}\tau_\nu} = -T_B + T,$$

where T is the temperature of the material. Hence, in this regime the spectral flux density S_ν is:

$$S_\nu^{RJ}(T) = \frac{2k\nu^2}{c^2}\int T_B \mathrm{d}\Omega.$$

If the radio source can be described by a Gaussian brightness distribution the above expression becomes:

$$\left[\frac{S_\nu}{Jy}\right] = 2.65 T_B \left[\frac{\theta}{'}\right]^2 \left[\frac{\lambda}{cm}\right]^2,$$

which makes possible to determine the brightness temperature of a source by measuring the flux and assuming, or measuring, a solid angle.

Thermal radiation

All objects at non-zero absolute temperature emit radiation. In the case in which the object is in thermodynamic equilibrium at temperature T the thermal radiation is such that

$$S_\nu = B_\nu(T),$$

where $B_\nu(T)$ is the Planck function. This relation represents one of the forms of Kirchoff's law. This radiation field only depends on the frequency ν and on the temperature T.

1.3.2 Dust thermal emission

Interstellar gas clouds are always mixed with dust grains which absorb the UV radiation from their surrounding and re-emits it as thermal radiation. Observing the thermal radiation from the dust gives us important information about the physical properties, such as density and temperature, of molecular clouds. Cold molecular clouds, which have typical temperatures of 10 to 30 K, appear as dark regions in the sky at infrared wavelengths. At these low temperatures, the black body emission peaks at sub-millimetre to millimetre wavelengths.

For a black body in thermodynamic equilibrium the intensity of the radiation is given by the Planck function:

$$B_\nu(T) = \frac{2h\nu^3}{c^2}\frac{1}{\mathrm{e}^{h\nu/kT}-1},$$

where T is the temperature, ν is the frequency, k is the Boltzmann constant, h is the Planck constant and c is the speed of light.

For low frequencies or high temperatures, $h\nu << kT$, we can use the approximation $\mathrm{e}^{h\nu/kT} \simeq 1 + h\nu/kT$, obtaining the Rayleigh-Jeans law:

$$B_\nu^{RJ}(T) \simeq \frac{2\nu^2}{c^2}kT.$$

Physical parameters derived from observations

In this section we overview the different physical parameters (temperature and mass) that can be derived from observations of the thermal dust emission.

Dust temperature: If observations of thermal emission from dust at several frequencies are available, then an spectral energy distribution (SED) model fitting can be done to determine the temperature. The observed intensities are usually interpreted as arising from a single temperature grey-body dust emission model (e.g. Guzman et al. 2015). The monochromatic intensity at a frequency ν is given by:

$$I_\nu(T_\mathrm{d}, N_g) = B_\nu(T_\mathrm{d})(1 - \mathrm{e}^{-\tau_\nu}),$$

where $B_\nu(T_\mathrm{d})$ is the Planck function at a dust temperature T_d and the optical depth $\tau_\nu = N_\mathrm{d}\kappa_\nu = R_{g\mathrm{d}}N_g\kappa_\nu$, where N_d is the dust column density, κ_ν is the dust absorption coefficient, $R_{g\mathrm{d}}$ is the gas-to-dust mass ratio which its generally assumed to be equal to 100. The particle column density is defined by $N_p = N_g/(\mu m_H)$, where $\mu = 2.3$. The number column density of molecular hydrogen N_{H_2} is obtained in the same way but using $\mu = 2.8$ (Kauffmann et al. 2008), under the assumption that all the hydrogen is in molecular form.

The temperature is obtained by minimizing the following function:

$$\chi^2(T_\mathrm{d}, N_g) = \sum_\nu \frac{(I_{\nu,obs} - \tilde{I}_\nu)^2}{\sigma_\nu^2},$$

where the sum is taken over the observed frequencies and $\tilde{I}_\nu$ is the intensity spectrum predicted by the model weighted by the respective bandpass and σ_ν is the variance. The best-fit dust temperature T_d, and gas column density N_g, minimize the χ^2 value.

Column Density and Mass: The column density and mass of a molecular cloud can be obtained from its dust thermal emission as follows. The column density of gas, which in a molecular cloud is mostly in the form of molecular hydrogen, can be expressed in terms of of the dust column density as:

$$N(H_2) = \int n_{H_2}\mathrm{d}s = \frac{1}{\mu_{H_2} m_H \kappa_\nu} \int \kappa_\nu \rho \mathrm{d}s,$$

where n_{H_2} is the particle density of hydrogen molecules, ρ is the density, μ_{H_2} is the weight per hydrogen molecule and m_H is the hydrogen atom mass. Introducing the optical depth τ_ν in the previous relation:

$$N(H_2) = \frac{\tau_\nu}{\mu_{H_2} m_H \kappa_\nu}.$$

Assuming that the dust continuum emission is optically thin then the observed flux per beam at frequency ν is $S_\nu^{beam} = \Omega_b B_\nu \tau_\nu$, and the beam averaged column density can be determined as :

$$N(H_2) = \frac{S_\nu^{beam}}{\Omega_b \kappa_\nu \mu_{H_2} m_H B_\nu(T_{\rm d})},$$

where $\rm B_\nu(T_d)$ is the Planck function at dust temperature $T_{\rm d}$, Ω_b is the beam size, and μ_{H_2} is the mean molecular weight.

The mass is given by the integral of the column densities across the source:

$$M = \mu_{H_2} m_H \int N_{H_2} D^2 {\rm d}\Omega$$

where D is the distance. Assuming the same standard assumptions the dust mass $M_{{\rm d}ust}$ can be written as:

$$M_{\rm dust} = \frac{D^2 S_\nu}{\kappa_\nu B_\nu(T_{\rm d})}.$$

.

1.3.3 Molecular line emission

The emission from molecules can arise from three different types of transitions: rotational, caused by the rotation of the nuclei around an orthogonal axis; vibrational, that happens when the nuclei vibrate around their equilibrium position; and electronic, produced by the de-excitation of electrons in a molecule from one energy level to another.

The main source of molecular emission in the millimeter regime is due to rotational transitions. This type of emission can only come from molecules with a non zero dipole moment. Since quantum mechanics allows molecules to have discrete values of their angular momentum, the energy associated with the rotation is specific for each transition and each molecule. The amount of rotational energy of a molecule is given by:

$$E_{rot} = BJ(J+1) = \frac{^2}{8\pi^2 I} J(J+1)$$

where B is the rotational constant, I is the moment of inertia and J is the angular momentum quantum number. The permitted transitions between lines are the ones where J varies one unit, the frequency of the transition is given by:

$$\nu_{J,J-1} = \frac{E_J - E_{J-1}}{h} = J\frac{\hbar}{2\pi I}.$$

The spontaneous emission coefficient for these transitions is low, hence the population of the energetic levels is dominated by the ambient radiation or collisions between molecules. Molecules located deep inside molecular clouds will typically be excited by collisions while molecules at the edges of the cloud will typically be excited by the ambient radiation. This means that, for the inner parts of the clouds, the excitation temperature of a transition is similar to the kinetic temperature T_k of the molecular cloud. The density at which the transition is thermalized is called critical density, n_{crit}, and is defined as (Snell et al. 1984):

$$n_{crit} = \frac{A}{C(1 - \mathrm{e}^{-h\nu/kT_k})},$$

where A is the inverse radiative lifetime and C is the collisional de-excitation coefficient. As the kinetic temperature of the cloud increases, levels of higher energies will be populated. The population in each level is given by:

$$\frac{N_J}{g_J} \propto exp\left[\frac{E_J}{kT_{\mathrm{ex}}}\right],$$

where N_j is the number of molecules in the level J, g_J is the statistical weight of the level J, E_J is the energy of the upper level, k is the Boltzmann constant, and T_{ex} is the excitation temperature of the gas. In the case of local thermodynamic equilibrium, LTE, $T_{ex} = T_k$.

As shown in the previous relations a molecule will need a certain density and temperature to be excited and therefore emit in a specific transition. Hence, molecular line observations allows us to determine physical and kinematical parameters of the gas in molecular gas.

Observations: Peak intensity, line-width and velocity.

From the molecular line emission of a source we can derive its properties through the analysis of the observed spectra. The three principal characteristics of a spectral line are the intensity, the line-width and the central velocity. The intensity gives information about the density and temperature of the cloud, while the line-width and velocity give information about the kinematics.

At millimetre wavelengths, the observed quantity measured with a radio telescope is called the Antenna Temperature (T_A). If the source is small in comparison to the beam of the telescope, it can be expressed as:

$$T_A = \frac{\Omega_s}{\Omega_b}\eta T_B,$$

where Ω_s is the solid angle of the source, Ω_b is the antenna beam size, η is the main beam efficiency, and T_B is the brightness temperature. This temperature corresponds to the intensity of the spectral line detected by the radio telescope. The antenna temperature is often expressed as the main beam temperature expressed as $T_{MB} = T_A/\eta$.

The observed T_A of a molecular transition is related to the excitation temperature $T_{\mathrm{e}x}$, at which the line is produced, by the expression:

$$T_A = \eta\phi(T_{\mathrm{ex}} - T_{bg})(1 - \mathrm{e}^{-\tau}),$$

where T_{bg} is the background temperature, ϕ is the main beam filling factor, and τ is the opacity of the transition.

The spectral lines are not sharp. There is always a finite width to the observed spectral lines. The spectral broadening of molecular clouds includes three main components (Garay and Lizano 1999): thermal broadening, natural broadening and non-thermal broadening.

The thermal broadening arises from the motions of the atoms and molecules in random directions, with an average speed proportional to the temperature of the gas. This produces the *thermal Doppler width* $\Delta\mathrm{v}_{\mathrm{th}}$ given by:

$$\Delta\mathrm{v}_{\mathrm{th}} = \sqrt{\frac{2\mathrm{kT}_{\mathrm{k}}}{\mathrm{m}}},$$

where m is the mass of the atom or molecule and T_k is the kinetic temperature of the gas.

The natural broadening produces the *natural line width* $\Delta\mathrm{v}_{\mathrm{i}}$ which arises from the uncertainty in energy of the states involved in the transition. The emitted photons will have a range of possible frequencies given by:

$$\Delta\nu_{\mathrm{i}} \approx \frac{\Delta E}{h} \approx \frac{1}{2\pi\Delta t},$$

where ΔE is the energy difference for the transition, and Δt is the lifetime of the excited state.

The non-thermal broadening is dominated by turbulent motions of the gas or by the presence of outflows or inflows. This is called the *turbulent width* Δv_{nt}. This is the mechanism that usually dominates the observed line-width from molecular clouds.

In general, the line profile can be described as a Gaussian with a line-width described as:

$$\Delta v_{obs} = (\Delta v_{th}^2 + \Delta v_i^2 + \Delta v_{nt}^2)^{1/2}$$

The analysis of the width of a detected molecular line gives information about the kinematics inside a molecular cloud.

Each molecular transition happens at a determined frequency. A Doppler shift between this frequency and the central frequencies of a detected molecular line is due to the radial velocity of the molecular cloud in the Galaxy. From this radial velocity and the position in the sky of the molecular cloud a kinematic distance toward the molecular cloud can be determined.

Moment map analysis

The moment map analysis is generally used to characterize the molecular line emission (Sault et al. 1995), since it gives an easy way to visualize and interpret the observations. If several lines are observed this method allows us to characterise the emission at every point across the map and to easily compare the emission between the different molecular transitions. The three principal moment maps used are the Zeroth, First and Second.

The Zeroth moment, M_0, or integrated intensity, is defined as:

$$M_0 = \int T_A^*(v) dv,$$

where $T_A^*(v)$ is the measured brightness at velocity v. The Zeroth moment reveals where the molecular line emission arises within the observed source.

The First moment, M_1, or intensity weighted velocity field, defined as:

$$M_1 = \frac{\int T_A^*(v) v dv}{\int T_A^*(v) dv},$$

reveals the mean velocity at each position within the source. It is useful to determine if different regions of the source have different kinematics.

The Second moment, M_2, or intensity weighted velocity dispersion, defined as:

$$M_2 = \sqrt{\frac{\int T_A^*(\mathrm{v})(\mathrm{v} - \mathrm{M}_1)^2 \mathrm{dv}}{\int T_A^*(\mathrm{v}) \mathrm{dv}}},$$

reveals the variation of the linewidth within the source. It is useful to identify regions where the turbulence is high.

Physical parameters derived from observations

Mass from virial equilibrium analysis: The mass of a molecular cloud can be estimated from the virial theorem, assuming that the cloud is in equilibrium between the potential energy and the kinetic energy inside the molecular cloud. The mass obtained from this method is called virial mass. For a spherical cloud of radius R, the virial mass, M_{vir}, in solar masses is:

$$M_{vir} = 210 \beta \Delta \mathrm{v}^2 \mathrm{R},$$

where Δv is the line-width in $km\ s^{-1}$, R is in pc, and β is a constant which depends on the density profile of the cloud ($\beta = 1$ for a uniform density core; $\beta = 0.9$ for one whose density varies as the inverse first power of the radius MacLaren et al. 1988).

Chapter 2

Aims and observations

2.1 Thesis aims

Despite significant efforts to understand the formation of massive, clustered stars, we lack a clear understanding about the processes involved. To understand better these phenomena we need to constrain the massive star formation scenarios through observations of the very early stages of star formation, characterizing Massive and Dense Cold Clumps (MDCCs). Clumps which are on the verge of forming protostars, but have not formed any yet, must still reflect the initial conditions of the formation of protoclusters. Searching and studying such objects is crucial for our understanding of star formation. Determination of the density, mass distribution and kinematics of the gas within these young MDCCs is crucial to unveil the processes involved.

The goal of this thesis is to better understand the nature of MDCCs and the way in which they fragment into seeds that will therefore form high-mass stars. The specific aims of this thesis are:

- Search for signatures of global collapse in the large scale of MDCCs.
- Study, with high angular resolution, the distribution of the mass within MDCCs into protostellar fragments and the kinematics of the gas .

To achieve these goals we used low and high angular resolution data (described in 2.2) to study the behaviour of the gas and dust from large to small scales within MDCCs and constrain the processes involved in high-mass star formation. The objects selected are described in the following section.

2.1.1 Source selection

We observed four massive and dense cold clumps (MDCC) discovered in a dust continuum emission survey towards luminous IRAS sources (Garay et al. 2004). These MDCC were

identified by having a large flux density at millimetre wavelengths, implying that they are massive, and by being undetected at mid-infrared (MSX) and far-infrared (IRAS) wavelengths, implying that they are cold. These conditions suggest that the four MDCC are close to the initial conditions expected for massive star formation, hence are ideal to study the early stages of massive star formation. The observed clumps are listed in Table 2.1.

Table 2.1: Coordinates of the four massive and dense cold clumps (MDCCs) observed with the APEX telescope.

Source	α (J2000)	δ (J2000)	Distance (kpc)
G305.136+0.068	13:10:41.7	-62:43:15.5	3.4
G333.125-0.562	16:21:34.9	-50:41:10.2	3.5
G18.606-0.076	18:25:08.7	-12:45:26.9	3.7
G34.458+0.121	18:53:19.8	+01:28:21.8	3.8

Figure 2.1 shows the *Spitzer*/IRAC three colour images (3.6 μm, 4.5 μ m, and 8.0 μ m) of the four clumps overlaid with contours of the *Herschel* dust continuum emission (250μm). We clearly see the dense clumps in the dust continuum and in the IR as dark structures. The clumps show a range in star formation activity: from G18.606-0.076, which is dark in the IR, to G34.458+0.25, which shows evidence for embedded star formation.

2.2 The data

2.2.1 Single dish observations

We made molecular line observations using the 12m Atacama Pathfinder Experiment (APEX) located in Llano de Chajnantor, Chile. The observations were carried out during May and July 2012 with the SHeFI instrument (Swedish Heterodyne Facility Instrument). A detailed description of the characteristics of APEX is given by Güsten et al. (2006). The frontend consisted of a single pixel heterodyne SiS operating in the 270 GHz band. The backend used was the eXtended Fast Fourier Transform Spectrometer (XFFTS). The half-power beam width of the telescope at 345 GHz is ∼20". The main beam efficiency is 0.73. We observed 3 spectral windows, for each of the clumps, centered at the frequencies of 267.6, 272 and 279.5 GHz each with 2.5 GHz bandwidth and 76 kHz (0.09 kms^{-1}) channels. This setup was chosen to map the emission in the HCO^+ (3-2), HNC (3-2) and N_2H^+ (3-2) lines. The bandwidth used to observe the HCO^+ (3-2) line also contained the HCN (3-2) and CH_3OH (5-4) lines, and the one used to observe the N_2H^+ (3-2) line, contained the CH_3OH (9-8) line. These transitions were chosen for the following reasons. The N_2H^+ molecule suffers little depletion and is one of the best probes of the coldest and densest gas (e.g. Caselli et al. 2002; Crapsi et al. 2007) thus a good tracer for physical conditions and kinematics of the densest and coldest gas of the clump, and the HNC and HCO^+ molecules to study the kinematics of neutral and molecular

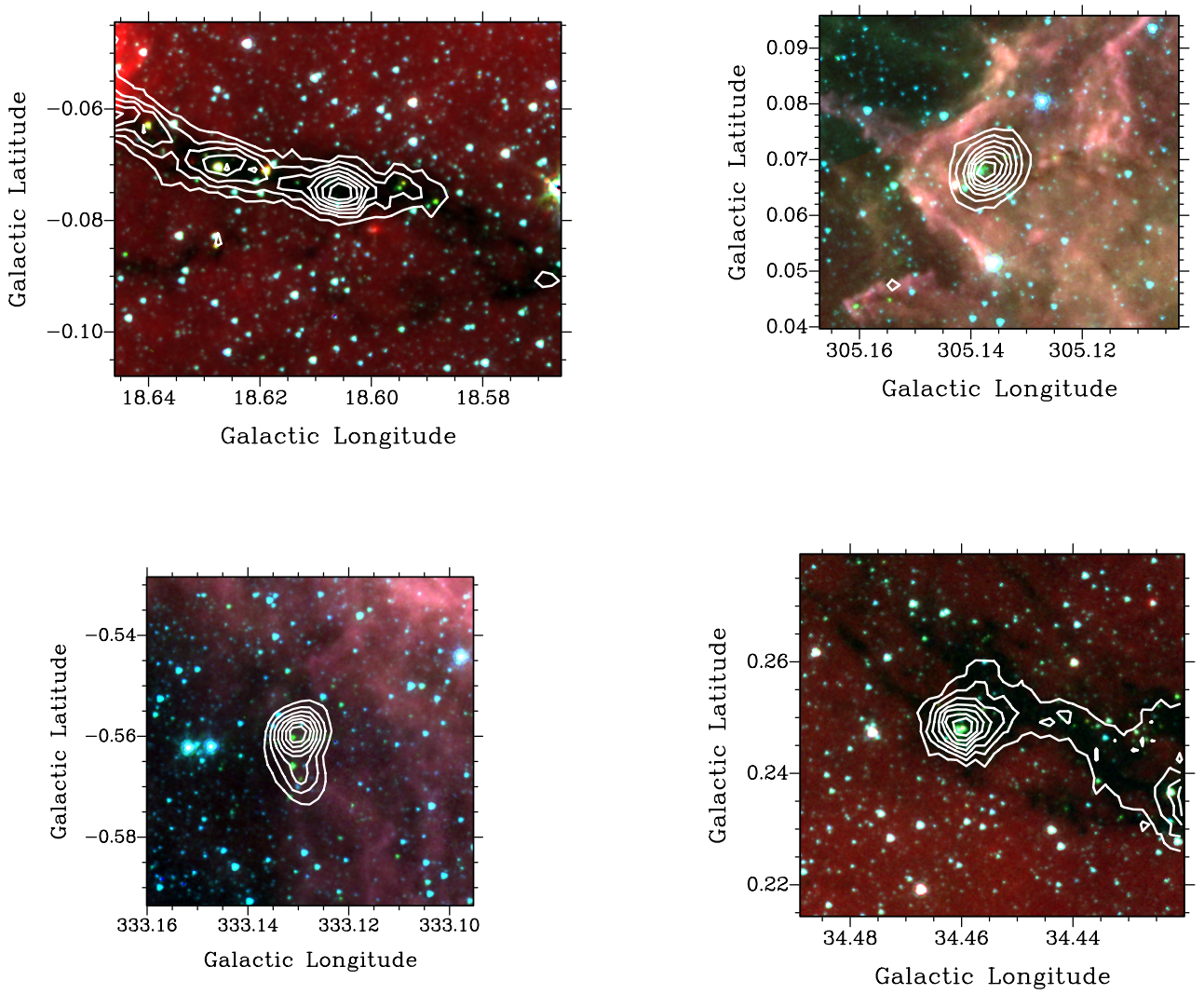

Figure 2.1: Spitzer-IRAC three-color images (3.6 μm = blue, 4.5 μm = green, and 8.0 μm = red) of the four MDCC showing different star formation activity, increasing from the top left to the bottom right. Overlaid are contours of the dust emission (ATLASGAL 870μm; levels are drawn at 30%, 40%, 50%, 60%, 70%, 80%, and 90% of the peak value). From top left to bottom right: G18.606-0.076, G305.136+0.068, G333.125-0.562, G34.458+0.25.

Table 2.2: Summary of the observed molecular transitions with the APEX telescope.

Molecular transition	Frequency (GHz)	E_u/k (K)	n_{crit} (cm^{-3})
HCN v=0 J=3-2	265.886	25.52	8×10^6
CH_3OH v=0 J=5-4	266.838	57.07	2.6×10^6
HCO^+ v=0 J=3-2	267.558	25.68	1.6×10^7
HNC v=0 J=3-2	271.981	26.11	1×10^7
CH_3OH v=0 J=9-8	278.305	109.97	2.6×10^6
N_2H^+ v=0 J=3-2	279.512	26.83	1.3×10^7

ion gas (information about the transitions, critical densities and excitation energies are given in Table 2.2). We mapped regions of 120"x120" for G305.136+0.068 and regions of 100"x100" for G18.606-0.076, G333.125-0.562 and G34.458+0.25. The maps were made with angular spacings of 20" and centered at the peak of the dust core (listed in table 2.1).The on-source integration time per position was ∼3 min for G305, ∼2 min for G333, G18 and G34. All the observations were carried out under good weather conditions (PWV < 1.3 mm).

All data reduction was performed using the CLASS software package. Each data set was calibrated on-line by the OnlineCalibrator program, which writes the calibrated spectra into a CLASS-format data file. Following the calibration an inspection, average and a base-line fitting were made. The final dataset have an angular resolution of ∼20", with an rms of 0.4 K.

2.2.2 ALMA observations

We observed, using Atacama Large Millimeter/submillimeter Array (ALMA), the 3 mm (90 GHz) dust continuum and molecular line emission toward G305.136+0.068. The observations were carried out, as part of ALMA Cycle 1, between April 25-28 2014 using both the 12-m array and the Compact Array (ACA, 7m antennas). Because ALMA's field of view at this wavelength is $\sim 52.6''$ and the cloud covers a region $> 50''$, a 3-point mosaic with Nyquist sampling was needed to cover its full extent. We observed 4 spectral windows in dual polarization mode centered at the frequencies of 89.2, 93.2, 98.0 and 110.2 GHz each with 234.4 MHz bandwidth and 122.1 kHz (0.4 kms^{-1}) channels. This setup was chosen to map the emission in the HCO^+ J=1-0, CS J=2-1, ^{13}CO J=1-0 and N_2H^+ J=1-0 lines. The HCO^+, CS and N_2H^+ molecules were chosen for the following reasons. The N_2H^+ molecule suffers little depletion and is one of the best probes of the coldest and densest gas (e.g. Caselli et al. 2002; Crapsi et al. 2007), HCO^+ is a good tracer of conditions within the larger scale surroundings and CS is a good tracer of lower-density material in outflows (information about the transitions, critical densities and excitation energies are given in Table 2.3). To map the 3mm dust continuum emission a set of 3 spectral windows were observed, centered at the frequencies of 91.2, 103.2 and 104.9 GHz each with a 1875 MHz bandwidth, also in dual polarization mode, with a coarser frequency resolution channel spacing of 976.6 kHz (∼3 kms^{-1}).

Table 2.3: Summary of the molecular transitions observed with the ALMA interferometer.

Molecular transition	Frequency (GHz)	E_u/k (K)	n_{crit} (cm^{-3})
HCO^+ v=0 J=1-0	89.189	4.28	$1.4x10^6$
N_2H^+ v=0 J=1-0	93.173	4.47	$1.3x10^6$
CS v=0 J=2-1	97.981	7.05	$5.7x10^5$
^{13}CO v=0 J=1-0	110.201	5.29	$2x10^3$

We used a combination of the 12m and 7m arrays to recover the emission from angular scales from 2″ to 40″. The projected baselines ranged from 18-490m for the 12m array and from 8-37m for the 7m array. All data reduction was performed using the CASA software package. Each data set was independently calibrated (by our ALMA support scientist) before being merged. The proceeding for merging the data is as follows. We first concatenated the 12-m and 7-m data with an equal weighting of 1. Then, we applied a weight to the data based on the visibility scatter and we cleaned and imaged the product. The final merged dataset have an angular resolution of ∼2" (0.03 pc), with a 1σ continuum sensitivity of ∼ 120 μJy beam^{-1} and a line brightness sensitivity of 18 mJy beam^{-1} per channel for the high velocity resolution data (0.4 kms^{-1}) and 1.9 mJy beam^{-1} per channel for the coarser velocity resolution data (∼3 kms^{-1}).

Chapter 3

Large scale (∼0.3 pc) properties of the gas

3.1 Results

Table 3.1 shows a list of the chemical species detected towards each of the four clumps. In addition to the aimed chemical species, HCN(3-2), HCO^+(3-2) , HNC(3-2) and N_2H^+(3-2), we also detected fainter emission in two transitions of methanol, CH_3OH, towards all the clumps with the exception of G18.606-0.076 where only the lower frequency transition was detected.

Figures 3.1-3.4 show spectral maps of the HCN(3-2), HCO^+(3-2), N_2H^+(3-2), HNC(3-2), CH_3OH(5-4) and CH_3OH(9-8) line emission observed toward G305.136+0.068, G333.125-0.562, G18.606-0.076 and G34.458+0.121 respectively. The spacing is 20" for all transitions. Offsets are measured from the reference positions given in Table 2.1.

Table 3.1: Molecular lines detected towards each of the observed clumps.

Molecule	Transition	Frequency (GHz)	E_u/k (K)	n_c (cm^{-3})	G305	G333	G18	G34
HCN v=0	3-2	265.886	25.52	8×10^6	√	√	√	√
HCO^+ v=0	3-2	267.558	25.68	1.6×10^7	√	√	√	√
HNC v=0	3-2	271.512	26.11	1×10^7	√	√	√	√
N_2H^+ v=0	3-2	279.512	26.83	1.3×10^7	√	√	√	√
CH_3OH v=0	5(2,3)-4(1,3)	266.838	57.07	2.6×10^6	√	√	√	√
CH_3OH v=0	9(-1,9)-8(0,8)	278.305	109.97	2.6×10^6	√	√	···	√

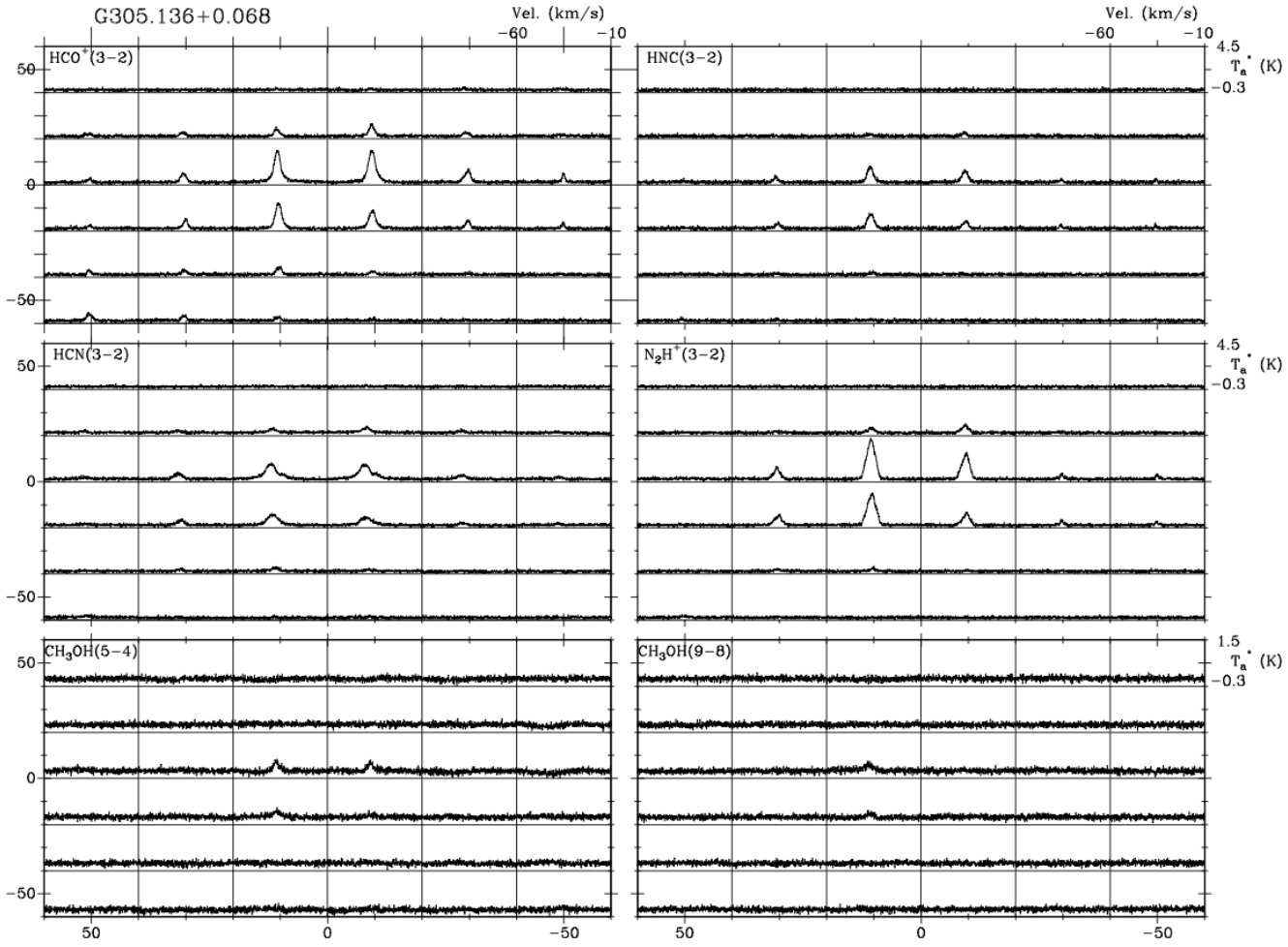

Figure 3.1: Spectral maps of HCO^+(3-2), HNC(3-2), HCN(3-2), N_2H^+(3-2), CH_3OH(5-4) and CH_3OH(9-8) molecular line emission toward G305.136+0.068. The grid spacing is 20". The velocity scale ranges from -60 to -10 km/s. The antenna temperature scale ranges from -0.3 to 4.5 K for all molecules, except for the CH_3OH transitions where it ranges from -0.3 to 1.5 K.

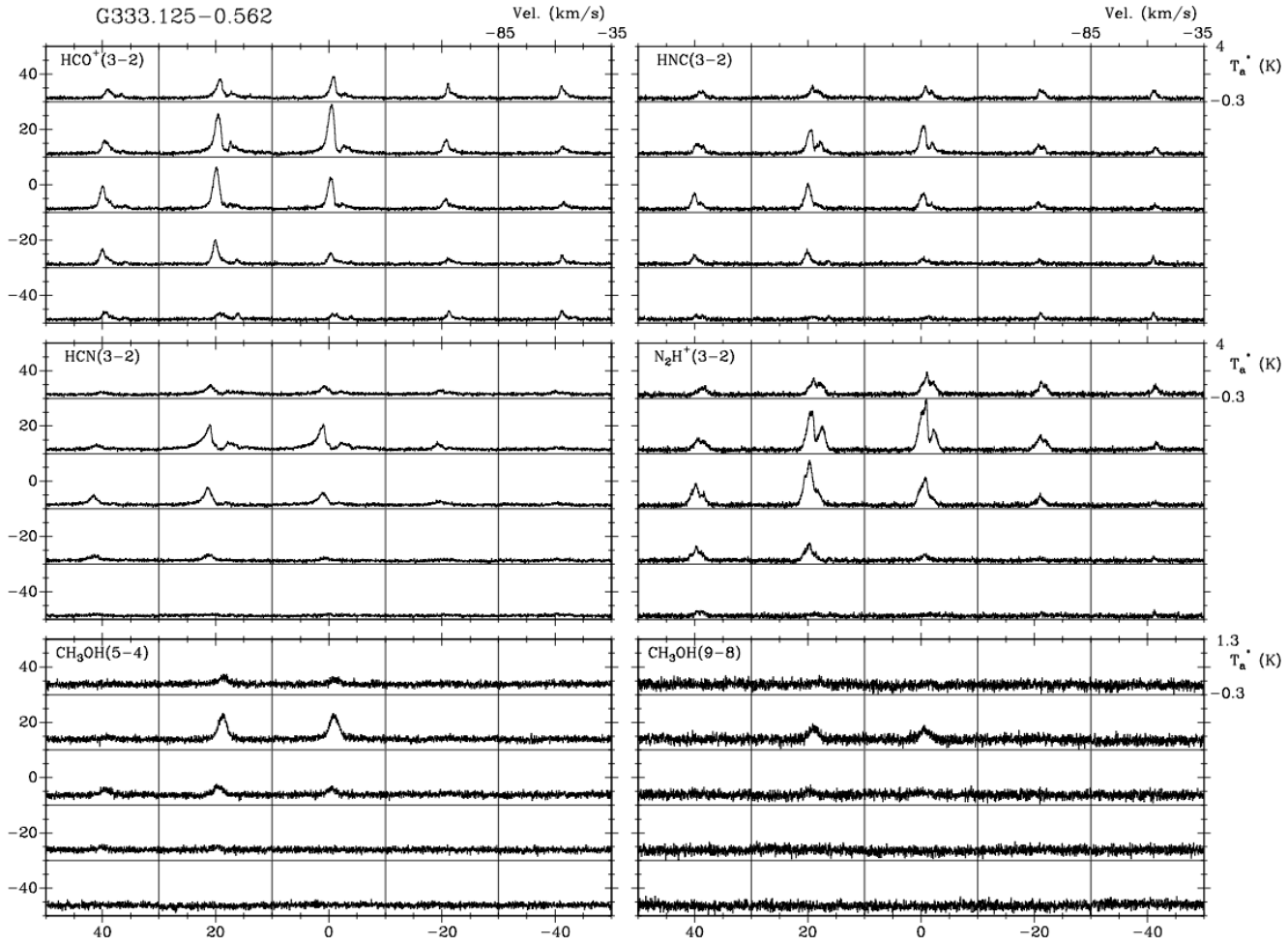

Figure 3.2: Spectral maps of HCO^+(3-2), HNC(3-2), HCN(3-2), N_2H^+(3-2), CH_3OH(5-4) and CH_3OH(9-8) molecular line emission toward G333.125-0.562. The grid spacing is 20". The velocity scale ranges from -85 to -35 km/s. The antenna temperature scale ranges from -0.3 to 4 K for all molecules, except for the CH_3OH transitions where it ranges from -0.3 to 1.3 K.

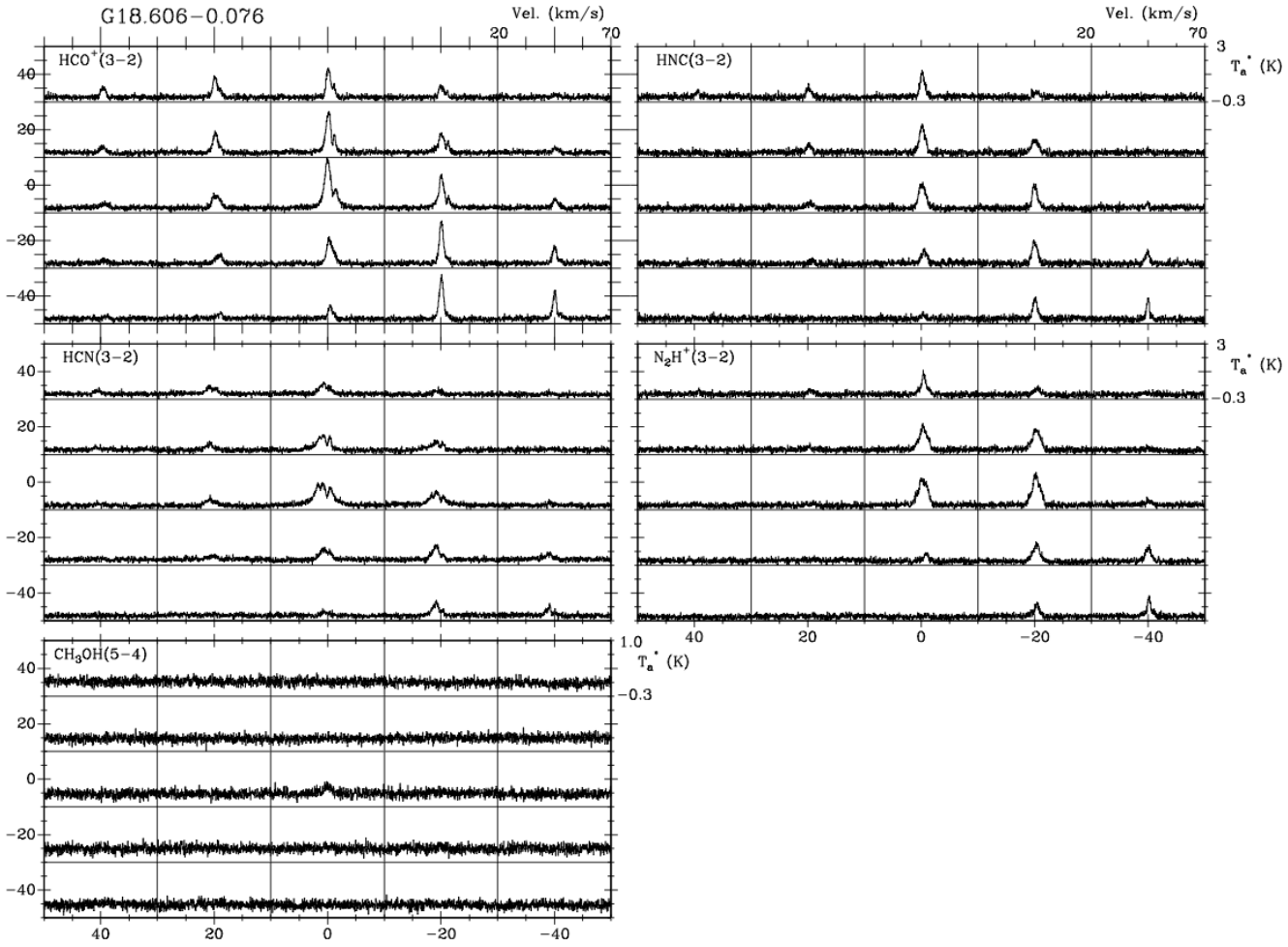

Figure 3.3: Spectral maps of HCO^+(3-2), HNC(3-2), HCN(3-2), N_2H^+(3-2) and CH_3OH(5-4) molecular line emission toward G18.606-0.076. The grid spacing is 20". The velocity scale ranges from 20 to 70 km/s. The antenna temperature scale ranges from -0.3 to 3 K for all molecules, except for CH_3OH(5-4) where it ranges from -0.3 to 1 K.

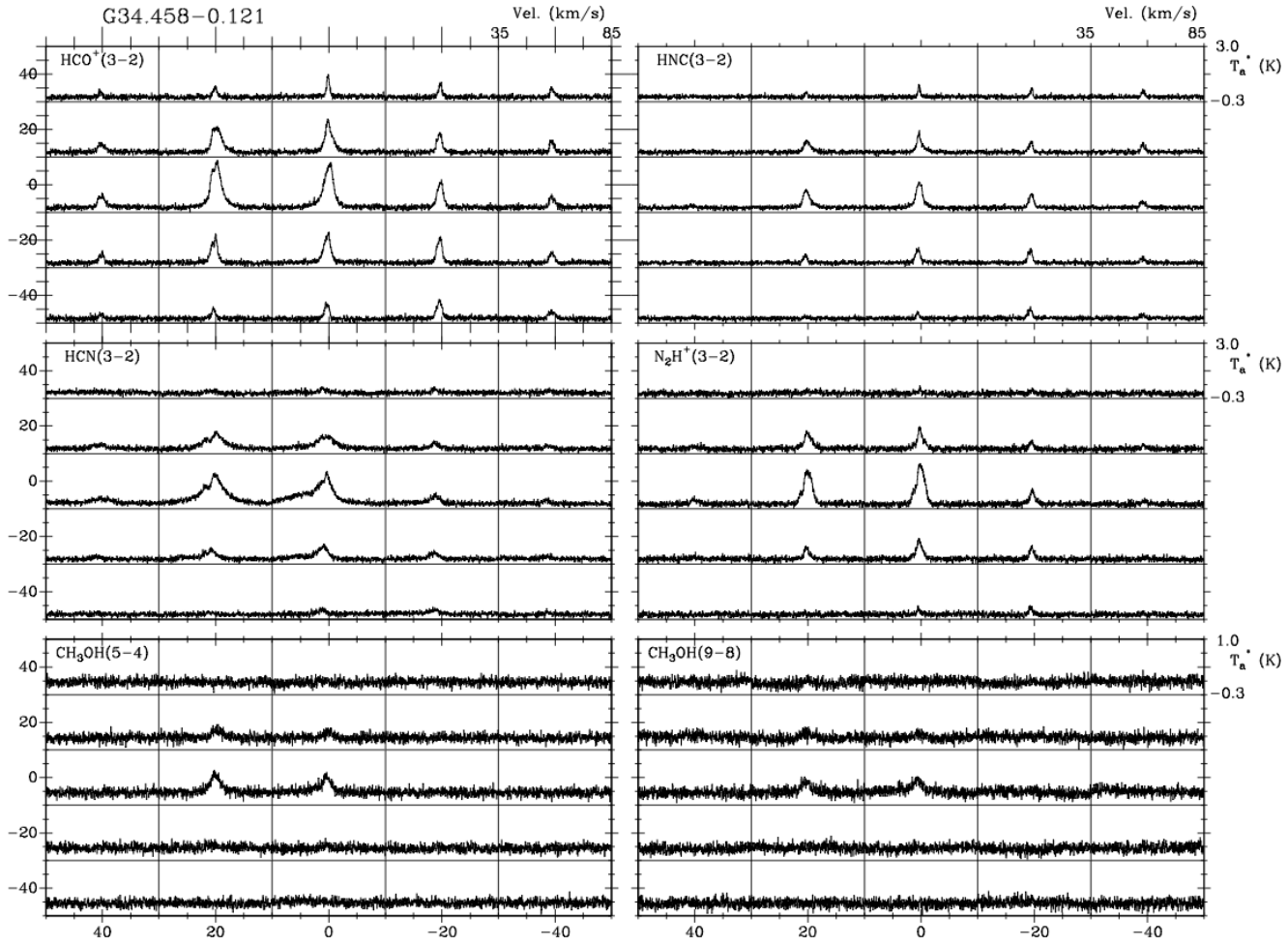

Figure 3.4: Spectral maps of HCO^+(3-2), HNC(3-2), HCN(3-2), N_2H^+(3-2), CH_3OH(5-4) and CH_3OH(9-8) molecular line emission toward G34.458+0.121. The grid spacing is 20". The velocity scale ranges from 35 to 85 km/s. The antenna temperature scale ranges from -0.3 to 3 K for all molecules, except for the CH_3OH transitions where it ranges from -0.3 to 1 K.

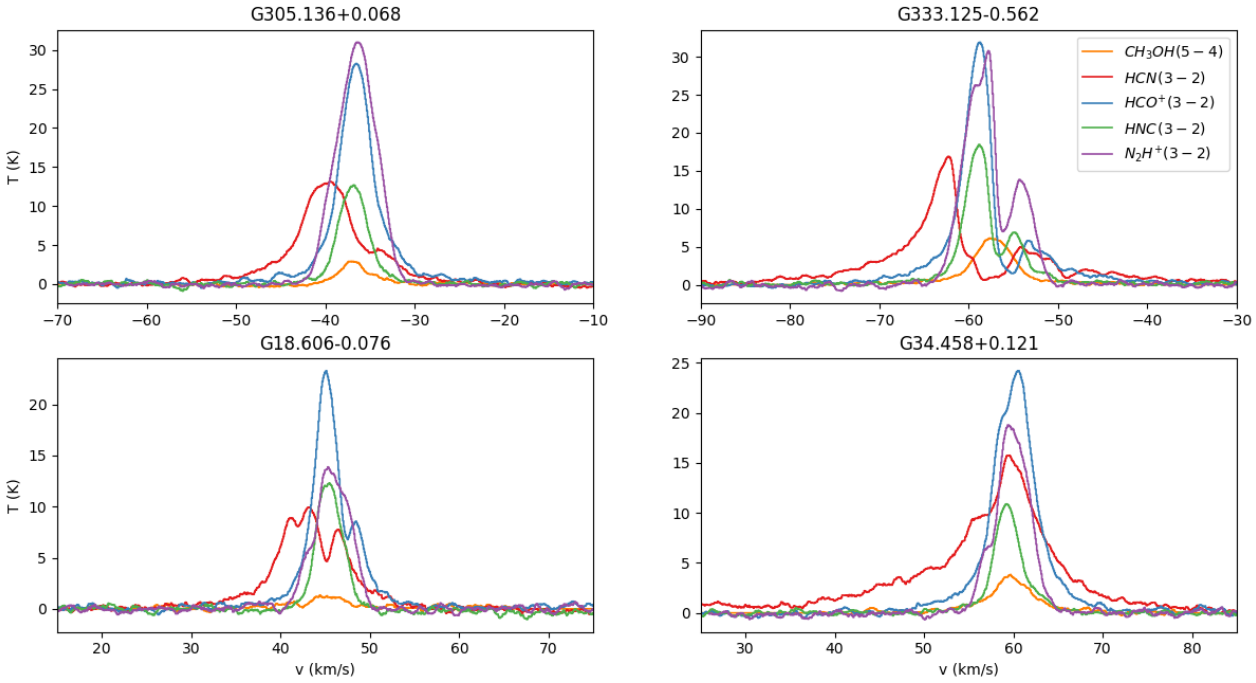

Figure 3.5: Spectra of CH_3OH(5-4) (orange), HCN(3-2) (red), HCO^+(3-2) (blue), HNC(3-2) (green) and N_2H^+(3-2) (purple) emission observed at the peak position of G305.136+0.068, G333.125-0.562, G18.606-0.076 and G34.458+0.121.

3.1.1 Line profiles

G305.136+0.068 is the clump that shows less complex line profiles (see Figure 3.1). The profiles of the HCO^+, HNC and CH_3OH emission are nearly gaussian. The profile of the N_2H^+ emission is triangular (Figure 3.1) due to the hyperfine structure which gives rise to 7 different lines (Caselli et al. 2002). G333.125-0.562, G18.606-0.076 and G34.458+0.121 show multiple line-shape features as self-absorption and high-velocity wings. This can also be seen in Figures 3.5 and 3.6 which show the spectra of all the molecular lines observed at the peak position and integrated over each clump, respectively.

Table 3.3 lists for each clump the observed parameters (antenna temperature, line center velocity, velocity dispersion, and velocity integrated antenna temperature) of the lines with nearly Gaussian profiles. Two sets of values are shown, one for the line emission observed at the peak position and the other for the spatially averaged emission, all of them determined from Gaussian fittting to the respective line profiles. The profiles of the emission in the HCO^+, HCN and HNC lines towards G333 and HCO^+ and HCN towards G18 show strong self-absoprtion features and hence Gaussian fits are unwarranted. Table 3.4 lists for G305, G18 and G34 the results of the hyperfine structure fitting of the N_2H^+(3-2) (line center velocity, velocity dispersion, and opacity) for the peak position and for the spatially averaged emission. The fit was done using the CLASS program hfs. The frequencies and relative intensities of the 7 hyperfine components were retrieved from the Cologne Database for

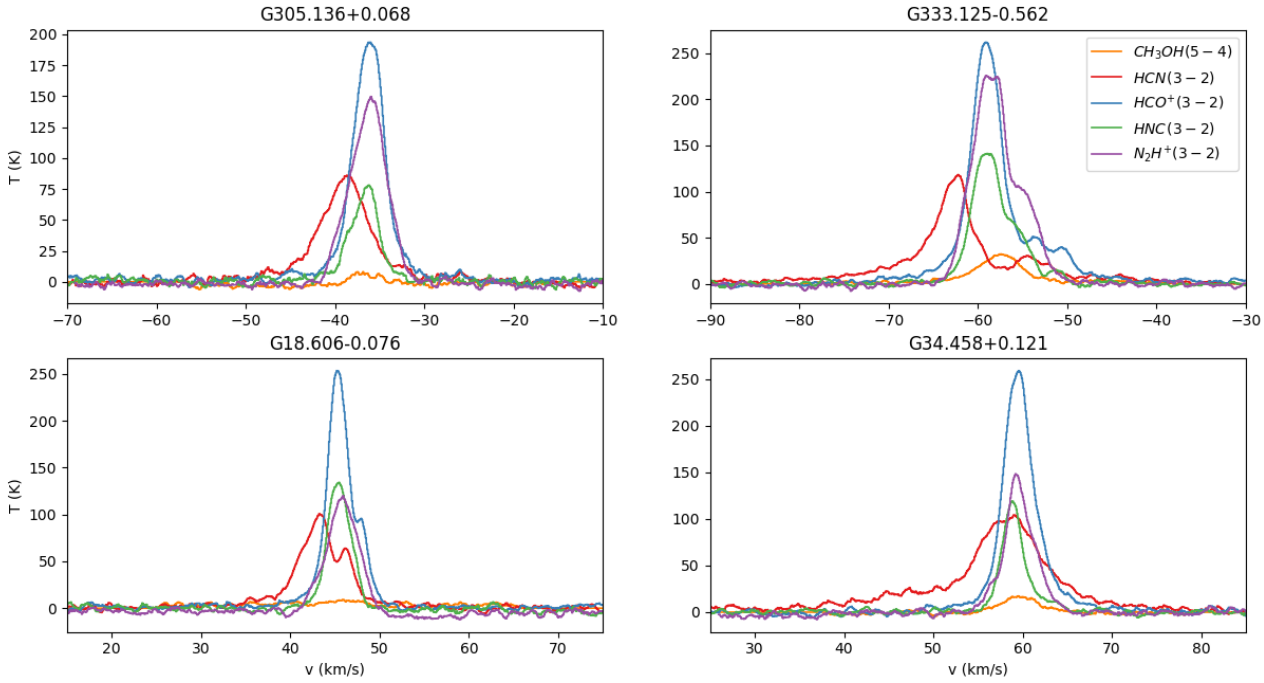

Figure 3.6: Integrated spectra of CH_3OH(5-4) (orange), HCN(3-2) (red), HCO^+(3-2) (blue), HNC(3-2) (green) and N_2H^+(3-2) (purple) emission toward G305.136+0.068, G333.125-0.562, G18.606-0.076 and G34.458+0.121.

Molecular Spectroscopy (Müller et al. 2001, Müller et al. 2005). The line widths are much larger than the thermal width expected for a clump with T ∼15 K, indicating that these clumps are highly turbulent. Column 10 of Table 3.3 and column 8 of Table 3.4 gives the FWHM angular size in the four observed transitions obtained through a two dimensional Gaussian fitting of the integrated intensity map for each case.

To characterize the emission we made moment analysis of the data (Sault et al. 1995) as detailed in the introduction. The moment analysis allows us to characterise the emission at every point across the map and to easily compare the emission between the different molecular transitions. The moment maps were calculated taking a velocity window of 60 km/s, centered at the line velocity for each case. To include only the highest signal-to-noise emission in this moment analysis we considered only positions across the clumps where the emission was above an intensity threshold of $\sim 3\sigma$.

Figure 3.7 shows images of the M_0 (integrated intensity), M_1 (intensity weighted velocity field), and M_2 (intensity weighted velocity dispersion) moments of the HCN(3-2), HCO^+(3-2), N_2H^+(3-2) and HNC(3-2) emission toward G305.136+0.068. Overlaid on the M_1 and M_2 images are contours of the integrated intensity to highlight the relation between the intensity of the emission of the gas and its kinematics. Figures 3.8-3.10 show images of the M_0 (integrated intensity) moments of the HCN(3-2), HCO^+(3-2), N_2H^+(3-2) and HNC(3-2) emission toward G333.125-0.562, G18.606-0.076 and G34.458+0.121 respectively. These three clumps show complex kinematics, hence the M_1 (intensity weighted velocity field), and

M_2 (intensity weighted velocity dispersion) moments are shown only for the molecules with Gaussian-shaped profiles.

The integrated intensity maps show that the HCO^+ emission is more extended than the emission from the other molecules for all clumps. The peak of the emission of each line correlates well from line to line for each clump.

Table 3.3: Observed parameters of the HCN(3-2), HCO^+(3-2), HNC(3-2), CH_3OH(5-4) and CH_3OH(9-8) emission for G305.136+0.068, G333.125-0.562, G18.606-0.076 and G34.458+0.121 (if they follow a Gaussian-like shape). The first column lists the molecule, columns 2-5 list, respectively, the antenna temperature, line center velocity, velocity dispersion and velocity integrated antenna temperature at the peak emission; columns 6-9 list, respectively, the antenna temperature, line center velocity from, sigma and velocity integrated antenna temperature of the source averaged emission, and column 10 the FWHM angular size.

	Peak				Average				
	T_A (K)	v (km s^{-1})	Δv (km s^{-1})	$\int T_A$dv (K km s^{-1})	T_A (K)	v (km s^{-1})	Δv (km s^{-1})	$\int T_A$dv (K km s^{-1})	θ_{obs} (arcsec)
(1)	(2)	(3)	(4)	(5)	(6)	(7)	(8)	(9)	(10)
G305.136+0.068									
HCO^+(3-2)	3.3	-36.6	4.5	16.0	0.6	-36.2	4.0	2.5	36.3
HNC(3-2)	1.7	-36.9	4.0	7.1	0.2	-36.7	3.8	0.9	25.8
CH_3OH (5-4)	0.3	-36.8	4.3	1.6	0.2	-36.8	4.5	1.1	34.3
CH_3OH (9-8)	0.2	-36.5	5.4	1.2	0.2	-36.1	4.7	0.9	24.1
G333.125-0.562									
CH_3OH (5-4)	0.7	-57.4	5.3	3.8	0.09	-57.5	5.3	3.8	41.1
CH_3OH (9-8)	0.3	-56.8	5.9	1.7	0.2	-56.7	5.5	1.1	39.2
G18.606-0.076									
N_2H^+(3-2)	1.8	45.8	4.5	8.7	0.5	45.9	4.2	2.4	37.4
HNC(3-2)	1.6	45.5	3.1	5.1	0.6	45.5	3.1	2.0	60.9
CH_3OH (5-4)	0.2	45.3	3.9	0.7	0.02	46.0	3.8	0.07	37.8
G34.458+0.121									
HCO^+(3-2)	2.7	60.2	5.4	15.8	1.1	59.6	4.0	4.8	47.6
N_2H^+(3-2)	2.4	59.9	4.5	11.2	0.6	59.6	4.0	2.6	35.9
HNC(3-2)	1.4	59.4	3.5	5.3	0.5	58.9	2.8	1.6	29.7
CH_3OH (5-4)	0.4	60.2	6.2	2.6	0.05	59.6	4.8	0.3	38.4
CH_3OH (9-8)	0.2	60.5	5.6	1.3	0.04	60.1	4.6	0.2	37.9

3.1.2 Velocity fields

The line profiles indicate different kinematic signatures for the clumps. G305.136+0.068 exhibits the simpler profiles (shown in Figure 3.1) with Gaussian like lines and absence of prominent high velocity wings, suggesting that is in an earlier stage of evolution. The line profiles of the other three clumps (Figures 3.2, 3.3 and 3.4) exhibit high velocity wings and multiple peaks in several of the detected lines, suggesting complex large-scale kinematics.

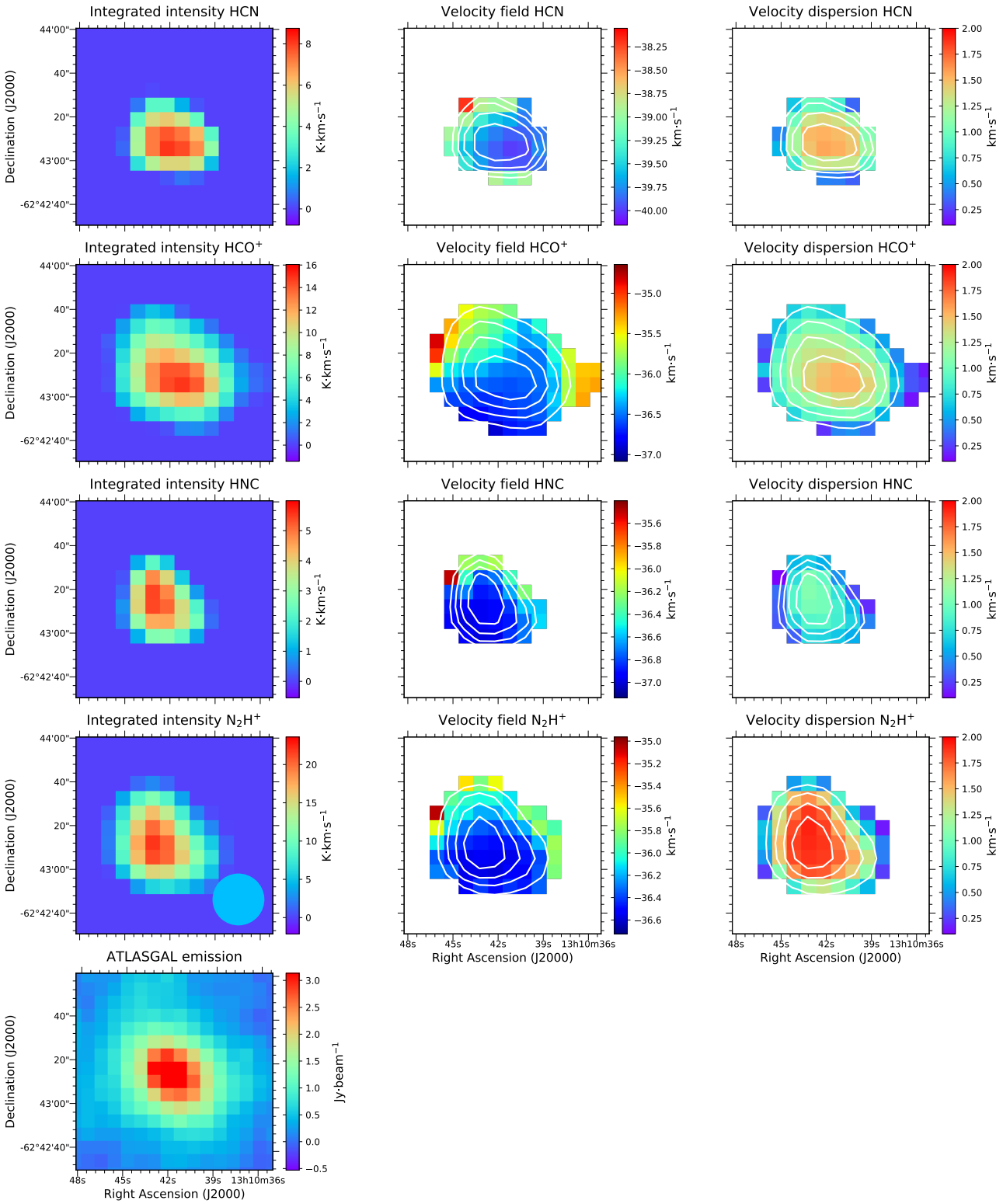

Figure 3.7: G305.136+0.068 moment maps of the HCN(3-2), HCO^+(3-2) , HNC(3-2) and N_2H^+(3-2) emission (from top to bottom). The bottom left panel shows the ATLASGAL continuum emission. The panels from left to right: integrated intensity (zeroth moment, units of K kms^{-1}), intensity weighted velocity field (first moment, units of kms^{-1}), intensity weighted velocity dispersion (second moment, units of kms^{-1}). Overlaid with white contours are the contours of the integrated intensity (levels are 20, 40, 60 and 80% of the peak).

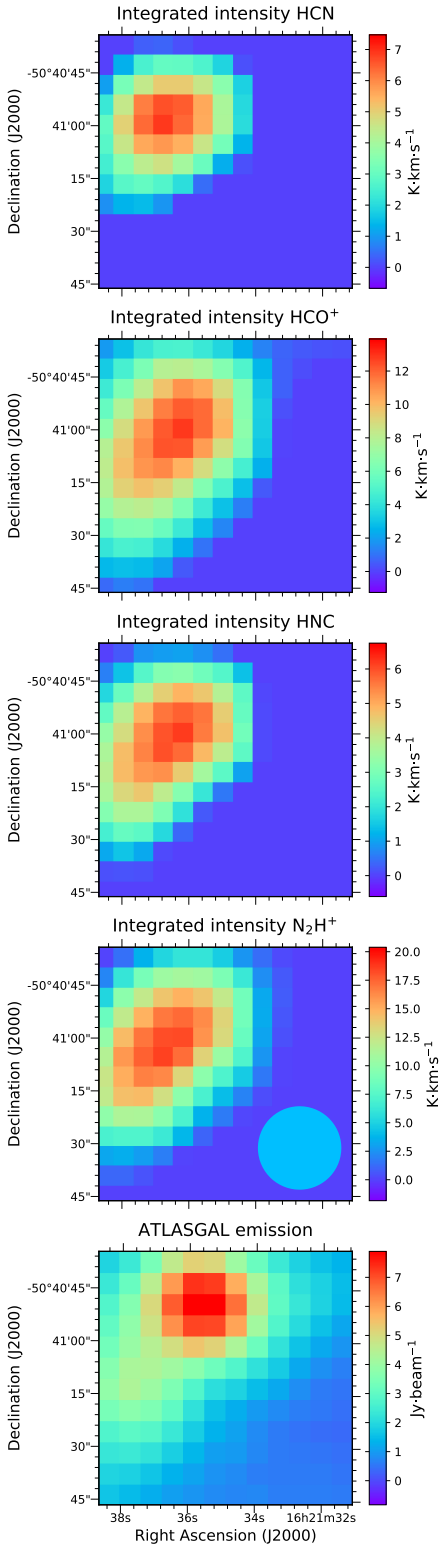

Figure 3.8: G333.125-0.562 integrated intensity moment maps (zeroth moment, units of K kms^{-1}) of the HCN(3-2), HCO$^+$(3-2) , HNC(3-2) and N_2H^+(3-2) emission (from top to bottom). The bottom left panel shows the ATLASGAL continuum emission.

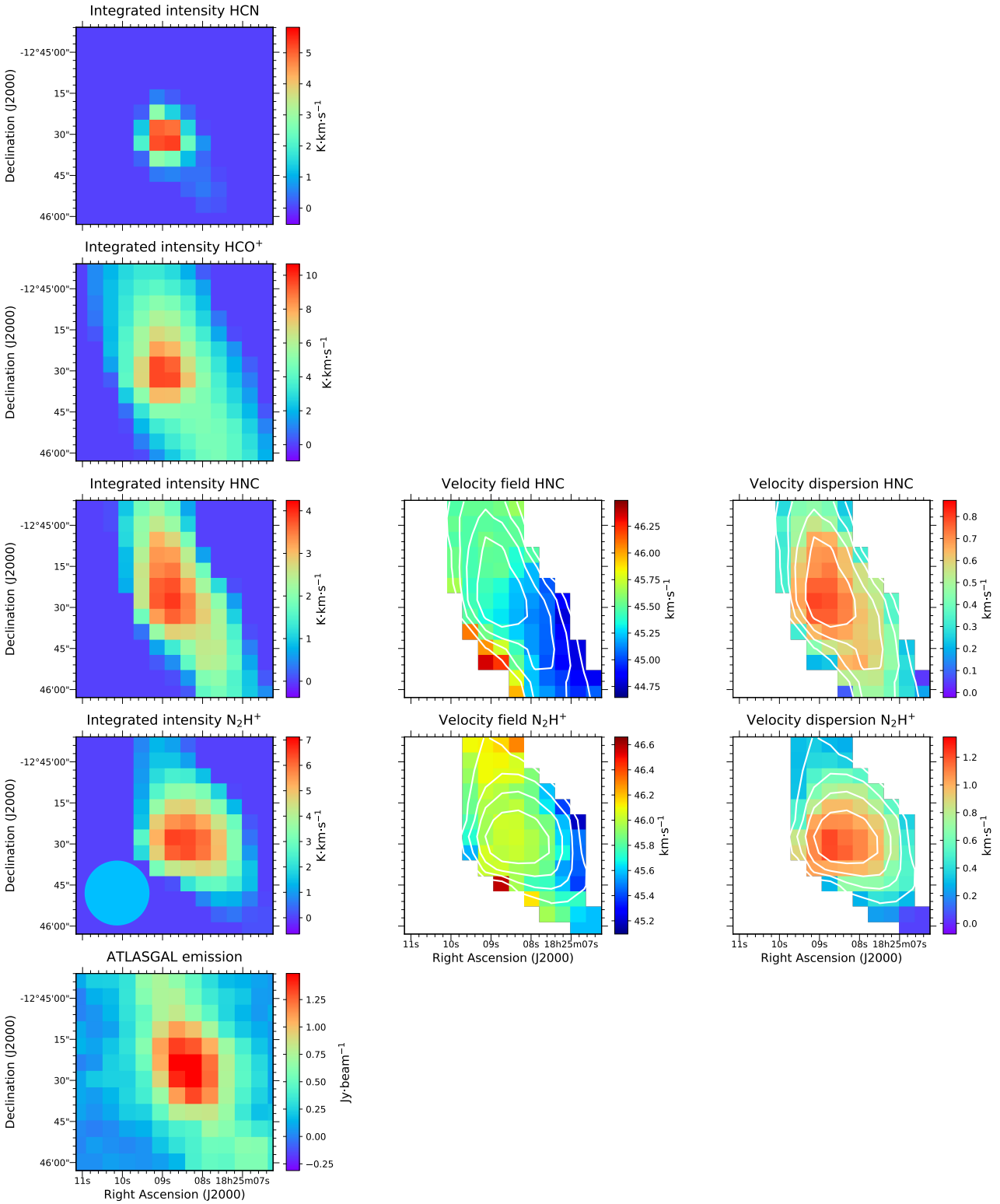

Figure 3.9: G18.606-0.076 integrated intensity moment maps (zeroth moment, units of K kms^{-1}) of the HCN(3-2), HCO$^+$(3-2) , HNC(3-2) and N_2H^+(3-2) emission (from top to bottom). The bottom left panel shows the ATLASGAL continuum emission. Also shown are the intensity weighted velocity field (first moment, units of kms^{-1}) and the intensity weighted velocity dispersion (second moment, units of kms^{-1}) for HNC(3-2) and N_2H^+(3-2). Overlaid with white contours are the contours of the integrated intensity (levels are 20, 40, 60 and 80% of the peak).

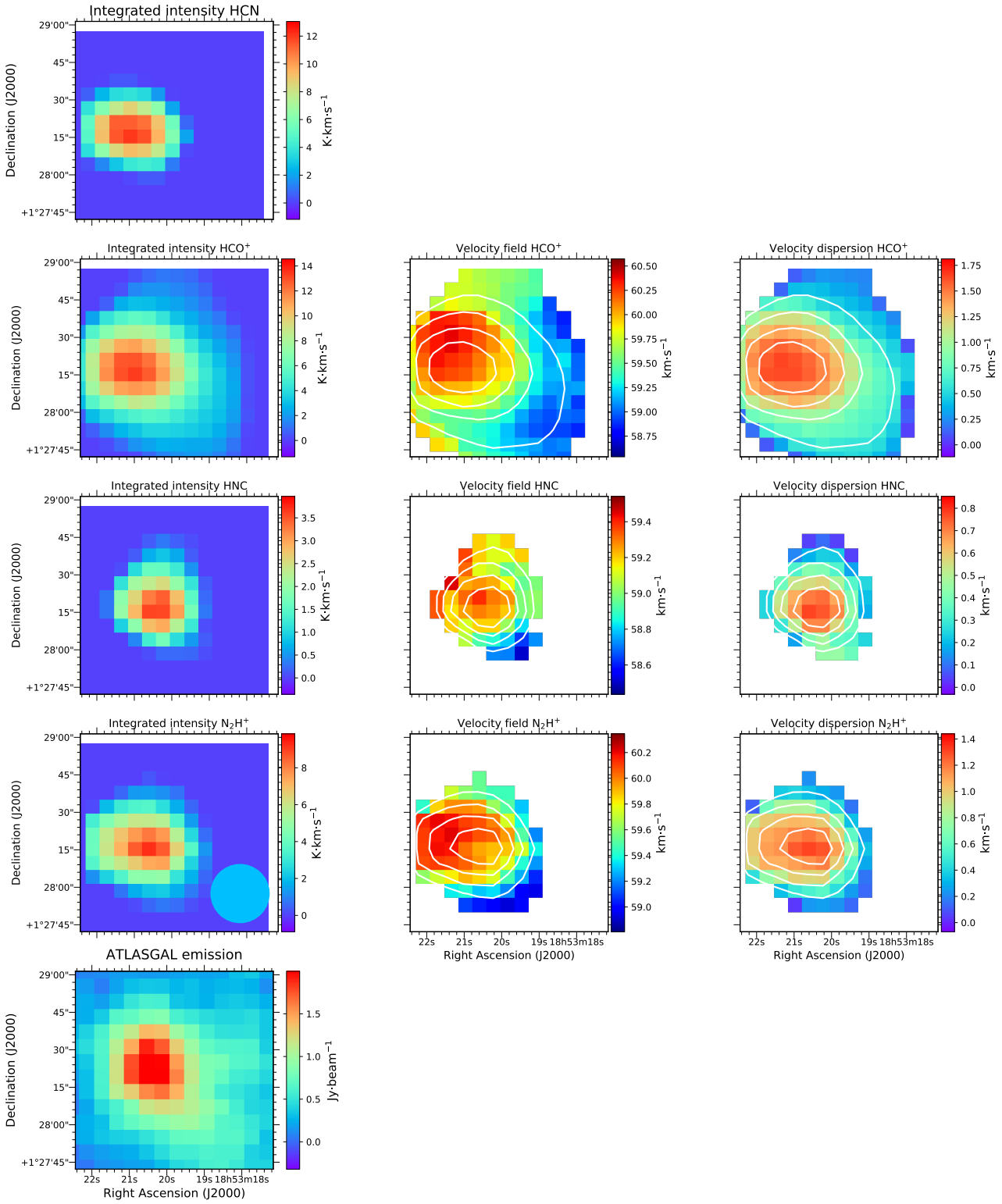

Figure 3.10: G34.458+0.121 integrated intensity moment maps (zeroth moment, units of K kms^{-1}) of the HCN(3-2), HCO$^+$(3-2) , HNC(3-2) and N_2H^+(3-2) emission (from top to bottom). The bottom left panel shows the ATLASGAL continuum emission. Also shown are the intensity weighted velocity field (first moment, units of kms^{-1}) and the intensity weighted velocity dispersion (second moment, units of kms^{-1}) for HCO$^+$(3-2), HNC(3-2) and N_2H^+(3-2). Overlaid with white contours are the contours of the integrated intensity (levels are 20, 40, 60 and 80% of the peak).

Table 3.4: Fitted parameters of the N_2H^+(3-2) emission for G305.136+0.068, G18.606-0.076 and G34.458+0.121. The fit was done using the CLASS program hfs for hyperfine structure. Columns 2-4 list, respectively, the line center velocity, velocity dispersion and opacity at the peak emission; columns 5-7 list, respectively, the line center velocity, velocity dispersion and opacity of the source averaged emission, and column 8 the FWHM angular size.

	Peak			Average			
	v (km s^{-1})	Δv (km s^{-1})	τ	v (km s^{-1})	Δv (km s^{-1})	τ	θ_{obs} (arcsec)
(1)	(2)	(3)	(4)	(5)	(6)	(7)	(8)
G305.136+0.068	-36.6	4.8	0.5	-36.3	4.6	<0.1	31.6
G18.606-0.076	45.6	4.0	<0.1	45.7	3.8	<0.1	37.4
G34.458+0.121	59.7	4.1	<0.1	59.4	3.7	<0.1	35.9

Moment maps gradients

The intensity weighted velocity field maps show some velocity gradients for G34.458+0.12 and G18.606-0.076. In the case of G34.458+0.12 a gradient of $\sim$ 1.5 km/s is seen in the HCO^+, HNC and N_2H^+ maps. For G18.606-0.076 a gradient is seen in the HNC and N_2H^+ maps. The structure of these gradients is not as defined as in the case of G34, maybe due to the elongated structure of this clump. The intensity weighted velocity dispersion maps show, for all analysed molecules and all clumps, a clear increase in the line width from the outer part of the clumps toward the central region.

Collapse signatures

Blue asymmetries in the profiles of optically thick molecular lines appear to be a signpost indicator of gas infall motions within cores (Myers et al. 1996), even when their shape is irregular (Chira et al. 2014). Radiative transfer models of molecular lines (Chira et al. 2014) have shown that among the best tracers of collapse motions are the (3-2) transitions of both HCN and HCO^+ molecules. Both of these transitions are typically optically thick.

In the case of G305.136+0.068 blue asymmetry is clearly seen in the HCN profile. Towards G333.125-0.562 all molecular lines, with exception of CH_3OH which is optically thin, show clear profiles with blue asymmetries. Towards G18.606-0.076 the kinematics look more complicated but there is line profile blue asymmetries for the HCN and HCO^+ molecules. There are no asymmetries shown towards G34.458+0.121. For G305.136+0.068 and G333.125-0.562 the N_2H^+ line peaks at the self-absorption dip from the HCN line. This behaviour is consistent with infall dynamics, as optical depth increases, the line develops a self-absorption dip between a brighter blue peak and a fainter red peak (Myers et al. 1996). As the infall velocity increases, the degree of asymmetry increases.

3.2 Discussion

Table 3.5: Derived physical parameters of MDCC. Columns from left to right: source name, average radius, average line-width, virial mass, dust mass and virial parameter.

Source	Radius (pc)	Δv (km/s)	M_{vir} ($M_\odot$)	M_{dust} ($M_\odot$)	α_{vir}
G305.136+0.068	0.25	3.9	8.0×10^2	1.1×10^3	0.9
G333.125-0.562	0.38	5.3	2.2×10^3	3.0×10^3	0.7
G18.606-0.076	0.40	3.1	8.1×10^2	5.6×10^2	2.0
G34.458+0.121	0.34	4.7	1.6×10^3	9.0×10^2	1.0

3.2.1 Virial Masses

To assess whether the clumps are gravitationally bound and unstable to collapse or unbound and transient, we determine the virial parameter, $\alpha_{\rm vir}$, defined as $\alpha_{\rm vir} = M_{\rm vir}/M_{\rm dust}$. The virial mass, $M_{\rm vir}$, is defined as $M_{\rm vir} = 210 \cdot \Delta {\rm v}^2 R$, where Δv is the measured line-width in units of km/s and R is the radius in units of pc. The radius of each clump was computed from the angular size, determined from a 2D Gaussian fit to the emission for each of the observed lines (listed in Table 3.3) assuming the clump distances given in Table 2.1. To estimate the line-widths we used different lines for each clump (mainly considering Gaussian like profiles). For G305.136+0.068 the lines used are HCO^+ and HNC, for G333.125-0.562 we used CH_3OH (5-4), for G18.606-0.076 we used the HNC value and finally for G34.458+0.25 we used both transitions of CH_3OH. The values were computed through Gaussian fitting (see Table 3.3), and the average for each clump is listed in Table 3.5.

To calculate the dust mass $M_{\rm dust}$ we used the ATLASGAL data at 870 μm. For this purpose we used the expression (Hildebrand 1983),

$$M_{dust} = \frac{D^2 F_\nu R_{gd}}{\kappa_\nu B_\nu(T)} \quad ,$$

where F_ν is the flux density at frequency ν. This expression assumes that the dust emission is optically thin. Assuming a dust temperature T=20 K and using a value of $\kappa_{870\mu m} = 1.85$ cm^2 g^{-1}, interpolated from the tabulated values from the Ossenkopf and Henning (1994) MRN distribution model with thin ice mantles that have coagulated at 10^6 cm^{-3}, and a gas-to-dust ratio R_{gd} of 100. The results are listed in Table 3.5.

The computed virial masses and virial parameters are shown in Table 3.5. For all the clumps the value of the virial mass is similar or higher than the dust mass. The virial parameter is in all cases $\sim$1, suggesting that the clumps are gravitationally bound.

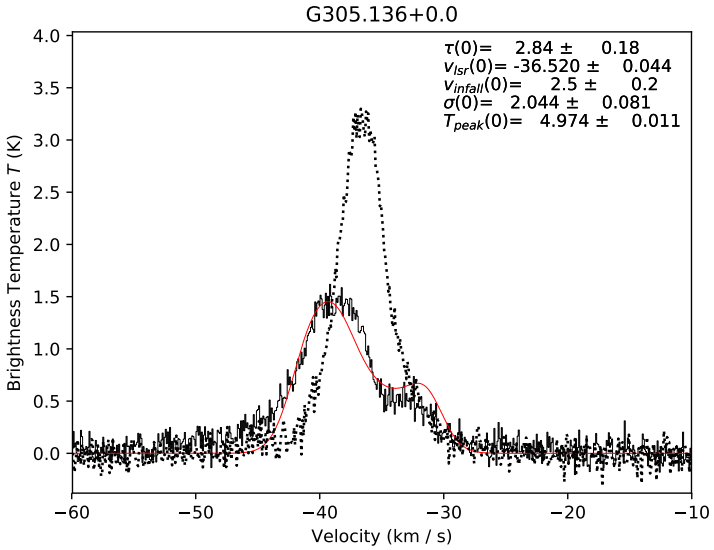

Figure 3.11: HCN(3-2) (solid line) and HNC(3-2) (dotted line) peak position spectra toward G305.136+0.068. The red line shows the best result of the fitting of the HILL5 model.

3.2.2 Evolutionary stages

The four observed clumps were identified by having a large flux density at millimetre wavelengths and by being undetected at mid and far-infrared wavelengths, implying that they are massive and cold. The IR Spitzer-IRAC data (Figure 2.1) suggest that the clumps are in different stages of star formation. G18.606-0.076 is associated with a dark IR region. G305.136+0.068 and G333.125-0.562 show 5.8 μm point sources suggesting they harbour accreting regions. Finally towards G34.458+0.25 we see the presence of a green fuzzy at the center of the clump, suggesting a later stage of evolution with a protostar forming in the center of the clump.

3.2.3 Collapse

In order to quantify the infall dynamics we used a radiative transfer model called HILL5 (De Vries and Myers 2005) using PySpecKit (Ginsburg and Mirocha 2011). The model assumes that the excitation temperature increases inward as a linear function of optical depth and uses 5 free parameters that are the line center optical depth of the cloud τ_c, the line-of-sight velocity of the system v_{lsr}, the infall velocity of the cloud v_c, the velocity dispersion σ and the peak excitation temperature in the cloud T_{pk}. This model has been found to perform especially well when there are two distinct peaks (De Vries and Myers 2005), whicht is the case for G305.136+0.068 and G333.125-0.562.

Figure 3.11 shows the result of the HILL5 model fitting for G305.136+0.068. In this case we used the HCN(3-2) and the HNC(3-2) emission. The results of the Gaussian fitting of the HNC line, that shows a Gaussian profile, were used as initial conditions for the HILL5 model fitting using the HCN emission. We can see that the HNC peak line corresponds with

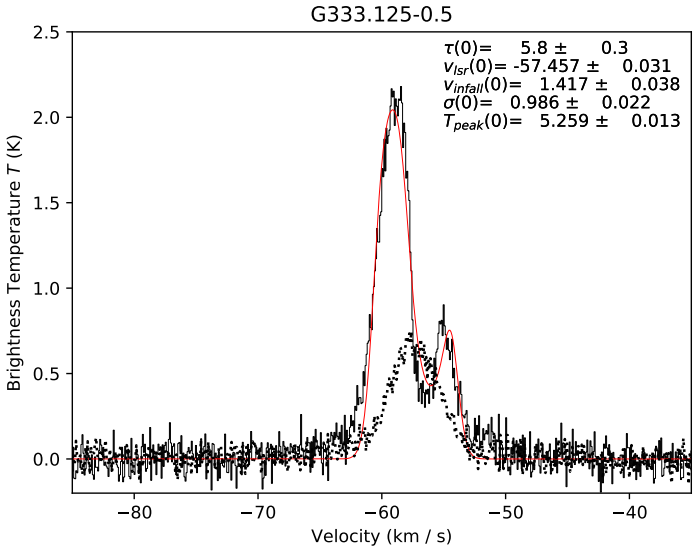

Figure 3.12: HNC(3-2) (solid line) and CH_3OH(5-4) (dotted line) peak position spectra toward G333.125-0.562. The red line shows the best result of the fitting of the HILL5 model.

the self-absorption dip from the HCN line.

Figure 3.12 shows the result of the HILL5 model fitting for G333.125-0.562. The line used for the initial conditions in this case is CH_3OH(5-4) for which the peak position corresponds to the self-absorption dip from the HNC line. The HCN line was not used for the HILL5 model fitting due to the presence of prominent velocity wings. The results of the models are shown in Table 3.6. The infall velocity for G305.136+0.068 is 2.5 km/s and for G333.125-0.562 is 1.4 km/s.

Table 3.6: Results of the HILL5 model fitting for G305.136+0.068 and G333.125-0.562.

Source	τ	v_{lsr} (km/s)	v_{infall} (km/s)	σ (km/s)	T_{peak} (K)
G305.136+0.068	2.84	-36.52	2.5	2.04	4.97
G333.125-0.562	5.8	-57.46	1.4	0.99	5.26

3.2.4 Radial velocity dispersion profiles

The density and velocity dispersion radial profiles are important indicators to characterize the evolutionary stage of star forming clumps. For instance the standard theory of low-mass star formation from a singular isothermal sphere (Shu 1977) predicts a velocity profile for the inner envelope of $\sim r^{-1/2}$. The logatropic equation of state model from McLaughlin and Pudritz (1997) predicts velocity dispersion nearly constant in the center and rising with distance in the outer regions as $\sim r^{1/3}$

A handful of studies of velocity dispersion profiles have been reported in the literature.

Table 3.7: Results of power-law fitting (Δ v $\propto r^{\alpha}$) from the radial velocity dispersion profiles from Figure 3.13. The values in column 6 are the average from the columns 2,3,4 and 5.

	α_{HCO^+} (2)	α_{HNC} (3)	$\alpha_{N_2H^+}$ (4)	$\bar{\alpha}$ (5)
G305.136+0.068	-0.33±0.05	-0.59±0.38	-0.98±0.28	-0.63±0.16
G18.606-0.076	—	-0.35±0.03	-0.67±0.13	-0.51±0.07
G34.458+0.121	-0.52±0.13	-1.74±0.58	-1.37±0.39	-1.21±0.24

For low-mass clumps, Goodman et al. (1998) found a nearly constant velocity dispersion within their inner regions (power-law index of ∼0-0.1 at scales of ∼0.1 pc) and a rise of velocity dispersion in the outer regions with power-law index ∼ 0.2, which is close to the logatropic model. Studies of high-mass clumps show either constant or increasing inward velocity dispersions (Lapinov et al. 1998; Fontani et al. 2002, Pirogov et al. 2003), which, apart from optical depth effects, could imply a higher degree of gas dynamical activity in central regions. Caselli and Myers (1995) derived an opposite trend from comparison of line widths and sizes of the emission regions for different species in Orion clumps.

Figure 3.13 shows the observed radial velocity dispersion profiles for G305.136+0.068, G18.606-0.076 and G34.458+0.121 in the molecules that show Gaussian-like profiles and are spatially extended. We find that for all the clumps and molecules the widths tend to increase inwards. Each point is taken as an average of the values inside a ring of a certain radius. The velocity dispersion values are taken from the second moment, the intensity weighted velocity dispersion. The error bars represent weights for the fitting and are calculated taking into account the dispersion of the values and the number of points for each average calculation. The average power-law index found for G305.136+0.068 is -0.63±0.16, for G18.606-0.076 is is -0.51±0.07, and for G34.458+0.121 is -1.21±0.24. Detailed results are shown in Table 3.7.

The discrepancy between the low-mass and high-mass clumps could be due to a higher degree of dynamical activity of gas in central regions of HMSF clumps, including differential rotation, infall motions and turbulence due to winds and outflows from massive protostars. Because of this we would expect to see different velocity dispersion profiles for different objects depending from their evolutionary stage.

To be able to study if there is any relation between the behaviour of the radial velocity dispersion profile and the evolutionary stage of the clumps a comparison with a bigger sample of objects was done. We used a sample of 15 SuperMALT sources classified as quiescent, protostellar or HII region. Figure 3.14 shows the radial velocity dispersion profiles for each clump grouped in their respective evolutionary stage, including our four clumps. For this purpose we used the HCO^+(3-2) line. All the clumps have widths that increase inwards but with different trends. The average results of the power-law index for each group is -0.1±0.02 for the quiescent clumps, -0.2±0.01 for the protostellar and -0.3±0.02 for the H II regions. This suggests a trend of decreasing index for earlier evolutionary stages. This may support the hypothesis mentioned before because in earlier evolutionary stages the clumps are more dynamically quiet.

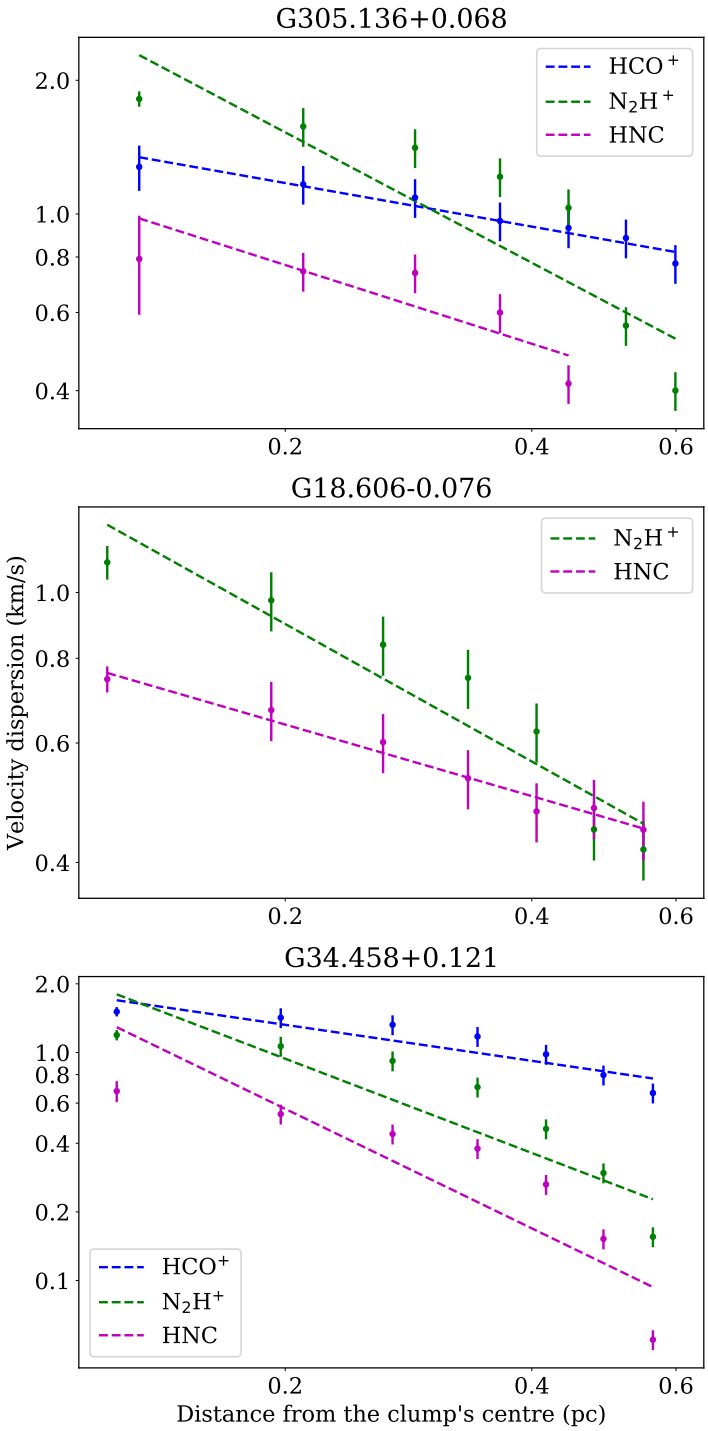

Figure 3.13: Radial velocity dispersion profiles from G305.136+0.068, G333.125-0.562, G18.606-0.076 and G34.458+0.121 using the HCO^+ (blue), HNC (magenta) and N_2H^+ (green) data. The dashed lines are linear fittings to the points. The results are listed in Table 3.7.

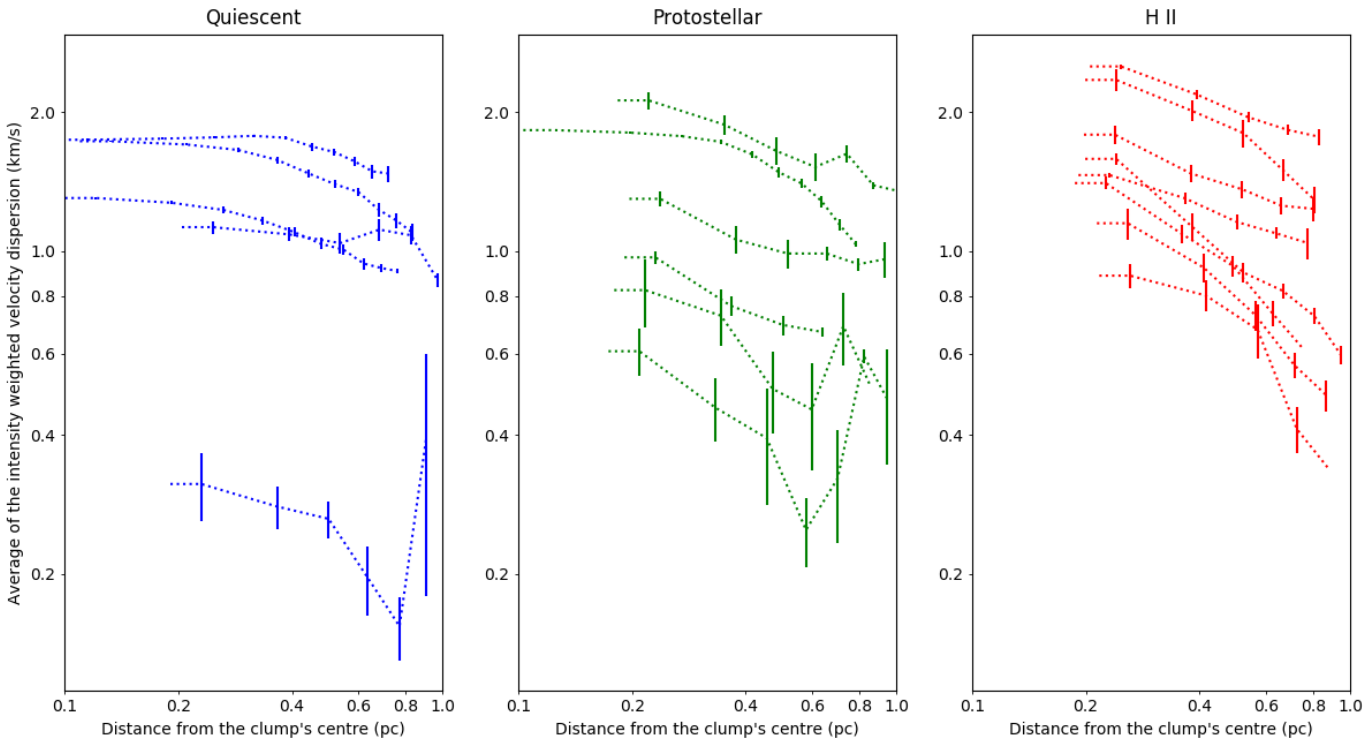

Figure 3.14: Radial velocity dispersion profiles for the 15 sources from the SuperMALT and G305.136+0.068, G333.125-0.562, G18.606-0.076 and G34.458+0.121, grouped following their evolutionary classification: quiescent (left panel), protostellar (center panel) and H II region (right panel).

Chapter 4

G305: Small scale (∼0.02 pc) structure with ALMA

In this chapter we will analise observations of molecular line emission and continuum emission at 3mm toward G305.137+0.069, a MDCC identified by Garay et al. (2004) from mm observations. This object was selected as a candidate for a clump in early stage of evolution due to its lack of MSX and IRAS emission, and classified as an Infrared Dark Cloud (IRDC) by Peretto and Fuller (2009) for its lack of bright infrarred emission in the *Spitzer* GLIMPSE and MIPSGAL archive data. The clump is located on the edge of the star-forming complex G305, one of the most luminous HII region complex in the galaxy (Hindson et al. 2012), at the distance of 3.4 kpc. It has a mass of 1.1×10^3 $M_\odot$, a size of 0.3 pc and a dust temperature of $\sim$ 17 K (Garay et al. 2004). The mass and size of this MDCC are consistent with a precursor of a high-mass star clump, as shown by Kauffmann and Pillai (2010) with their empirical relationship. The value of the dust temperature, together with the detection of emission at 70 microns, indicates that this MDCC is in the pre-stellar (or quiescent) phase of evolution (see Contreras et al. 2017), and therefore is an ideal candidate to study the physical conditions in the early stages of the formation of massive stars.

4.1 Results

4.1.1 Continuum emission

Figure 4.1, left panel, shows our image of the 3 mm dust continuum emission observed with ALMA. Also for comparison shown, in the right panel, is the 4.5 μm infrared emission image from the Spitzer Space Telescope ($\sim$ 2 angular resolution) which exhibits a clear extinction feature toward the center. Both panels are overlaid with contours of the single dish dust continuum emission at 0.87 mm (ATLASGAL, $\sim$ 19 angular resolution, Schuller et al. 2009).

The bulk of the dust continuum emission revealed by ALMA is concentrated toward the center of the clump – as determined from the single dish observations – and lies near the

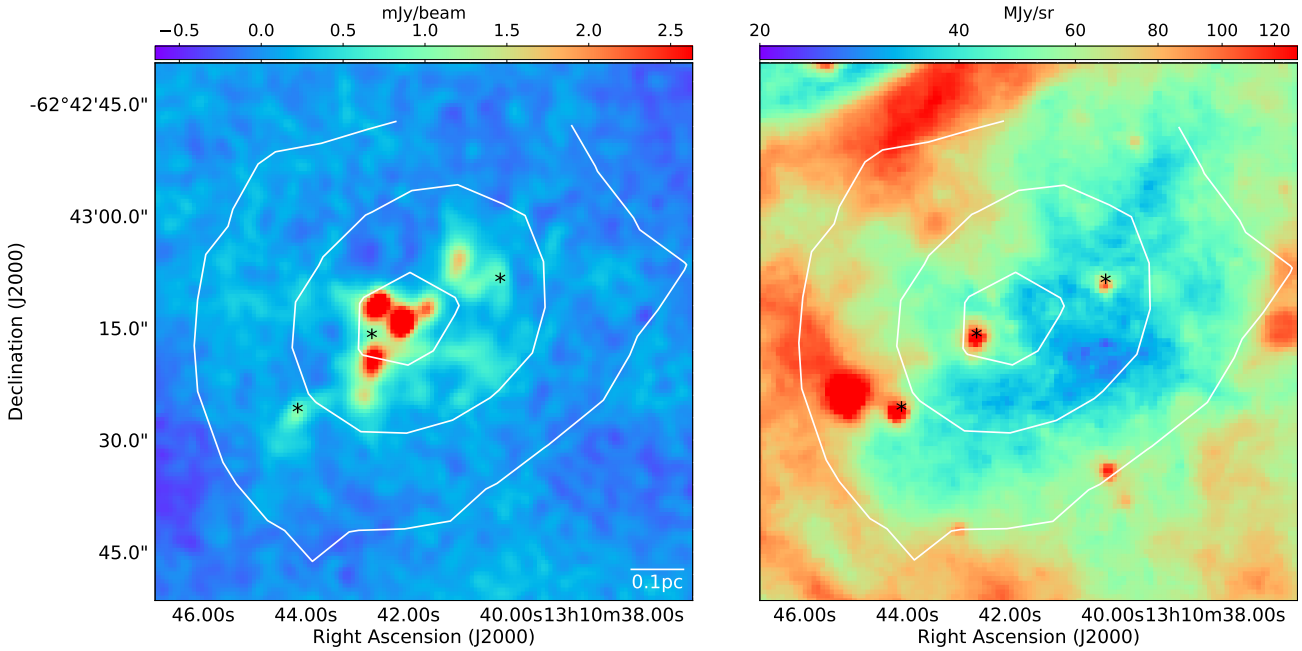

Figure 4.1: Images of the millimetre and infrared emission toward G305.137+0.069 at ∼2" angular resolution. Left panel: 3 mm image from ALMA. Right panel: 4.5 μm image from *Spitzer Space Telescope*. In both images the white contour levels correspond to single dish dust continuum emission (ATLASGAL 870 μm, ∼19" angular resolution, levels are drawn at 20, 50 and 90% of the peak emission). The stars show the position of three Spitzer sources reported by Garay et al. (2015). The scale bar marks a size of 0.1 pc on the bottom right corner of the left panel.

peak of the mid-IR extinction. The most prominent features that can be identified from a visual inspection of the ALMA image are a handful of bright compact structures as well as weaker emission distributed in filamentary-like structures. In order to be quantitative in the identification of features in the 3mm image we used two commonly employed algorithms: Dendrogram (Rosolowsky et al. 2008) and Gaussclump (Stutzki and Guesten 1990). The number of compact structures (hereafter referred as cores) extracted by Gaussclump is twelve (shown by the orange ellipses in Figure 4.2) while Dendrogram extracted nine cores. Eight cores were extracted by both methods; their parameters (flux densities and sizes) being similar (differences not larger than 10%). The most notable difference between the output of the two algorithms is in core mm-6 which was not extracted by Dendrogram. Given the good agreement, hereafter we will adopt the core parameters determined from Gaussclump, Table 4.1. Col.1 gives the core name, col. 2 the peak position , cols. 3-5 give, respectively, the peak flux density, flux density and angular size.

The total flux density measured, within a region of ∼ 100 in size, in the ALMA continuum image is 85 mJy. A Gaussian fit to the intensity distribution observed with the compact array (ACA) only gives an angular size of 19.1 × 12.8. An extrapolation of the flux densities measured with single dish, of 16.1 Jy at 0.87 mm (Garay et al. 2015) and 4.24 Jy at 1.2 mm (Garay et al. 2004), assuming a dust emissivity index, β, of 2, predicts a value at 3 mm of ∼ 110 mJy. The lower observed value is probably due to the more extended emission observed with single dish being resolved out by the interferometric observations. This is supported by

the fact that the size determined by the single dish observations is ~ 33 (Garay et al. 2004), smaller than that determined with the ACA .

Assuming that the dust continuum emission is optically thin, it is possible to compute the beam averaged column density in each position of the image from the expression,

$$N(H_2) = \frac{F_\nu^{beam} R_{\rm gd}}{\Omega_b \kappa_\nu \mu_{H_2} m_H B_\nu(T)},$$

where F_ν^{beam} is the observed flux per beam at frequency ν, $B_\nu(T)$ is the Planck function at dust temperature T, Ω_b is the beam size, μ_{H_2} is the mean molecular weight, and κ_ν is the dust opacity. Using a value of $\kappa_{3mm} = 0.21$ cm^2 g^{-1}, interpolated from the tabulated values from the Ossenkopf and Henning (1994) MRN distribution model with thin ice mantles that have coagulated at 10^6 cm^{-3}, a value of $\mu_{H_2} = 2.8$ (Kauffmann et al. 2008) and a gas-to-dust ratio R_{gd} of 100, the above expression at 3 mm reads as

$$N(H_2) = 5.13 \times 10^{23} \left(e^{(4.8/T)} - 1 \right) F_{100GHz}^{beam} \ \ {\rm cm}^{-2},$$

where F_{100GHz}^{beam} is the 100 GHz flux density observed in a beam of 2.39×2.10, measured in mJy.

Assuming a temperature of 20 K for the whole cloud, (average of the values reported by Garay et al. 2015 and Guzmán et al. 2015), we find that the column densities across G305.137+0.069 have a mean value of 4.3×10^{23} cm^{-2} and a maximum value of 8.1×10^{23} cm^{-2}. In section 4.2.1 we discuss the distribution of the column density across the clump.

4.1.2 Molecular line emission

Figure 4.3 shows images of the velocity integrated emission obtained with ALMA in the CS, HCO^+ and N_2H^+ lines, along with the dust continuum image. The velocity range of integration is from -46.8 to -26.8 km/s for the CS and HCO^+ lines and from -50.0 to -43.2 km/s for the N_2H^+ line (corresponding to the lower velocity component of the hyperfine structure; see discussion below). Figure 4.3 shows that the molecular emission arises from a bright central region, with an angular size of ~ 12, and an extended, weaker envelope, best seen in the HCO^+ line. The overall extent and morphology of the HCO^+ and CS emission are similar, although there are some differences at fine levels of detail, such as in the position of the peak line emission (shown as a black cross). We note that the weak emission in HCO^+ is more uniformly distributed and extended than the weak continuum emission. This is most likely due to the HCO^+ line emission probing lower H_2 column densities than those probed by the dust emission. Of the three tracers, N_2H^+ is the one that best correlates with the dust continuum emission.

The main characteristics of the observed profiles are illustrated in Figure 4.4 which shows the peak spectra observed toward the three brighter dust sources: mm-8, mm-9 and mm-10. The profiles of the HCO^+ emission are highly complex, showing multiple velocity components

Table 4.1: Observed parameters of the dust continuum cores1.

Core	Peak position		Peak Flux Density[2]	Total flux[2]	θ_s
	α(J2000)	δ(J2000)	(mJy beam^{-1})	(mJy)	(arcsec)
(1)	(2)		(3)	(4)	(5)
mm-1	13:10:40.28	-62:43:07.34	0.86±0.043	1.69±0.084	1.99±0.15
mm-2	13:10:40.41	-62:43:20.70	0.63±0.032	0.68±0.034	1.73±0.13
mm-3	13:10:40.71	-62:43:09.44	1.02±0.051	1.11±0.055	1.62±0.12
mm-4	13:10:40.89	-62:43:17.92	0.77±0.039	3.07±0.15	3.08±0.22
mm-5	13:10:40.98	-62:43:05.85	1.75±0.088	4.64±0.23	2.66±0.20
mm-6	13:10:41.58	-62:43:12.07	2.25±0.11	2.41±0.12	1.40±0.10
mm-7	13:10:42.04	-62:43:17.90	1.40±0.070	1.20±0.060	1.04±0.076
mm-8	13:10:42.09	-62:43:13.95	5.82±0.29	10.47±0.52	2.37±0.17
mm-9	13:10:42.58	-62:43:11.76	4.36±0.22	7.51±0.38	2.29±0.16
mm-10	13:10:42.64	-62:43:19.08	3.20±0.16	9.67±0.48	3.07±0.22
mm-11	13:10:42.83	-62:43:23.98	1.57±0.079	2.47±0.12	1.80±0.13
mm-12	13:10:44.14	-62:43:26.34	1.06±0.053	1.46±0.073	1.56±0.11

[1] Cores identified using GaussClump with parameters *threshold = 3.5σ, step = 1σ and size = 1 beam.*

[2] We estimate uncertainties in the flux of 5%.

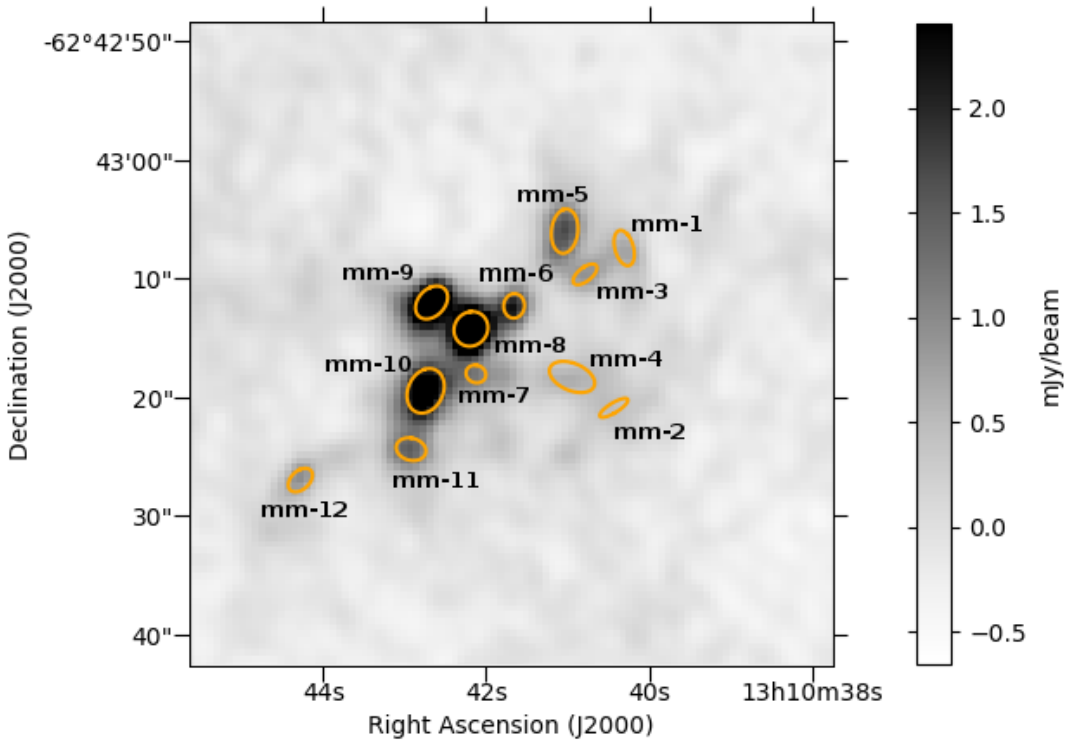

Figure 4.2: ALMA 3mm dust continuum compact structures (shown as orange ellipses) extracted using the GaussClump algorithm (12 cores).The parameters used in the search are *threshold* = 3.5σ, *step* = 1σ and *size* = 1 beam.

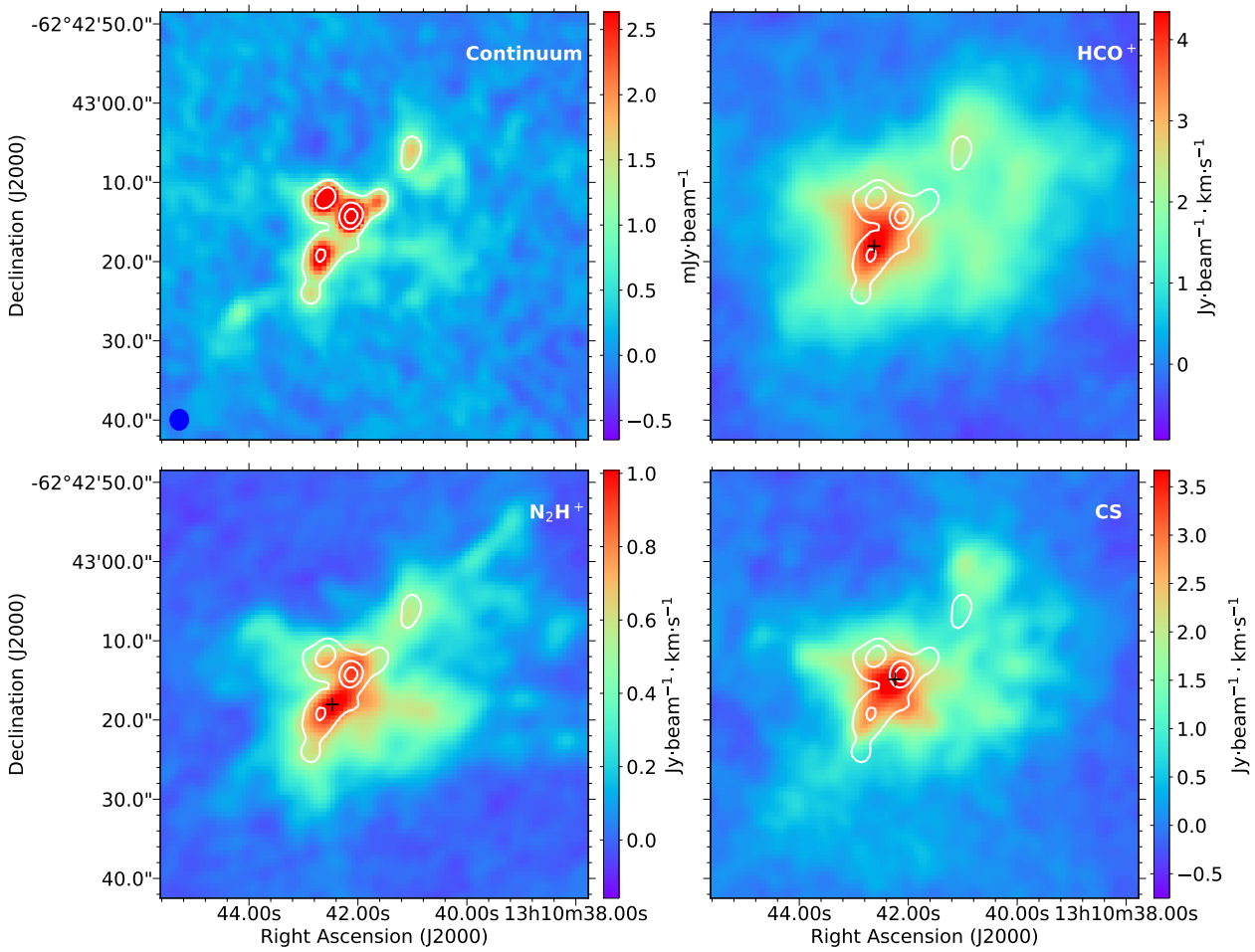

Figure 4.3: Images of the dust continuum emission and velocity integrated line emission from G305.136+0.068. Upper left: 3mm continuum. Upper right: HCO^+. Lower left: N_2H^+. Lower right: CS. In each panel overlaid in white contours is the 3 mm dust continuum emission at 20%, 50% and 80% of the peak. The color scale is in units of mJy beam^{-1} in the continuum image and in mJy beam^{-1} km s^{-1} for the line images. The peak of each line emission is shown by the black crosses. The angular resolution is shown in the lower left corner of the continuum emission image.

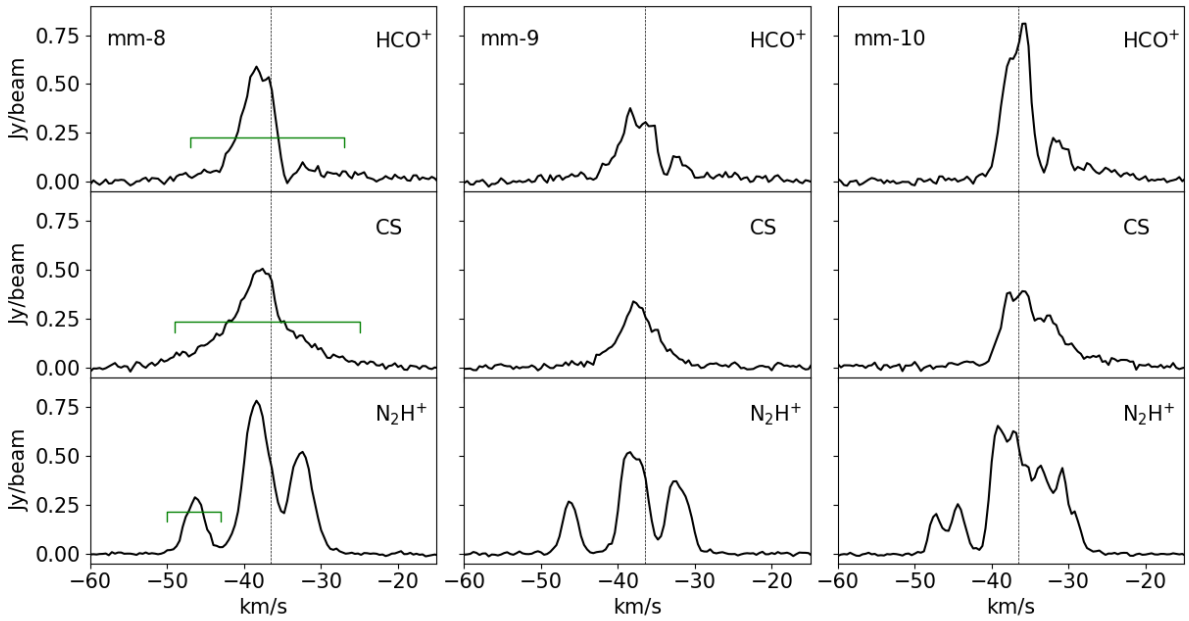

Figure 4.4: Spectra of the line emission observed at the peak position of the three brighter mm sources (see Table 4.1 for more details). From left to right: mm-8, mm-9 and mm-10. From top to bottom: HCO^+, CS and N_2H^+. The dashed vertical line shows the clump velocity of -36.5 km/s (Garay et al. 2015). The brackets show the velocity intervals used for the integration of the moment maps.

and high velocity wings. The multiple velocity components are seen across the whole clump, and we suggest that they mark the presence of gas flows driven by gravity (see discussion below). High velocity wings are best seen in the profiles of the CS emission. The profiles of the N_2H^+ line are less complex, with the emission arising from typically a single velocity component. We note that the N_2H^+(1-0) transition consists of 15 main hyperfine components, however, due to the overlap of closely spaced HF components, only 3 distinct lines are observed, as shown in Figure 4.4 (bottom left panel). Towards a few positions within the clump the spectra of the N_2H^+ emission shows double peaks in each of the three sets of blended hyperfine components, indicating the presence of two velocity components in those line of sights (e.g., towards mm-10). We suggest that these positions mark regions where flows driven by gravity are merging, giving rise to cores.

Figure 4.5 presents a grid of the HCO^+ spectra observed toward the 30×30 central region of G305.137+0.069, showing the complexity of the line shapes. Clearly seen are features such as high-velocity wings, skewness and multiple peaks. This diversity of features have been predicted to be observed in models of compressible turbulence, which also show that the appearance of non-Gaussian line-shape features decreases as time evolves (e.g. Falgarone et al. 1994). The line profiles observed toward G305.137+0.069 show similarities to the model spectra at early stages of evolution.

To characterize the emission at each point within the region we performed moment analysis

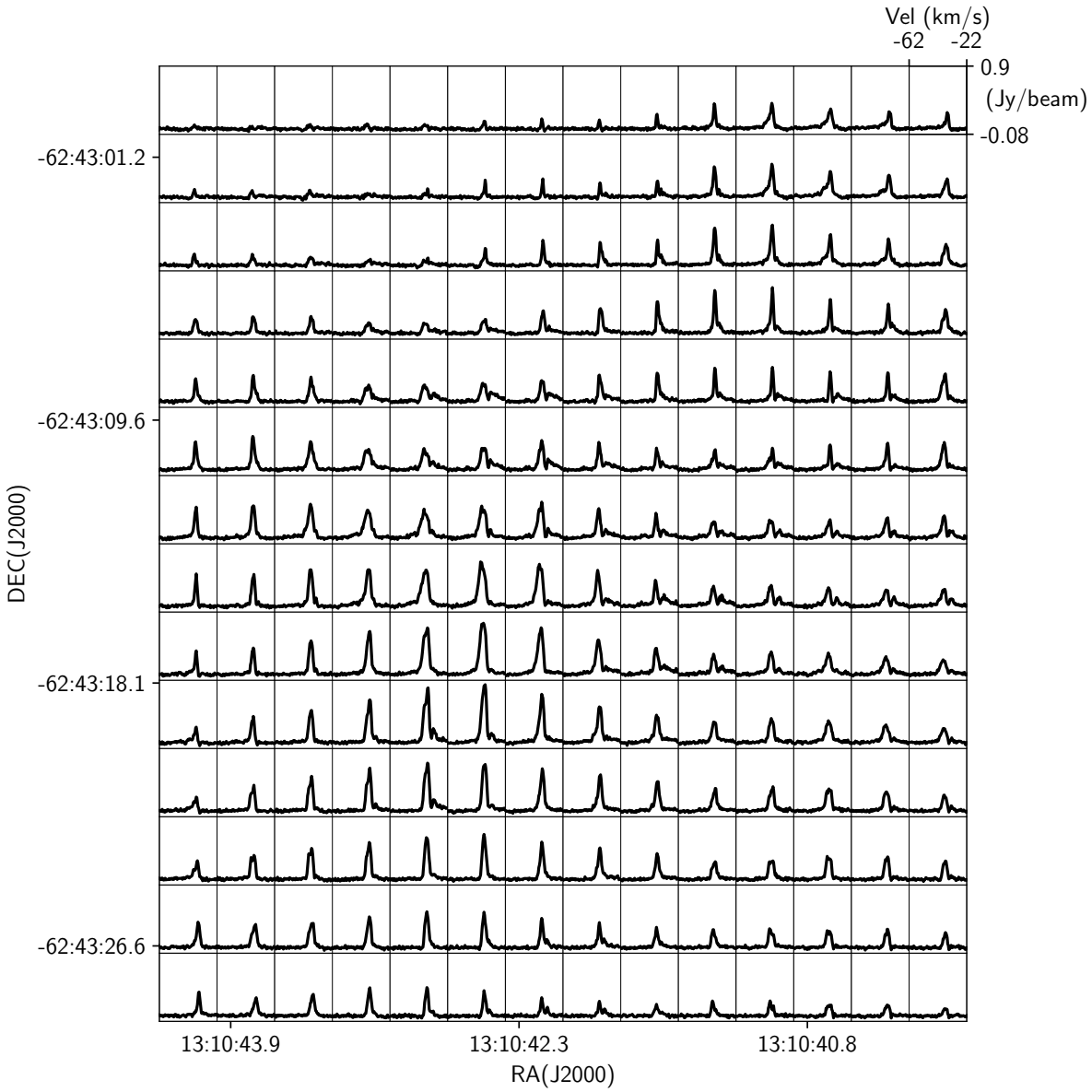

Figure 4.5: 30"×30" spectral map of the HCO^+ emission towards the central region of G305.137+0.069. The grid spacing is 2" (roughly the beam size).

of the data (Sault et al. 1995) which allows an easy comparison of the characteristics of the emission in the different molecular transitions. We computed the zeroth moment (M_0, or integrated intensity), first moment (M_1, or intensity weighted velocity field) and second moment (M_2, or intensity weighted velocity dispersion) defined as follows,

$$M_0 = \int_{v_i}^{v_f} T_A^*(v)\mathrm{d}v, M_1 = \frac{\int_{v_i}^{v_f} T_A^*(v) v \mathrm{d}v}{\int_{v_i}^{v_f} T_A^*(v)\mathrm{d}v}, M_2 = \sqrt{\frac{\int_{v_i}^{v_f} T_A^*(v)(v-M_1)^2\mathrm{d}v}{\int_{v_i}^{v_f} T_A^*(v)\mathrm{d}v}},$$

where $T_A^*(v)$ is the measured brightness at velocity v, and v_i and v_f are the limits of the velocity range. The velocity range used in the moment calculations of HCO^+ and CS is from -46.8 to -26.8 km/s (these ranges are marked in Figure 4.4). The moments of the N_2H^+ emission were computed using the lower velocity component of the three observed lines (velocity range from -50.0 to -43.2 km/s) which is composed of a single hyperfine component.

In the moment analysis only those positions across the clump where the emission has a signal-to-noise > 3 were included. We used a threshold of 0.06 Jy beam^{-1} ($\sim 3\sigma$) for all three transitions. At clump locations where the spectra shows multiple velocity components or self-absorption this analysis may not describe well the gas kinematics, but it does provide a method to easily characterize and compare the emission from the tracers and the dust continuum across the clump.

Figure 4.6 shows the M_0, M_1, and M_2 moments of the HCO^+, CS and N_2H^+ emission toward G305.137+0.069. Overlaid on the M_1 and M_2 images are contours of the integrated intensity to highlight the relation between the intensity of the emission of the gas and its kinematics. The intensity weighted velocity field images show that none of the molecular lines present organized motions or any clear velocity gradients across the clump. There is however a good agreement in the velocity field determined from the emission in the HCO^+ and CS lines. In the N_2H^+ moment images clearly seen is an elongated structure, extending from southeast to northwest, aligned with the dust continuum cores that is not present in the other two molecules.

Figure 4.7 presents position-velocity (PV) diagrams of the HCO^+, N_2H^+ and CS emission along cuts in two perpendicular directions, shown in the top panels of the figure, passing through the main cores. The N_2H^+ cuts show three velocity features corresponding to the three group of hyperfine components, which, as expected, exhibit the same pattern. A striking feature seen in the CS PV diagram along the SE-NW cut, also seen in HCO^+, is the presence of three high velocity structures (two redshifted and one blueshifted) near the central region of the clump. While the typical interpretation is that the wing emission is due to the presence of bipolar outflows arising from protostellar objects within the cores, the odd number of lobes complicates the identification of the driving sources. An alternative explanation is that the high velocity features are the result of gravitational acceleration as the density concentrations collapse.

To investigate in more detail the spatial distribution of the wing emission, we made contour maps of the velocity integrated CS emission in two ranges of blueshifted and redshifted radial flow velocities: intermediate (IV) and high (HV). The radial flow velocity, v_{flow}, is defined as $v_{LSR} - v_0$, where v_0 is the systemic velocity of the clump. The clump velocity is assumed

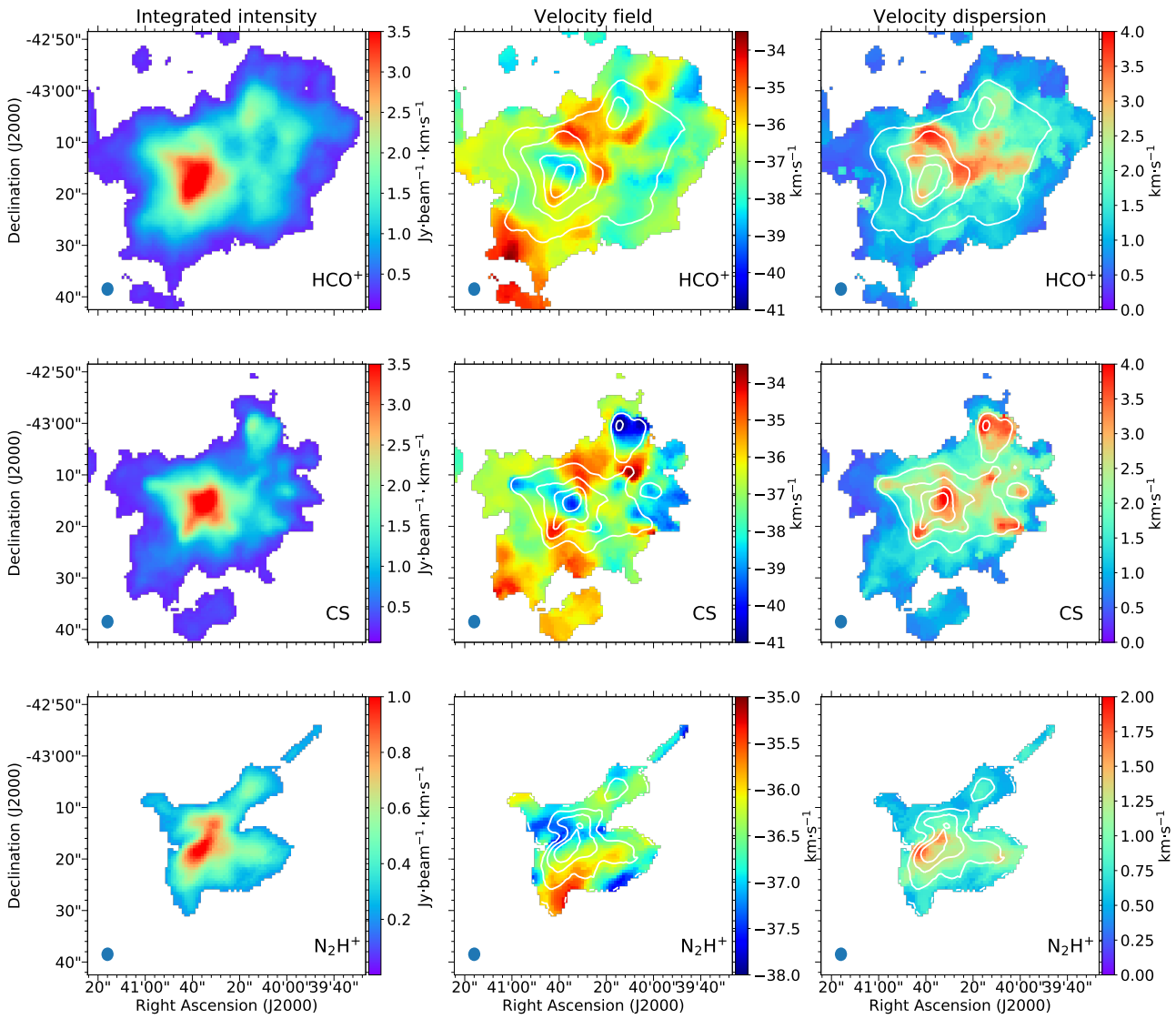

Figure 4.6: Moment maps of the HCO^+, CS and N_2H^+ emission (from top to bottom). From left to right: integrated intensity (zeroth moment, units of Jy beam^{-1} km s^{-1}), intensity weighted velocity field (first moment, units of km s^{-1}), intensity weighted velocity dispersion (second moment, units of km s^{-1}). Overlaid in white are contour levels of the integrated intensity (20, 40, 60 and 80% of the peak). The beam is shown in the lower left corner.

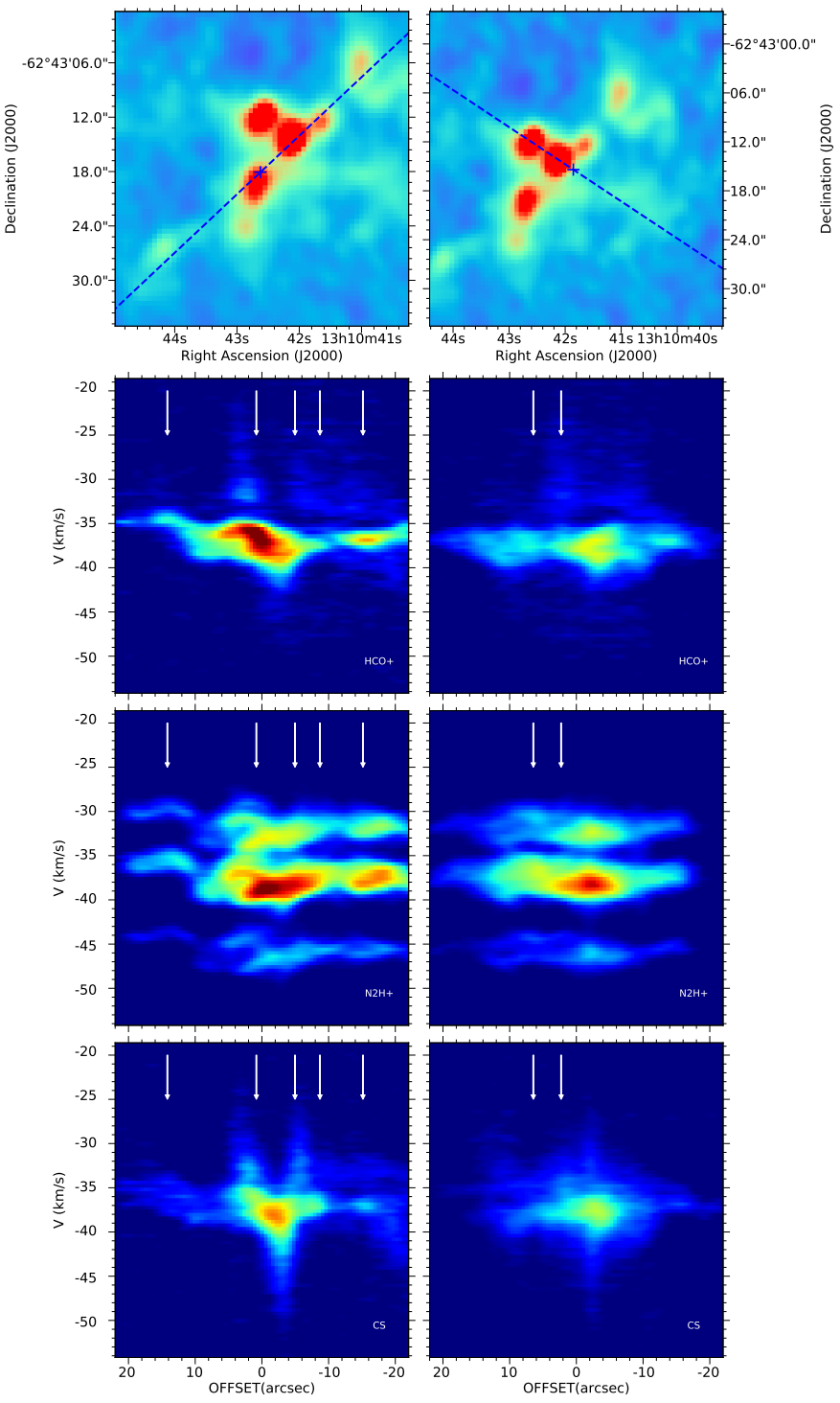

Figure 4.7: Position velocity diagrams of HCO^+, N_2H+ and CS. The cuts were made along two perpendicular directions shown in the upper panels. The south-east to north-west cut is shown on the left column, and the north-east to south-west cut in the right column. The positions of the mm-sources crossed by the cuts are shown with arrows. The center of the cuts, from which the offset is measured, are shown by blue crosses on the top panels.

to be -36.5 km/s (Garay et al. 2015). Figure 4.8 shows maps of the IV and HV CS emission overlaid on the ALMA dust continuum image. The range of flow velocity integration for the IV map (upper panel) is from -5 to -9 km s^{-1} for the blueshifted gas and from 5 to 9 km s^{-1} for the redshifted gas (red contours) and for the HV map (bottom panel) is from -9 to -14 km s^{-1} for the blueshifted gas and from 9 to 14 km s^{-1} for the redshifted gas. The morphology of the CS wing emission is quite complex, showing an intricate overlap between the blueshifted and redshifted emission. The question arises as to which the energy source of the flowing motions. A possible explanation is that the observed morphology is due to the presence of a handful of outflows driven by low-mass protostars. We note however that the highest blueshifted and redshifted flow velocities detected in the region arises from two compact structures located, respectively, to the southeast and northwest from core mm-8, which are possible tracing a bipolar outflow and hence indicating that core mm-8 host an energy source. An alternative explanation is that the observed motions are the result of the global gravitational collapse of the clump. This scenario proposes that a cloud collapsing on a large scale gives rise, through the focusing effects of gravity, to the formation of a cluster of cores (Hartmann and Burkert 2007, Naranjo-Romero et al. 2015, Kuznetsova et al. 2018). The mass needed to explain the magnitude of the IV flow velocities, of ~ 7 km s^{-1} over the spatial extent of the IV region, of ~ 0.2 pc in radius, is $\sim 1 \times 10^3$ M$_\odot$. This is similar to the mass of the whole clump, giving support to the suggestion that the observed motions are driven by gravity. As can be seen in the right panel of Fig. 1, the molecular clump is engulfed by a photodissociated region (PDR). We suggest that the cold clump has become unstable and collapse due to the compression exerted by the warm gas of the PDR.

Molecular emission from cores

In what follows, we discuss the characteristics of the molecular gas from the cores, which allows to investigate their kinematics and dynamical state. To determine the line center velocities and linewidths we used the observations of the N_2H^+(1-0) line, since they mainly probe the emission from dense gas. We fitted simultaneously the whole hyperfine structure of the N_2H^+(1-0) line using the N_2H^+ fitter from pyspeckit. The parameters of the 15 components used in the fit can be found in Daniel et al. (2005). Figure 4.9 shows the spectra of the N_2H^+(1-0) emission from the cores (i.e. of the emission integrated over the angular region subtended by the core) and the result of the hyperfine fit. The fitted line center velocity, linewidth and total optical depth are listed in Table 4.2.

For the cores with single line profiles, the linewidths range from 1.9 to 3.1 km/s with an average value of 2.6 km/s. These widths are much larger than the thermal widths, of 0.18 km/s at the temperature of 20 K, showing that the motions within the cores are dominated by non-thermal motions. This is in contrast to cores in low-mass clumps with tend to approach thermal broadening previous to the formation of a protostar (e.g., Pineda et al. 2010). Whether the non-thermal motions correspond to random-turbulence or core scale motions is difficult to discern. From simulations of hierarchical fragmentation in a globally collapsing cloud, Naranjo-Romero et al. (2015) concluded that the velocity dispersion at all scales are caused by infall motions. Given that this MDCC seems to be globally collapsing, then the observed large linewidths could be reflecting infalling motions within already collapsing cores.

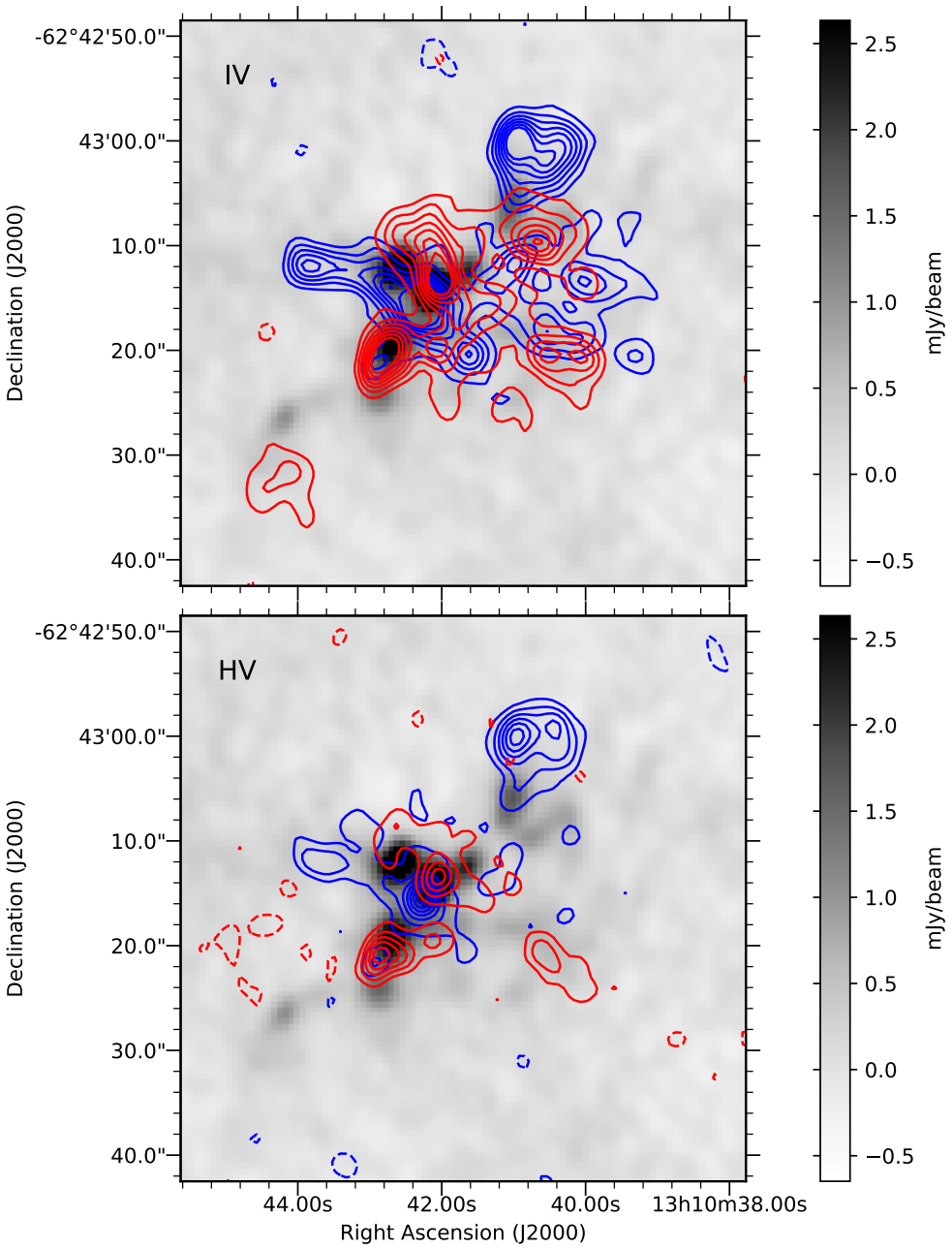

Figure 4.8: CS maps of intermediate (IV) and high velocity(HV) gas emission overlaid on the ALMA dust continuuum (gray scale). The range of flow velocity integration for the IV map (upper panel) is from -5 to -9 km s^{-1} for the blueshifted gas (blue contours) and from 5 to 9 km s^{-1} for the redshifted gas (red contours) and for the HV map (bottom panel) is from -14 to -9 km s^{-1} for the blueshifted gas and from 9 to 14 km s^{-1} for the redshifted gas.

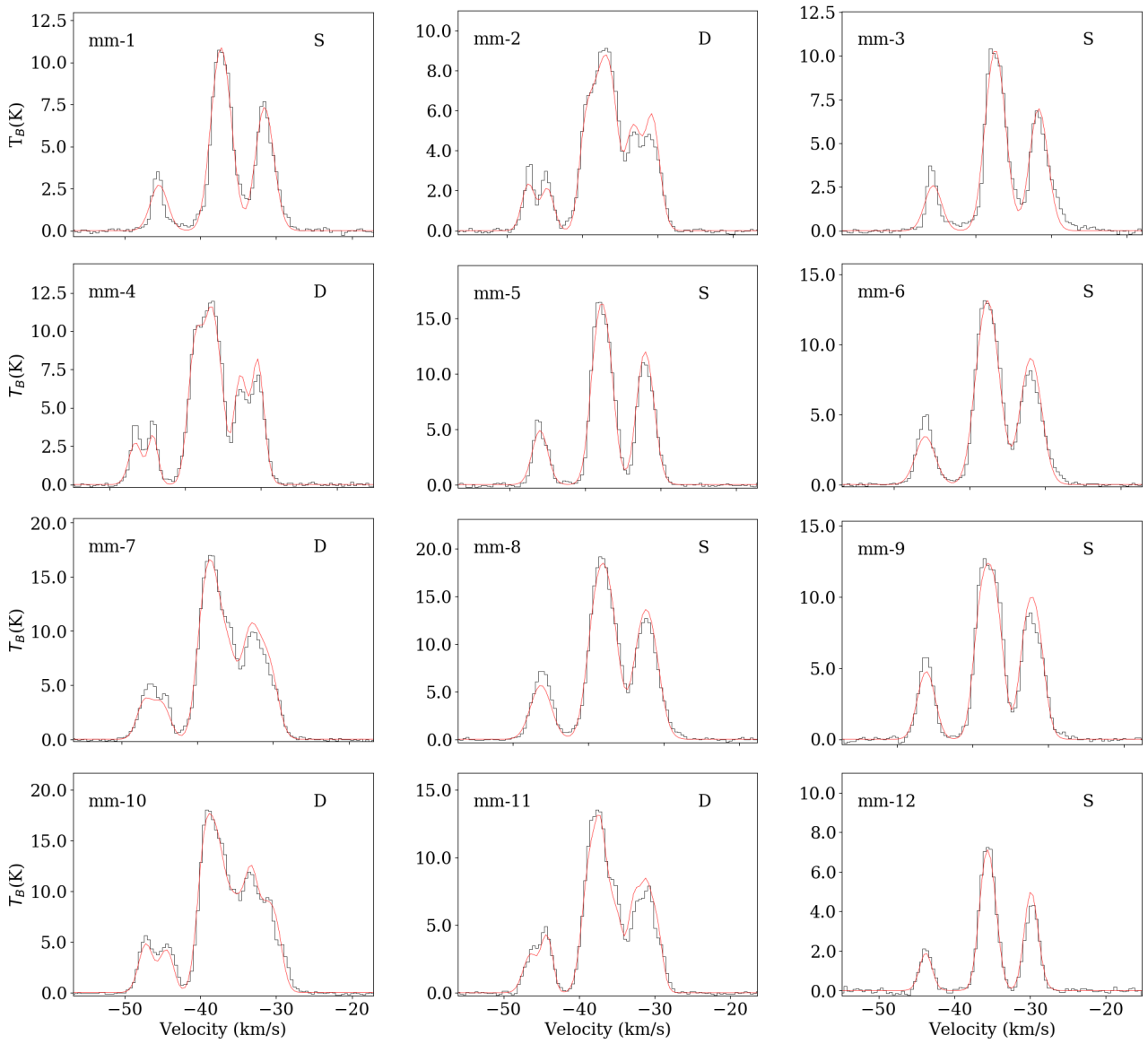

Figure 4.9: Spectra of the integrated N_2H^+(1-0) emission from the cores. The red line shows the result of an hyperfine fit using a single velocity component (labeled S) or two velocity components (labeled D). The fitted parameters are given in Table 4.2.

Table 4.2: Observed parameters of the N_2H^+(1-0) emission from cores.1

Core	Component	v (km/s)	Δv (km/s)	τ
mm-1	1	-36.24±0.02	2.64±0.04	0.54±0.01
mm-2	1	-37.91±0.08	1.94±0.16	2.43±0.57
	2	-35.40±0.07	2.01±0.13	0.42±0.02
mm-3	1	-36.38±0.03	2.60±0.06	0.51±0.01
mm-4	1	-37.36±0.05	2.01±0.12	0.55±0.01
	2	-35.03±0.04	1.52±0.10	1.02±0.46
mm-5	1	-36.76±0.02	2.36±0.05	1.45±0.25
mm-6	1	-36.61±0.02	2.98±0.06	0.92±0.25
mm-7	1	-37.85±0.10	2.21±0.12	0.39±0.05
	2	-35.58±0.19	2.55±0.27	2.57±0.60
mm-8	1	-37.04±0.02	3.09±0.05	1.88±0.23
mm-9	1	-36.88±0.02	2.56±0.06	3.33±0.35
mm-10	1	-37.96±0.06	2.20±0.10	0.98±0.03
	2	-35.25±0.09	1.99±0.15	4.05±0.74
mm-11	1	-37.18±0.07	2.30±0.13	0.57±0.02
	2	-35.01±0.06	1.54±0.12	8.55±1.73
mm-12	1	-34.56±0.01	1.92±0.04	0.38±0.01

[1] Derived from a fit to the whole hyperfine structure.

Knowing the optical depth in a single HF transition of N_2H^+, $\tau_\nu^{\rm i}$, the total column density of this molecule can be calculated from the expression (cf. Mangum and Shirley 2015),

$$N_{tot}(N_2H^+) = \frac{3h}{8\pi^3\mu^2}\frac{Q_{rot}}{J_u R_{\rm i}}\exp\left(\frac{E_u}{kT_{\rm ex}}\right)\left[\exp\left(\frac{h\nu}{kT_{\rm ex}}\right)-1\right]^{-1}\int\tau_\nu^{\rm i}{\rm d}v$$

where E_u and J_u are, respectively, the energy and rotational quantum number of the upper level of the transition, μ and Q are, respectively, the dipole moment and partition function of the molecule, $R_{\rm i}$ is the relative strength of the HF line and T_{ex} is the excitation temperature. This expression assumes that the level populations are described by a single excitation temperature (LTE). In particular for observations of the J = 1→0 transition, using μ = 3.40 Debyes and $Q_{rot} = 0.45(T_{ex} + 0.75)$, (Mangum and Shirley 2015), the above expression can be written as

$$N_{tot}(N_2H^+) = \frac{3.11\times10^{11}(T_{ex}+0.75)}{R_{\rm i}}\exp\left(\frac{E_u}{kT_{\rm ex}}\right)\left[\exp\left(\frac{h\nu}{kT_{\rm ex}}\right)-1\right]^{-1}\int\tau_\nu^{\rm i}{\rm d}v$$

The column densities of N_2H^+ toward the cores, computed using the total optical depth in the J=1-0 transition reported in Table 4.2 (hence $R_{\rm i}$=1 in the above expression) and assuming T_{ex} = 20 K, are given in col. 2 of Table 4.3. They range from 9.3×10^{13} to 1.1×10^{15} cm^{-2}, with an average value of 4.4×10^{14} cm^{-2}. Column 4 of Table 4.3 gives the [N_2H^+/H_2] abundance ratio, estimated as the ratio of the column densities in these two species. The column densities of H_2, given in col. 3, were determined from the dust continuum emission integrated over

Table 4.3: Column densities of cores with a single velocity component in the N_2H^+ J = 1-0 transition.

Core	$N(N_2H^+)$ (cm^{-2})	$N(H_2)$ (cm^{-2})	$[N_2H^+/H_2]$
mm-1	1.8×10^{14}	6.1×10^{22}	3.0×10^{-9}
mm-3	1.7×10^{14}	6.0×10^{22}	2.9×10^{-9}
mm-5	4.4×10^{14}	9.4×10^{22}	4.7×10^{-9}
mm-6	3.5×10^{14}	1.8×10^{23}	2.0×10^{-9}
mm-8	7.4×10^{14}	2.7×10^{23}	2.8×10^{-9}
mm-9	1.1×10^{15}	2.1×10^{23}	5.3×10^{-9}
mm-12	9.3×10^{13}	8.5×10^{22}	1.1×10^{-9}

the angular region subtended by the cores. We find that the average $[N_2H^+/H_2]$ abundance ratio in the cores is 3.1×10^{-9}, value similar to that reported by Sanhueza et al. (2012) for quiescent clumps.

4.2 Discussion

4.2.1 Dust column density N-PDF

Figure 4.10 shows the dust column density probability distribution function (N-PDF) for G305.137+0.069, obtained using a Gaussian kernel density estimation (KDE) to avoid dependencies on the bin choice. The error of the KDE was obtained using the bootstrap method (Efron 1982). The top panel shows the N-PDF obtained including the Gaussian noise. Its shape can be described by a combination of three distributions: (i) a Gaussian distribution, which describes the noise of the column density image; (ii) a log-normal distribution, which is a signature of turbulent gas; and (iii) a power-law distribution, which is related to self-gravitating gas. The point where the N-PDF changes from log-normal to power-law is an indicator that represents a transition between the gas dynamics being dominated by supersonic turbulence, which builds the log-normal distribution, to densities where gravity plays an increasingly important role (Burkhart et al. 2017). We performed a simultaneous Bayesian estimation of the parameters of the three distributions using a Markov chain Monte Carlo sampler (MCMC; Sharma 2017) to obtain reliable parameter errors. The piecewise function used is defined as follows,

$$f(\Sigma) = \begin{cases} A\exp(-B\ (\Sigma - C)^2) & \Sigma \leq 0 \\ A\exp(-B\ (\Sigma - C)^2) + \frac{E}{\Sigma\sigma_{ln}\sqrt{2\pi}}\exp\left(\frac{-(ln\Sigma - F)^2}{2\sigma_{ln}^2}\right) & \Sigma > 0 \quad \& \quad \Sigma \leq \Sigma_t \\ A\exp(-B\ (\Sigma - C)^2) + G\ \Sigma^{\alpha} & \Sigma \geq \Sigma_t, \end{cases}$$

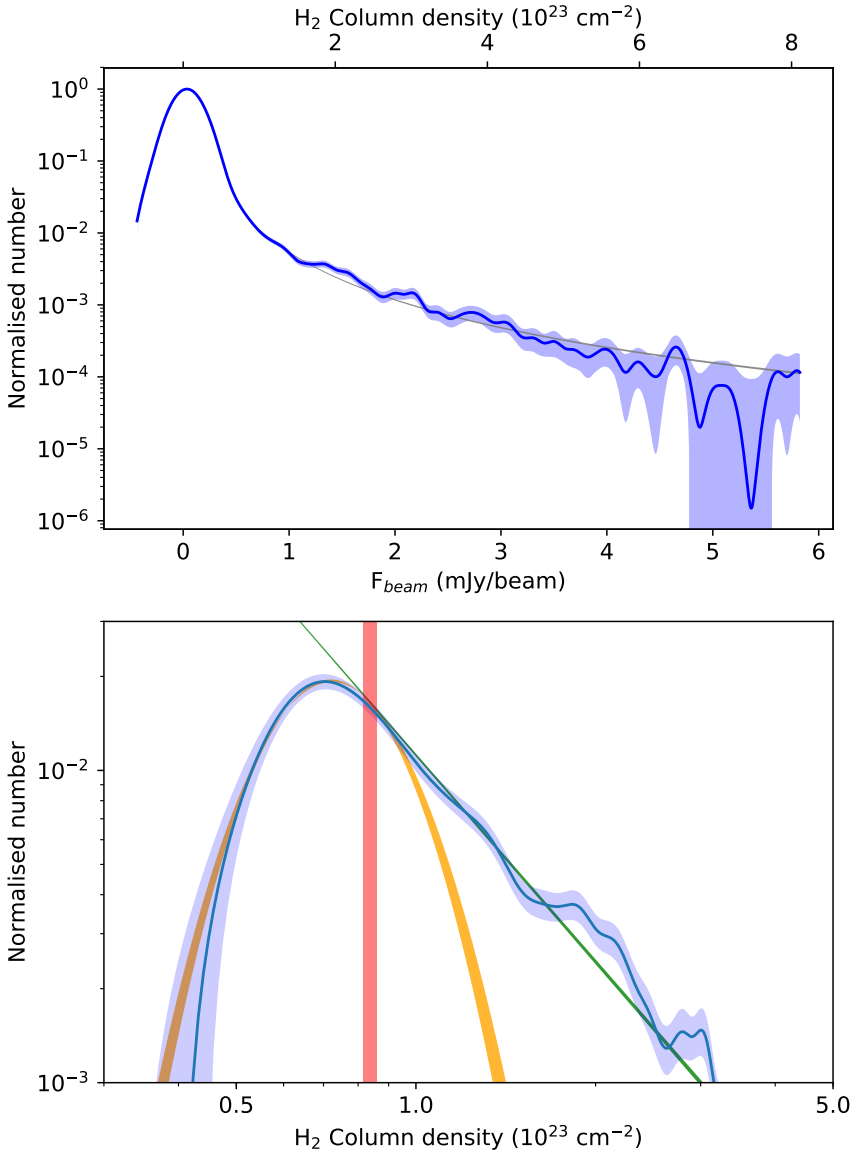

Figure 4.10: Column density PDF Gaussian kernel density estimation for G305.136+0.068 (blue line). Blue shaded regions show the uncertainties obtained through the bootstrap method (Efron 1982). The top panel shows the observed (blue line and shaded region) and inferred (gray line and shaded region) PDFs. The inferred PDF is a combination of three distributions: a Gaussian for the noise, a log-normal for the turbulent gas, and a power-law for the self-gravitating gas. The bottom panel shows the PDF with the noise subtracted, and the inferred contributions of the log-normal (orange) and power-law (green) distributions. The vertical red line shows the point at which the distributions deviate from log-normal, $N(H_2)=(8.4 \pm 0.23)\times10^{22}$ cm^{-2}. The thickness of the lines represents 1σ errors. The 1σ noise level is equivalent to $N(H_2)=1.4\times10^{22}$ cm^{-2}.

where Σ is the column density, σ_{ln} is the width of the log-normal distribution, α is the slope of the power-law, and Σ_t is the transition point between the log-normal and power-law distributions.

The bottom panel of Figure 4.10 shows the N-PDF with the Gaussian noise subtracted, leaving only the contributions from the turbulent and self-gravitating gas components. The high density end of the N-PDF is well described with a log-normal distribution plus a power-law. Also shown are the individual log-normal (orange line) and power-law (green line) inferred distributions. The 1σ confidence interval is represented by the thickness of the lines. The deviation point from the log-normal to the power-law regime is well determined with a low associated error, which is shown as a red line. The column density where gravity starts to play a more important role corresponds to $(8.4 \pm 0.23)\times10^{22}$ cm^{-2}. We note that this is only a reference value, since the deviation point can also be affected by changes in the temperature of the gas in the vicinity of young protostars. However, in either case the deviation from the log-normal distribution indicates the effect of self-gravity. The inferred value for the width of the log-normal distrbution is σ_{ln} = 0.27 $\pm$ 0.01 and for the slope of the power-law, α = -2.20 $\pm$ 0.01.

Observations of clouds in the solar neighbourhood suggest a column density threshold of $\sim 1.4\times10^{22}$ cm^{-2} above which star formation takes place with high efficiency (Lada et al. 2010). In the case of G305.137+0.069 the column densities are higher than this threshold, as for other regions (Rathborne et al. 2014), suggesting that this value may not be universal.

4.2.2 Physical parameters of cores

The derived physical parameters of the cores are summarized in Table 4.4. The radius, given in column 2, were determined from the relation $R = \frac{\Theta D}{2}$ where Θ is the FWHM angular size determined from a 2D Gaussian fit to the spatial intensity distribution. The radius of the cores range from 1800 to 5300 AU. The masses were calculated using the expression (Hildebrand 1983),

$$M = \frac{D^2 F_\nu R_{g\mathrm{d}}}{\kappa_\nu B_\nu(T)} \quad ,$$

where F_ν is the flux density at frequency ν. This expression assumes that the dust emission is optically thin. Assuming a distance D=3.4 kpc, a dust temperature T=20 K, $\kappa_{3mm} = 0.21$ cm^2 g^{-1} (see section 4.1.1), and a gas-to-dust ratio R_{gd} of 100, the above expression reads at 3 mm as

$$M = 4.84\ F_{3mm}(mJy)\ M_\odot,$$

where $F_{3mm}(mJy)$ is the flux density at 3 mm in mJy. The mass of the cores, given in column 3, range from 3.3 to 50.6 $M_\odot$. The densities of the cores, given in column 4, were computed from the mass and radius as $n = 3M/4\pi R^3$. They range from 3.1×10^6 to 3.1×10^7cm^{-3}.

Most of the cores have column densities lying above the threshold for star formation derived from the N-PDF analysis of G305.137+0.069 (see Figure 4.10), and hence are expected to be self-gravitating objects. To assess whether the cores in this MDCC are gravitationally bound or unbound and transient (ignoring the effects of magnetic fields or external pres-

Table 4.4: Derived parameters of cores.

Core	Radius ($\times 10^3$AU)	M_{dust} ($M_\odot$)	Density ($\times 10^6 cm^{-3}$)	M_{vir} ($M_\odot$)	α_{vir}
(1)	(2)	(3)	(4)	(5)	(6)
mm-1	3.4±0.5	8.2±1.9	6.4±2.2	24.0±3.5	3.0±0.6
mm-2	3.0±0.4	3.3±0.77	3.9±1.3	—	—
mm-3	2.8±0.4	5.3±1.3	7.7±2.6	19.0±2.8	3.6±0.7
mm-4	5.3±0.7	14.8±3.5	3.1±1.1	—	—
mm-5	4.5±0.6	22.5±5.3	7.3±2.5	25.7±3.8	1.1±0.2
mm-6	2.4±0.3	11.6±2.7	26.1±8.8	21.5±3.2	1.9±0.4
mm-7	1.8±0.3	5.8±1.4	31.4±10.6	—	—
mm-8	4.0±0.6	50.6±11.9	23.3±7.9	39.2±5.7	0.78±0.2
mm-9	3.9±0.6	36.3±8.5	18.4±6.3	26.0±3.9	0.72±0.1
mm-10	5.2±0.7	46.7±11.0	9.9±3.3	—	—
mm-11	3.1±0.4	12.0±2.8	12.5±4.2	—	—
mm-12	2.7±0.4	7.1±1.7	11.3±3.8	10.0±1.5	1.4±0.3

sure), we computed the virial mass, M_{vir}, defined as $M_{vir} = 5\sigma^2 R/G$ where σ is the velocity dispersion ($\sigma = \Delta v/2.35$), R is the radius and G the gravitational constant, and the virial parameter, α_{vir}, defined as $\alpha_{vir} = M_{vir}/M_{dust}$ where M_{dust} is the core mass derived from the dust continuum observations. The virial mass and virial parameter of the cores, computed using the sizes given in Table 5 and the linewidths of the N_2H^+ emission given in Table 3, are given in columns 5 and 6 of Table 4.4, respectively. Five cores have α_{vir} values within a factor of 1.5 of the nominal value for virial equilibrium, indicating that they are likely to be gravitationally bound structures. There are two cores (mm-1 and mm-3) with α_{vir} greater than 3, suggesting they may correspond to transients objects. Figure 4.11 shows the dust versus virial mass for the seven cores with derived line widths. The solid line represents $\alpha_{vir} = 1$. We can see that only the more massive cores are subvirial. In what follows we describe the properties of the three most massive cores within the clump, individually.

mm-8. This core, located at the center of the MDCC (see Figure 4.2), is the most massive one within G305.137+0.069, with a mass of 50.6 $M_\odot$. It has a radius of 4000 AU, a center velocity of −37.0 km/s and a linewidth of 3.1 km/s. Its virial parameter is 0.78, consistent with being gravitationally bound and prone to collapse. This core exhibits strong high velocity redshifted and blueshifted emission in CS (see Figure 4.4). It is not clear, however, whether the HV emission arises from streams of gas falling towards the center of the gravitational potential or from a bipolar outflow driven by a protostar embedded in this core.

mm-9. Located 3.7 north-east from mm-8 (see Figure 4.2), this core has a dust mass of 36.3 $M_\odot$ and a radius of 3900 AU. Its center velocity is −36.9 km/s and its linewidth is 2.6 km/s. Its virial parameter is 0.7, indicating that it is gravitationally bound and possibly collapsing. The spectra of HCO^+ shows a weak self-absorption feature (see Figure 4.4).

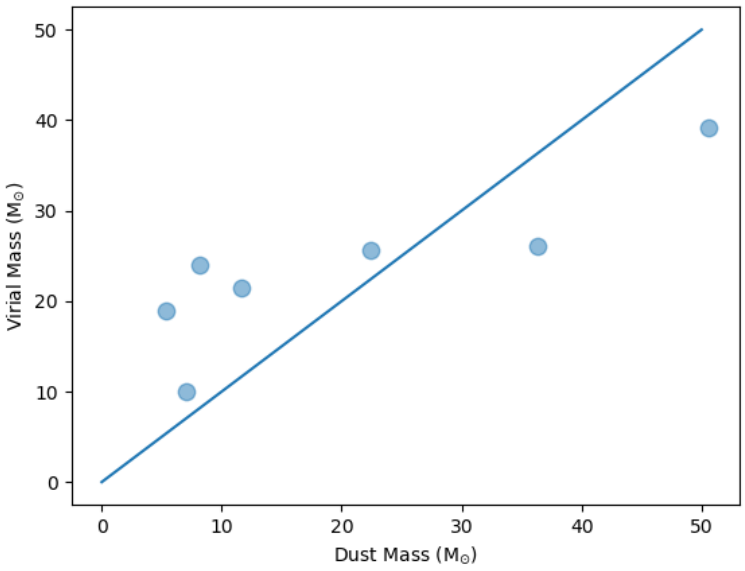

Figure 4.11: Dust mass versus virial mass for the seven cores with derived line widths from hyperfine fitting of N_2H^+ J(1-0) emission (see Table 4.4. The solid line represents $\alpha_{\rm vir} = 1$).

mm-10. Located 6 south-east of mm-8 (see Figure 4.2), this core is the second most massive within the clump, having a dust mass of 46.7 $M_\odot$ and a radius of 5200 AU. The N_2H^+ emission spectra shows the presence of two velocity components (see Figure 4.4). A fitting made using the two sets of hyperfine components give center velocities of -38.0 and -35.3 km/s and linewidths of 2.2 and 2.0 km/s respectively. In addition to these two velocity components, the CS spectra towards core mm-10 shows high-velocity redshifted emission (see Figure 4.8). These results suggest that mm-10 might be the result of converging flows.

4.2.3 Fragmentation and the Core Mass Function

Massive clumps are expected to fragment into cores leading to the formation of a cluster of stars. However, the properties of the cores at the early stages of evolution of MDCCs are poorly known. Our ALMA observations of the G305.137+0.069 clump offers the possibility to investigate the core mass function (CMF) within a MDCC in an early stage of evolution. We recall that the G305.137+0.069 clump has a mass of 1.1×10^3 $M_\odot$, an average density of $\sim 2 \times 10^5$ cm^{-3} (Garay et al. 2004) and an average temperature of 20 K. The thermal Jeans-mass under these conditions is 3.5 $M_\odot$. G305.137+0.069 MDCC can potentially form a cluster of stars, moreover, its mass and radius are consistent with high-mass star cluster progenitors (Kauffmann and Pillai 2010).

A handful of observations towards low-mass star forming regions show that the CMF of their small scale ($<$ 6000 AU) starless cores has a shape (or slope) similar to that of the stellar initial mass function (IMF), suggesting that the cores are direct progenitors of the stellar masses (e.g., Motte et al. 1998; Könyves et al. 2015). To investigate whether this conclusion holds for regions likely to form high-mass stars, such as G305.137+0.069, we show in Figure 4.12 the empirical Cumulative Distribution Function (CDF) of the cores, the

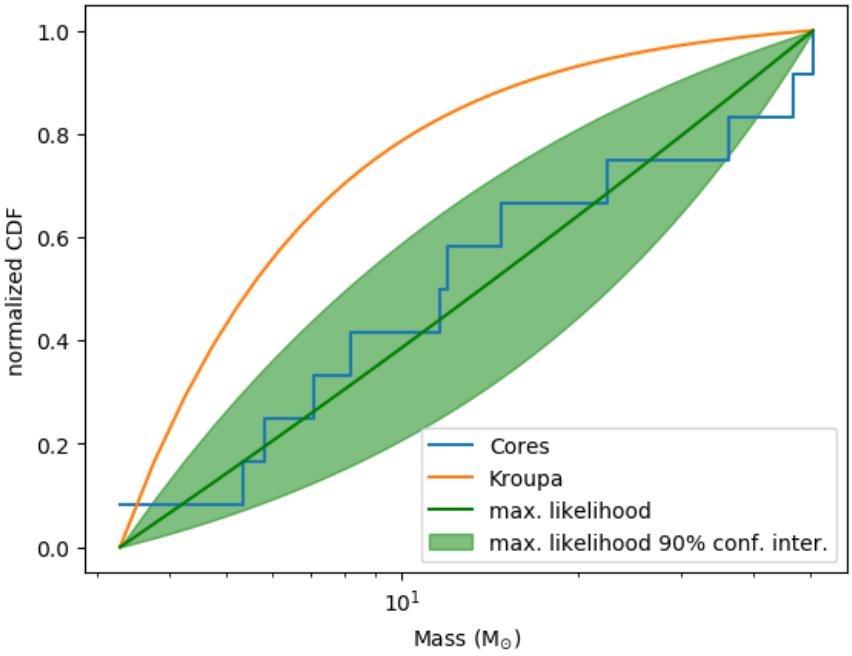

Figure 4.12: Core mass function (CMF) for the cores within G305.137+0.069. The blue line shows the cumulative distribution function of the cores, the orange line shows the initial mass function distribution (IMF) from Kroupa (2001). The green line and green shaded area show the maximum likelihood estimation of the power law index ($\gamma = 0.02$) and its 90% confidence interval ($\gamma \in [-0.60, 0.64]$), respectively.

proportion of cores that are less than or equal to each value considering all cores reported in Table 4.1. Following $\mathrm{d}n/\mathrm{d}\log M \propto M^{\gamma}$, the inferred value of the power law index γ is 0.02 $\pm$ 0.37 (1σ errors) and the 90% confidence interval is -0.60 to 0.64. This power law index is much flatter than that of the IMF for stars with masses greater than 1 $M_\odot$, of -1.35 (Kroupa 2001), indicated by the orange line. We note that due to the small number of cores we preferred to use the CDF, rather than the differential form of the CMF, to avoid numerical biases introduced by binning. We conclude that in G305.137+0.069 there is an excess of high-mass cores (masses above 30 $M_\odot$) relative to the population of intermediate mass cores (5–10 $M_\odot$) if the distribution of core masses followed a Kroupa IMF. A similar conclusion has been recently reported for the cores in the W43-mm1 region, for which a γ index of -0.9 has been derived (Motte et al. 2018). Furthermore, our ALMA observations also indicate that there is a lack of low mass cores in the bin 2.7 to 4.6 $M_\odot$ which can not be attributed to a sensitivity bias, since the 5σ limiting mass of our observations corresponds to 2.4 $M_\odot$. Similar findings have been reported towards a few MDCC in an early stages of evolution (Zhang et al. 2015, Bontemps et al. 2010).

Further, we find that the total mass in the form of cores towards G305.137+0.069 is 224.1 $M_\odot$. Therefore $\sim$ 30% of the total mass of the clump is in the form of cores with masses $\gtrsim$ 3 $M_\odot$. The remaining, more diffuse, gas can be a reservoir for the existing cores to continue accreting, and therefore increase their mass, or give rise to new cores.

4.2.4 Constraints on models of high-mass star formation

In what follows we discuss the above results in the frame of the proposed models and the constraints they impose on them. The shape of the CMF in G305.137+0.069 is definitively different from that of the stellar IMF, showing an overpopulation of high-mass cores compared to intermediate-mass cores. This result is difficult to reconcile with the competitive accretion model (Bonnell and Bate 2002), which assumes that initially the clump fragments into cores of thermal Jean-mass which then accrete matter from the surroundings to give rise to a CMF similar in shape to the IMF (e.g. Motte et al. 1998, Testi and Sargent 1998, Könyves et al. 2015). Since G305.137+0.069 is highly turbulent, we first consider whether the formation of the dense cores in this MDCC could be explained within the frame of the turbulent fragmentation model proposed by Padoan and Nordlund (2002). They showed that the mass distribution of cores with masses above 1 $M_{\odot}$ formed by the process of turbulent fragmentation follows a power-law with a slope of $3/(4\text{-}\beta)$, where β is the power spectrum index of the turbulence. The derived value of the slope of the core mass distribution in G305.137+0.069, of ~ 0.0, can not be explained by a reasonable value of β.

The number of observed fragments in G305.137+0.069 is at least an order of magnitude smaller than the number of Jeans masses in the clump, of ~ 300 ($= M_{clump}/M_J$), being limited to a small number of massive cores. The limited fragmentation at the early evolutionary stages of MDCC has been already reported by Csengeri et al. (2017) but with observations made at lower angular resolution. A similar result to ours was recently reported by Contreras et al. 2018 who detected, using ALMA observations with 1.2 resolution, only 22 cores towards the massive ($\sim$ 1200 $M_{\odot}$) Infrared Dark Cloud G331.372-0.116. The extracted cores in G305.137+0.069 have a mean mass of 18.7 $M_{\odot}$, about 5 times larger than the Jean mass (at the average condition of the clump). Possible mechanisms that increase the mass scale for fragmentation include turbulence and magnetic fields. In addition, it has been argued that the level of fragmentation could be limited to a few massive cores if the clump is undergoing global gravitational collapse (Schneider et al. 2010, Bontemps et al. 2010). This possibility finds support in single dish observations which indicate that G305.137+0.069 is undergoing large scale infalling motions (Garay et al. 2015). This is illustrated in Figure 3.11 which shows the profiles of the optically thick HCN(3-2) and optically thin HNC(3-2) lines as observed with the APEX telescope (FWHM beam of 20). A fit to these line profiles using the simple Hill5 model of De Vries and Myers (2005) indicate an infall velocity of $\sim$2.5 km s^{-1}.

Theoretical works (e.g., Koyama and Inutsuka 2000; Heitsch et al. 2008) have shown that low-velocity shocks appear in turbulent colliding flows. Interestingly low velocity SiO emission, likely to arise from shocks, has been detected towards G305.137+0.069 (Jackson et al. 2013) giving further support to the idea that the cores are forming via the merging of flows driven by gravity in a turbulent clump. The question of whether the observed cores in G305.137+0.069 will continue to fragment leading to the formation of a group of low-mass stars or collapse into a single high-mass star is difficult to discern with the present data. The first alternative may find support by the fact that in MDC in more evolved stages of evolution the CMF closely resembles the IMF shape (e.g., Ginsburg et al. 2017). On the other hand, using the empirical mass versus radius relationship of Kauffmann and Pillai (2010) above which cores avoid fragmentation, we might conclude that most of the cores in G305.137+0.069 will not undergo fragmentation and form a single massive protostar.

The new ALMA observations strongly suggest that the CMF in MDCCs is not universal, and is likely to depend on the dynamical state (or evolutionary stage) of the clump as well as on its mass. We find that massive clumps in their early stages of evolution are underpopulated with low-mass cores. This suggests that high-mass stars may only form in dynamical clouds during the initial cluster formation phase whereas low-mass stars form continuously and may approach the standard IMF at later stage.

Chapter 5

Conclusions

We performed APEX observations in the 270 GHz band of molecular emission, in the HCO^+, HNC, N_2H^+, HCN, and CH_3OH lines, towards four massive and dense cold clumps G305.136+0.069, G333.125-0.562, G18.606-0.076 and G34.458+0.12 in order to study their physical and kinematical conditions at large scales. The line profiles indicate different kinematic signatures for the clumps. G305.136+0.068 exhibits the simpler profiles with Gaussian like lines and absence of prominent high velocity wings, suggesting it is in an early, quiescent stage of evolution. The line profiles of the other three clumps exhibit high velocity wings and multiple peaks in several of the detected lines, suggesting complex large-scale kinematics. The linewidths of the clumps are in the range from 3.1 to 5.5 km/s and are therefore dominated by turbulence. All clumps have virial parameters ~ 1, indicating that they are close to be gravitationally bound. The profiles of the emission in optically thick molecular lines towards G305.136+0.068 and G333.125-0.562 show blue asymmetries indicative of gas infall motions with infall speeds of $\sim$2 km/s.

The density and velocity dispersion radial profiles are important indicators to characterize the evolutionary stage of star forming clumps. Thus we investigated the velocity dispersion profiles for our clumps. Assuming a power law velocity dispersion radial profile ($\Delta v \propto r^{\alpha}$) the power law index derived for three of our clumps (G305.136+0.068, G18.606-0.076 and G34.458+0.121) are between -1.4 and -0.3, in all cases consistent with a profile with linewidths that increase inwards. Other works find values of the power law index > 0. This difference can be interpreted as due to a higher degree of dynamical activity of the gas in the central regions of HMSF clumps.

G305.136+0.069 shows Gaussian like profiles and absence of prominent high velocity wings at large scales (APEX data), suggesting it is in an early stage of evolution. Thus, we decided it was the perfect candidate for ALMA high angular resolution observations. We performed ALMA observations at 3mm of dust continuum and molecular emission, in the HCO^+, CS and N_2H^+ lines, towards G305.136+0.069 in order to reveal its small-scale structure. The result can be summarized as follows:

1. From the continuum image we identified, using the GaussClump algorithm, twelve cores. The dust derived masses range from 3.3 to 50.6 $M_{\odot}$, their sizes from 1800 to

5300 AU, and their densities from 3.1 $\times 10^6$ to 3.1 $\times 10^7$ cm^{-3}.

2. The column densities across G305.136+0.069 have a mean value of 4.3 $\times 10^{23}$ cm^{-2} and a maximum value of 8.1 $\times 10^{23}$ cm^{-2}. An analysis of the column density PDF shows that the deviation point from a log-normal distribution to a power-law regime is (8.4 $\pm$ 0.23)$\times 10^{22}$ cm^{-2}. Most of the extracted cores have column densities larger than this value, suggesting they are self-gravitating. The deviation value is not consistent with the values reported for the solar neighbourhood suggesting that this value may not be universal.
3. We analysed the Core Mass Function(CMF) using the empirical Cumulative Distribution Function (CDF) to avoid binning bias. The shape of the CMF above 3 M$_\odot$ in G305.137+0.069 is definitively different from that of the IMF, showing an excess of high-mass cores compared to intermediate-mass cores. In addition there is a lack of low mass cores (masses in the range 3 to 5 M$_\odot$). We interpret these results as indicating that in the early stages of collapse of massive dense clumps only massive cores are formed and suggest that high-mass stars may only form in dynamical clouds during the initial cluster formation phase whereas low-mass stars form continuously and may approach the standard IMF at later stage.
4. Emission was detected in all three observed molecular transitions. The observed profiles in the HCO$^+$ and CS lines are highly complex, showing high velocity wings, self-absorption features and multiple peaks. The diversity of non-Gaussian line-shape features indicates that G305.137+0.069 is a turbulent clump in an early stage of evolution. The overall morphology of the emission in the HCO$^+$ and CS lines are similar, indicating they trace the same molecular gas, their weak emission being more uniformly distributed and extended than the weak continuum emission.The N_2H^+ emission is best correlated with the continuum emission and hence with the cores.
5. The line widths of the cores range from 1.9 to 3.1 km/s and are therefore dominated by non-thermal motions. Whether the large line widths are reflecting micro-turbulent motions or infalling motions within collapsing cores is difficult to assess. The most massive cores have virial parameters smaller than 1, suggesting they are probably collapsing.
6. The observed spatial morphology and kinematics of the gas within the G305.137+0.069 MDCC convey the idea that the cores are formed in a globally collapsing via the gravitational focusing of gas towards the large potential wells and the merging of flows driven by gravity.

Bibliography

Battersby, C., J. Bally, J. M. Jackson, A. Ginsburg, Y. L. Shirley, W. Schlingman, and J. Glenn
2010. An Infrared Through Radio Study of the Properties and Evolution of IRDC Clumps. , 721:222–250.

Bergin, E. A. and M. Tafalla
2007. Cold Dark Clouds: The Initial Conditions for Star Formation. , 45:339–396.

Beuther, H., E. B. Churchwell, C. F. McKee, and J. C. Tan
2007. The Formation of Massive Stars. *Protostars and Planets V*, Pp. 165–180.

Blake, G. A., E. C. Sutton, C. R. Masson, and T. G. Phillips
1987. Molecular abundances in OMC-1 - The chemical composition of interstellar molecular clouds and the influence of massive star formation. , 315:621–645.

Blitz, L.
1993. Giant molecular clouds. In *Protostars and Planets III*, E. H. Levy and J. I. Lunine, eds., Pp. 125–161.

Blitz, L., L. Magnani, and L. Mundy
1984. High-latitude molecular clouds. , 282:L9–L12.

Blitz, L., L. Magnani, and A. Wandel
1988. Broad-wing molecular lines without internal energy sources. , 331:L127–L130.

Blitz, L. and F. H. Shu
1980. The origin and lifetime of giant molecular cloud complexes. , 238:148–157.

Bonnell, I.
1997. Collapse, Fragmentation and Binary Stars. In *The Third Pacific Rim Conference on Recent Development on Binary Star Research*, K.-C. Leung, ed., volume 130 of *Astronomical Society of the Pacific Conference Series*, P. 1.

Bonnell, I. A. and M. R. Bate
2002. Accretion in stellar clusters and the collisional formation of massive stars. , 336:659–669.

Bonnell, I. A., M. R. Bate, C. J. Clarke, and J. E. Pringle

2001. Competitive accretion in embedded stellar clusters. , 323:785–794.

Bontemps, S., F. Motte, T. Csengeri, and N. Schneider
2010. Fragmentation and mass segregation in the massive dense cores of Cygnus X. , 524:A18.

Burkhart, B., K. Stalpes, and D. C. Collins
2017. The Razors Edge of Collapse: The Transition Point from Lognormal to Power-Law Distributions in Molecular Clouds. , 834:L1.

Caselli, P., P. J. Benson, P. C. Myers, and M. Tafalla
2002. Dense Cores in Dark Clouds. XIV. N_2H^+ (1-0) Maps of Dense Cloud Cores. , 572:238–263.

Caselli, P. and P. C. Myers
1995. The Line Width–Size Relation in Massive Cloud Cores. , 446:665.

Chambers, E. T., J. M. Jackson, J. M. Rathborne, and R. Simon
2009. Star Formation Activity of Cores within Infrared Dark Clouds. , 181:360–390.

Chira, R.-A., R. J. Smith, R. S. Klessen, A. M. Stutz, and R. Shetty
2014. Line profiles of cores within clusters - III. What is the most reliable tracer of core collapse in dense clusters? , 444:874–886.

Clemens, D. P. and R. Barvainis
1988. A catalog of small, optically selected molecular clouds - Optical, infrared, and millimeter properties. , 68:257–286.

Contreras, Y., J. M. Rathborne, A. Guzman, J. Jackson, S. Whitaker, P. Sanhueza, and J. Foster
2017. Characterizing the properties of cluster precursors in the MALT90 survey. , 466:340–354.

Contreras, Y., P. Sanhueza, J. M. Jackson, A. E. Guzmán, S. Longmore, G. Garay, Q. Zhang, Q. Nguy#7877n-Lu'o'ng, K. Tatematsu, F. Nakamura, T. Sakai, S. Ohashi, T. Liu, M. Saito, L. Gomez, J. Rathborne, and S. Whitaker
2018. Infall Signatures in a Prestellar Core Embedded in the High-mass 70 μm Dark IRDC G331.372-00.116. , 861:14.

Crapsi, A., P. Caselli, M. C. Walmsley, and M. Tafalla
2007. Observing the gas temperature drop in the high-density nucleus of L 1544. , 470:221–230.

Csengeri, T., S. Bontemps, F. Wyrowski, S. T. Megeath, F. Motte, A. Sanna, M. Wienen, and K. M. Menten
2017. The ATLASGAL survey: The sample of young massive cluster progenitors. , 601:A60.

Daniel, F., M.-L. Dubernet, M. Meuwly, J. Cernicharo, and L. Pagani
2005. Collisional excitation rate coefficients of N_2H^+ by He. , 363:1083–1091.

De Vries, C. H. and P. C. Myers
2005. Molecular Line Profile Fitting with Analytic Radiative Transfer Models. , 620:800–815.

Efron, B.
1982. *The Jackknife, the Bootstrap and other resampling plans.*

Falgarone, E., D. C. Lis, T. G. Phillips, A. Pouquet, D. H. Porter, and P. R. Woodward
1994. Synthesized spectra of turbulent clouds. , 436:728–740.

Faúndez, S., L. Bronfman, G. Garay, R. Chini, L.-Å. Nyman, and J. May
2004. SIMBA survey of southern high-mass star forming regions. I. Physical parameters of the 1.2 mm/IRAS sources. , 426:97–103.

Fontani, F., R. Cesaroni, P. Caselli, and L. Olmi
2002. The structure of molecular clumps around high-mass young stellar objects. , 389:603–617.

Garay, G., S. Faúndez, D. Mardones, L. Bronfman, R. Chini, and L.-Å. Nyman
2004. Discovery of Four New Massive and Dense Cold Cores. , 610:313–319.

Garay, G. and S. Lizano
1999. Massive Stars: Their Environment and Formation. , 111:1049–1087.

Garay, G., D. Mardones, Y. Contreras, J. E. Pineda, E. Servajean, and A. E. Guzmán
2015. G305.136+0.068: A Massive and Dense Cold Core in an Early Stage of Evolution. , 799:75.

Ginsburg, A., C. Goddi, J. M. D. Kruijssen, J. Bally, R. Smith, R. Galván-Madrid, E. A. C. Mills, K. Wang, J. E. Dale, J. Darling, E. Rosolowsky, R. Loughnane, L. Testi, and N. Bastian
2017. Thermal Feedback in the High-mass Star- and Cluster-forming Region W51. , 842:92.

Ginsburg, A. and J. Mirocha
2011. PySpecKit: Python Spectroscopic Toolkit. Astrophysics Source Code Library.

Goodman, A. A., J. A. Barranco, D. J. Wilner, and M. H. Heyer
1998. Coherence in Dense Cores. II. The Transition to Coherence. , 504:223–246.

Güsten, R., L. Å. Nyman, P. Schilke, K. Menten, C. Cesarsky, and R. Booth
2006. The Atacama Pathfinder EXperiment (APEX) - a new submillimeter facility for southern skies -. , 454:L13–L16.

Guzmán, A. E., P. Sanhueza, Y. Contreras, H. A. Smith, J. M. Jackson, S. Hoq, and J. M. Rathborne
2015. Far-infrared Dust Temperatures and Column Densities of the MALT90 Molecular Clump Sample. , 815:130.

Hartmann, L. and A. Burkert

2007. On the Structure of the Orion A Cloud and the Formation of the Orion Nebula Cluster. , 654:988–997.

Heitsch, F., L. W. Hartmann, A. D. Slyz, J. E. G. Devriendt, and A. Burkert
2008. Cooling, Gravity, and Geometry: Flow-driven Massive Core Formation. , 674:316–328.

Herschel, W.
1785. On the Construction of the Heavens. *Philosophical Transactions of the Royal Society of London Series I*, 75:213–266.

Hildebrand, R. H.
1983. The Determination of Cloud Masses and Dust Characteristics from Submillimetre Thermal Emission. , 24:267.

Hindson, L., M. A. Thompson, J. S. Urquhart, A. Faimali, J. S. Clark, and B. Davies
2012. The G305 star-forming complex: a wide-area radio survey of ultracompact H II regions. , 421:3418–3430.

Jackson, J. M., J. M. Rathborne, J. B. Foster, J. S. Whitaker, P. Sanhueza, C. Claysmith, J. L. Mascoop, M. Wienen, S. L. Breen, F. Herpin, A. Duarte-Cabral, T. Csengeri, S. N. Longmore, Y. Contreras, B. Indermuehle, P. J. Barnes, A. J. Walsh, M. R. Cunningham, K. J. Brooks, T. R. Britton, M. A. Voronkov, J. S. Urquhart, J. Alves, C. H. Jordan, T. Hill, S. Hoq, S. C. Finn, I. Bains, S. Bontemps, L. Bronfman, J. L. Caswell, L. Deharveng, S. P. Ellingsen, G. A. Fuller, G. Garay, J. A. Green, L. Hindson, P. A. Jones, C. Lenfestey, N. Lo, V. Lowe, D. Mardones, K. M. Menten, V. Minier, L. K. Morgan, F. Motte, E. Muller, N. Peretto, C. R. Purcell, P. Schilke, S.-N. Bontemps, F. Schuller, A. Titmarsh, F. Wyrowski, and A. Zavagno
2013. MALT90: The Millimetre Astronomy Legacy Team 90 GHz Survey. , 30:e057.

Kauffmann, J., F. Bertoldi, T. L. Bourke, N. J. Evans, II, and C. W. Lee
2008. MAMBO mapping of Spitzer c2d small clouds and cores. , 487:993–1017.

Kauffmann, J. and T. Pillai
2010. How Many Infrared Dark Clouds Can form Massive Stars and Clusters? , 723:L7–L12.

Kennicutt, Jr., R. C.
1990. Global effects of interactions on galaxy evolution. In *NASA Conference Publication*, J. W. Sulentic, W. C. Keel, and C. M. Telesco, eds., volume 3098 of *NASA Conference Publication*.

Könyves, V., P. André, A. Men'shchikov, P. Palmeirim, D. Arzoumanian, N. Schneider, A. Roy, P. Didelon, A. Maury, Y. Shimajiri, J. Di Francesco, S. Bontemps, N. Peretto, M. Benedettini, J.-P. Bernard, D. Elia, M. J. Griffin, T. Hill, J. Kirk, B. Ladjelate, K. Marsh, P. G. Martin, F. Motte, Q. Nguyên Luong, S. Pezzuto, H. Roussel, K. L. J. Rygl, S. I. Sadavoy, E. Schisano, L. Spinoglio, D. Ward-Thompson, and G. J. White
2015. A census of dense cores in the Aquila cloud complex: SPIRE/PACS observations

from the Herschel Gould Belt survey. , 584:A91.

Koyama, H. and S.-I. Inutsuka
2000. Molecular Cloud Formation in Shock-compressed Layers. , 532:980–993.

Kroupa, P.
2001. The Local Stellar Initial Mass Function. In *Dynamics of Star Clusters and the Milky Way*, S. Deiters, B. Fuchs, A. Just, R. Spurzem, and R. Wielen, eds., volume 228 of *Astronomical Society of the Pacific Conference Series*, P. 187.

Kuznetsova, A., L. Hartmann, and J. Ballesteros-Paredes
2018. Kinematics and structure of star-forming regions: insights from cold collapse models. , 473:2372–2377.

Lada, C. J. and E. A. Lada
2003. Embedded Clusters in Molecular Clouds. , 41:57–115.

Lada, C. J., M. Lombardi, and J. F. Alves
2010. On the Star Formation Rates in Molecular Clouds. , 724:687–693.

Lapinov, A. V., P. Schilke, M. Juvela, and I. I. Zinchenko
1998. Studies of dense cores in regions of massive star formation. VI. Multitransitional CS and CO observations of G 261.64-2.09, G 268.42-0.85, G 270.26+0.83 and G 301.12-0.20. , 336:1007–1023.

Larson, R. B.
1981. Turbulence and star formation in molecular clouds. , 194:809–826.

Liu, T., Y. Wu, J. Wu, S.-L. Qin, and H. Zhang
2013. Competitive accretion in the protocluster G10.6-0.4? , 436:1335–1342.

MacLaren, I., K. M. Richardson, and A. W. Wolfendale
1988. Corrections to virial estimates of molecular cloud masses. , 333:821–825.

Magnani, L. and J. S. Onello
1995. A new method for determining the CO to H2 conversion factor for translucent clouds. , 443:169–180.

Mangum, J. G. and Y. L. Shirley
2015. How to Calculate Molecular Column Density. , 127:266.

McKee, C. F. and E. C. Ostriker
2007. Theory of Star Formation. , 45:565–687.

McKee, C. F. and J. C. Tan
2003. The Formation of Massive Stars from Turbulent Cores. , 585:850–871.

McLaughlin, D. E. and R. E. Pudritz
1996. A model for the internal structure of molecular cloud cores. , 90:326.

McLaughlin, D. E. and R. E. Pudritz
1997. Gravitational Collapse and Star Formation in Logotropic and Nonisothermal Spheres. , 476:750–765.

Motte, F., P. Andre, and R. Neri
1998. The initial conditions of star formation in the rho Ophiuchi main cloud: wide-field millimeter continuum mapping. , 336:150–172.

Motte, F., T. Nony, F. Louvet, K. A. Marsh, S. Bontemps, A. P. Whitworth, A. Men'shchikov, Q. Nguyen Luong, T. Csengeri, A. J. Maury, A. Gusdorf, E. Chapillon, V. Könyves, P. Schilke, A. Duarte-Cabral, P. Didelon, and M. Gaudel
2018. The unexpectedly large proportion of high-mass star-forming cores in a Galactic mini-starburst. *Nature Astronomy*, 2:478–482.

Müller, H. S. P., F. Schlöder, J. Stutzki, and G. Winnewisser
2005. The Cologne Database for Molecular Spectroscopy, CDMS: a useful tool for astronomers and spectroscopists. *Journal of Molecular Structure*, 742:215–227.

Müller, H. S. P., S. Thorwirth, D. A. Roth, and G. Winnewisser
2001. The Cologne Database for Molecular Spectroscopy, CDMS. , 370:L49–L52.

Myers, P. C., D. Mardones, M. Tafalla, J. P. Williams, and D. J. Wilner
1996. A Simple Model of Spectral-Line Profiles from Contracting Clouds. , 465:L133.

Naranjo-Romero, R., E. Vázquez-Semadeni, and R. M. Loughnane
2015. Hierarchical Gravitational Fragmentation. I. Collapsing Cores within Collapsing Clouds. , 814:48.

Ossenkopf, V. and T. Henning
1994. Dust opacities for protostellar cores. , 291:943–959.

Padoan, P. and Å. Nordlund
2002. The Stellar Initial Mass Function from Turbulent Fragmentation. , 576:870–879.

Peretto, N. and G. A. Fuller
2009. The initial conditions of stellar protocluster formation. I. A catalogue of Spitzer dark clouds. , 505:405–415.

Pillai, T., F. Wyrowski, S. J. Carey, and K. M. Menten
2006. Ammonia in infrared dark clouds. , 450:569–583.

Pineda, J. E., A. A. Goodman, H. G. Arce, P. Caselli, J. B. Foster, P. C. Myers, and E. W. Rosolowsky
2010. Direct Observation of a Sharp Transition to Coherence in Dense Cores. , 712:L116–L121.

Pirogov, L., I. Zinchenko, P. Caselli, L. E. B. Johansson, and P. C. Myers
2003. N_2H^+(1-0) survey of massive molecular cloud cores. , 405:639–654.

Plume, R., D. T. Jaffe, N. J. Evans, II, J. Martín-Pintado, and J. Gómez-González
1997. Dense Gas and Star Formation: Characteristics of Cloud Cores Associated with Water Masers. , 476:730–749.

Rathborne, J. M., S. N. Longmore, J. M. Jackson, J. F. Alves, J. Bally, N. Bastian, Y. Contreras, J. B. Foster, G. Garay, J. M. D. Kruijssen, L. Testi, and A. J. Walsh
2015. A Cluster in the Making: ALMA Reveals the Initial Conditions for High-mass Cluster Formation. , 802:125.

Rathborne, J. M., S. N. Longmore, J. M. Jackson, J. M. D. Kruijssen, J. F. Alves, J. Bally, N. Bastian, Y. Contreras, J. B. Foster, G. Garay, L. Testi, and A. J. Walsh
2014. Turbulence Sets the Initial Conditions for Star Formation in High-pressure Environments. , 795:L25.

Rosolowsky, E. W., J. E. Pineda, J. Kauffmann, and A. A. Goodman
2008. Structural Analysis of Molecular Clouds: Dendrograms. , 679:1338–1351.

Sanhueza, P., J. M. Jackson, J. B. Foster, G. Garay, A. Silva, and S. C. Finn
2012. Chemistry in Infrared Dark Cloud Clumps: A Molecular Line Survey at 3 mm. , 756:60.

Sault, R. J., P. J. Teuben, and M. C. H. Wright
1995. A Retrospective View of MIRIAD. In *Astronomical Data Analysis Software and Systems IV*, R. A. Shaw, H. E. Payne, and J. J. E. Hayes, eds., volume 77 of *Astronomical Society of the Pacific Conference Series*, P. 433.

Schilke, P., D. J. Benford, T. R. Hunter, D. C. Lis, and T. G. Phillips
2001. A Line Survey of Orion-KL from 607 to 725 GHZ. , 132:281–364.

Schneider, N., T. Csengeri, S. Bontemps, F. Motte, R. Simon, P. Hennebelle, C. Federrath, and R. Klessen
2010. Dynamic star formation in the massive DR21 filament. , 520:A49.

Schuller, F., K. M. Menten, Y. Contreras, F. Wyrowski, P. Schilke, L. Bronfman, T. Henning, C. M. Walmsley, H. Beuther, S. Bontemps, R. Cesaroni, L. Deharveng, G. Garay, F. Herpin, B. Lefloch, H. Linz, D. Mardones, V. Minier, S. Molinari, F. Motte, L.-Å. Nyman, V. Reveret, C. Risacher, D. Russeil, N. Schneider, L. Testi, T. Troost, T. Vasyunina, M. Wienen, A. Zavagno, A. Kovacs, E. Kreysa, G. Siringo, and A. Weiß
2009. ATLASGAL - The APEX telescope large area survey of the galaxy at 870 μm. , 504:415–427.

Sharma, S.
2017. Markov Chain Monte Carlo Methods for Bayesian Data Analysis in Astronomy. *ArXiv e-prints*.

Shu, F. H.
1977. Self-similar collapse of isothermal spheres and star formation. , 214:488–497.

Shu, F. H., F. C. Adams, and S. Lizano

1987. Star formation in molecular clouds - Observation and theory. , 25:23–81.

Snell, R. L., L. G. Mundy, P. F. Goldsmith, N. J. Evans, II, and N. R. Erickson
1984. Models of molecular clouds. I - Multitransition study of CS. , 276:625–645.

Snow, T. P. and B. J. McCall
2006. Diffuse Atomic and Molecular Clouds. , 44:367–414.

Stutzki, J. and R. Guesten
1990. High spatial resolution isotopic CO and CS observations of M17 SW - The clumpy structure of the molecular cloud core. , 356:513–533.

Testi, L. and A. I. Sargent
1998. Star Formation in Clusters: A Survey of Compact Millimeter-Wave Sources in the Serpens Core. , 508:L91–L94.

Wang, P., Z.-Y. Li, T. Abel, and F. Nakamura
2010. Outflow Feedback Regulated Massive Star Formation in Parsec-Scale Cluster-Forming Clumps. , 709:27–41.

Williams, J. P., L. Blitz, and A. A. Stark
1995. The Density Structure in the Rosette Molecular Cloud: Signposts of Evolution. , 451:252.

Wilson, R. W., K. B. Jefferts, and A. A. Penzias
1970. Carbon Monoxide in the Orion Nebula. , 161:L43.

Zhang, Q., K. Wang, X. Lu, and I. Jiménez-Serra
2015. Fragmentation of Molecular Clumps and Formation of a Protocluster. , 804:141.